Title
Niche-associated heterogeneity of lymphoid stromal cells

Author
Rodda, Lauren Barbara

Publication Date
2017

Niche-associated heterogeneity of lymphoid stromal cells

by

Lauren B. Rodda

DISSERTATION

Submitted in partial satisfaction of the requirements for the degree of

DOCTOR OF PHILOSOPHY

in

Biomedical Sciences

in the

GRADUATE DIVISION

of the

UNIVERSITY OF CALIFORNIA, SAN FRANCISCO

This dissertation is dedicated to my parents,

Jane Van Doren and David Rodda,

for the endless love, support and opportunities they have

provided me in my pursuit of becoming a scientist

ACKNOWLEDGEMENTS

Over the course of my PhD, Dr. Jason Cyster has shared with me his immense knowledge of immunology, meticulous project design, technical rigor in experiments and succinct communication skills. His expansive understanding of the literature and mentorship in hypothesis development has been essential to my success in the lab. As I began coming up with my own project and experiment ideas, he was available daily for discussion and was supportive of me learning the new microscopy techniques, single-cell RNA sequencing technology and computational analysis required for my projects. Finally, through feedback on lab meetings and presentations, Jason has taught me how to convey my work with clarity and precision. He has taught me this style in writing papers as well and committed significant time and energy to the rapid production of these papers. Jason is a role model of a successful scientist and has provided an intense training in immunology, bench techniques and effective and efficient publication.

I have also benefitted from my thesis committee members' expert feedback. Rich Locksley and Mark Ansel provided critical analysis of my projects informing important decisions about the direction of the work. Their expertise expanded my thinking about the context and applications of the work. I greatly appreciated their readiness to meet with me outside of official committee meetings and their input on my future plans.

The bulk of my training happened in the lab and was shaped by my fellow lab members with whom I shared long hours, frustrations and triumphs. I began my rotation under the direction of Dr. Oliver Bannard, who balanced critical mentorship with humility. His mastery of the literature fueled many illuminating discussions. For most of my time, I shared a bay with Dr. Jagan Muppidi and Erick Lu. Jagan was a constant

source of uplifting motivation and an incredible example of critical thought, persistent experimentation and efficient progress. He trained me in many techniques and helped me build and refine hypotheses. His mentorship and friendship are irreplaceable. Erick Lu began graduate school several years after me, but has been a role model of hard work, persistence and commitment. He is by far the most respectful and selfless member of the lab, spending more than his share of time replenishing common resources.

The Cyster Lab post-docs during my tenure did much to advance my education. Dr. Andrea Reboldi's unwavering excitement and commitment to science were contagious. He was generous with his time and creativity and discussions about immunology, from seminars to my project, never failed to be inspiring as well as useful. Dr. Tangsheng Yi was an excellent model of hard work and productivity. These pursuits led him to frequently suggest I ask for help from the 'real' expert in the lab who, invariably, was anyone but him. His initial work on follicular dendritic cells (FDCs) launched my project and he dedicated time and encouragement to get me started. While beginning to study FDCs, I had the opportunity to work with Dr. Xiaoming Wang, who paired a quiet nature with meticulous skill. I frequently reflect on the perspectives of the field that he shared with me. I also received early sage advice from Dr. Tal Arnon, whose confidence, technical mastery and voracious appetite for science I strive to emulate. Dr. Hsin Chen taught me how to use and optimize the two-photon and confocal microscopes, which became the central tools of my research. Dr. Francisco Ramierez-Valle imbued the lab culture with fierce experimental precision and kindness. All of the post-docs including Dr. Michael Barnes, Dr. Brian Laidlaw, Dr. Jiaxi Wu, Dr.

Dan Liu and Dr. Hayakazu Sumida gave thoughtful feedback in lab meetings and were a constant source of support. Jinping An, our lab manager, is an irreplaceable member of the lab, keeping our resources viable and managing the critical mouse colony. In addition, Ying Xu, our lab technician, and her technical expertise have been essential for my experimental progress.

My fellow graduate students have also contributed to my scientific growth. Early on, Dr. Betsy Gray and Dr. Brenda Han were already technical experts and helped me with experiments as well as helping me stay organized. Their focus and discipline is enviable. Dr. Tim Schmidt provided an infectious positivity that was much needed. Eric Dang quickly became a leader in the lab not just in data productivity, but also in commitment to productive scientific discussion. I always valued his expert input and found our discussions of the future of the field and new technologies most inspirational. Another MD-PhD student, Michelle (Shelly) Mintz has become an impressive role model of persistence and attention to detail. Her example and friendship has revitalized me in these later years. While the lab culture has evolved over my time there, I am confident the commitment to rigorous experiments, technical excellence and crucial immunological questions will not wane under the purview of our newest graduate students Elise Wolf and Antonia Gallman.

I chose to come to UCSF because of the welcoming and collaborative community and would like to thank everyone, professors and students, who made it so. I enjoyed being part of this atmosphere and my research benefitted greatly from the generosity of other immunology labs with trial and last minute reagents and technical expertise. As Biomedical Science graduate students we were committed to helping each other

succeed. In particular, Dr. Jenny Qi, Dr. Adriana Mujal, Dr. Darienne Myers and Katherine Farrar inspired me in and outside the lab, providing essential balance along with critical feedback and technical advice. My graduate experience could not have progressed with such ease without the administrative aid of Claire Chan, Brandy Lopez, Annie Chan and the Biomedical Sciences team: Demian Sainz, Ned Molyneaux, Monique Piazza, Lisa Magargal and Nathan Jew. The help of the LARC administration and staff was also invaluable.

Finally, I would not be at UCSF without the support of my family and friends. My parents, Jane Van Doren and David Rodda, have provided me incredible opportunities to find my path from the very beginning. Early kitchen pH chemistry turned into school projects, a summer research internship and coding textbooks. They are my ultimate role models of hard-work, commitment, intellectual curiosity and discipline. Their unwavering love and encouragement fuels me daily to pursue the heights. I also greatly appreciate the motivation and enthusiasm of my grandparents Barbara Van Doren, Lawrence Van Doren, Dorothy Rodda and Gordon Rodda and all my aunts, uncles and cousins. My friends outside of UCSF have become my West coast family and I could not have completed my PhD without the support of Eva Cheung, Miriam Zachau Walker, Anna Tarakanova, Mahati Chintapalli, Suejung Shin and Kasey Rowe. Lastly, I have been incredibly fortunate to find a daily confidant and companion in Cory Diers. His resolute support and buoyant spirit have seen me through the worst of lows in graduate school and ushered me to the best of highs. I am forever grateful for the immense positive impact he has had on the person I am today.

CONTRIBUTIONS TO PRESENTED WORK

All work described in this thesis was performed under the direct supervision and guidance of Dr. Jason G. Cyster. Funding for this research was acquired by Dr. Cyster except where stated in the acknowledgement section of each chapter. Additional contributions are described below.

Chapter 2 was published as Rodda, L.B., Bannard, O., Ludewig, B., Nagasawa, T., and Cyster, J.G. (2015). Phenotypic and Morphological Properties of Germinal Center Dark Zone Cxcl12-Expressing Reticular Cells. *The Journal of Immunology 195*: 4781–4791. Copyright © 2015. The online manuscript can be found here <www.jimmunol.org/content/195/10/4781.long>. The manuscript is reproduced here in accordance with the policies of The American Association of Immunologists, Inc. I preformed all the experiments and quantification and prepared the figures. I conceived of the experiments and wrote the manuscript with Dr. Cyster. Prior to this work, Dr. Oliver Bannard, a former post-doc in the lab, and Dr. Cyster discovered *Cxcl12*-expressing Reticular Cells (CRCs) and, as such, Dr. Bannard's technical expertise in thick section, confocal imaging of these cells and useful discussion was essential to launch this work. Dr. Bannard also taught me how to implant the Azlet osmotic pumps required for acute treatment with CXCR4 inhibitor. Dr. Hsin Chen, a post-doc in the lab, trained me in use of the 2-photon microscope for explant tissue imaging, which I applied to whole lymph nodes (LNs) and Peyer's patches to image full CRC networks and dark zone germinal center B cell dynamics. Jinping An was our animal technician and performed the mouse screening, which saved valuable time. Other contributors are listed in the acknowledgement section of this chapter.

Chapter 3 is under review as of Dec. 8, 2017 as Rodda L.B., Lu E., Bennett M.L., Sokol C.L., Wang X., Luther S.A., Barres B.A., Luster A.D., Chun J.Y., and Cyster J.G. Single-cell RNA sequencing of LN stromal cells reveals niche-associated heterogeneity. *Immunity*. The manuscript is reproduced here in accordance with the policies of Cell Press and Elsevier, Inc. I preformed all of the computational analysis and most of the experiments, except where specified below, and prepared all the figures. I conceived of the experiments and wrote the manuscript with Dr. Cyster. Dr. Jimmie Ye provided training in the initial computation analysis and useful feedback. Erick Lu, a graduate student in the lab, optimized the RNAscope procedure and trained me in this technique. Mr. Lu performed the RNAscope of *Ch25h* and *Pthlh* expression in the figures. Dr. Xiaoming Wang, a former post-doc in the lab, made the initial observations of ENPP2 staining in LNs, which was replicated by me for the figure. Ying Xu performed the qPCR analysis. Dr. Caroline Sokol performed the REX3 stromal flow cytometry under the supervision of Dr. Andrew Luster. Frozen LNs from REX3 mice were prepared by Ryan Camire and provided to us by Dr. Luster. Dr. Mariko Bennett aided in the logistics of the Tmem119 knockout mice experiments and advised on staining for Tmem119. Dr. Ben Barres provided the Tmem119 knockout mice and Tmem119 antibodies. Dr. Sanjiv Luther provided the rapid stromal isolation protocol I used to prepare LN stroma for single-cell RNA sequencing. Jinping An was our animal technician and performed the mouse screening, which saved valuable time. Other contributors are listed in the acknowledgement section of this chapter.

Niche-associated heterogeneity of lymphoid stromal cells

By Lauren B. Rodda

ABSTRACT

Stromal cells establish the compartmentalization of lymphoid tissues critical for the immune response. However, the full diversity of lymph node stromal cells remains undefined. Germinal centers (GCs) form in the center of follicles during a T-dependent immune response and are comprised of two niches, the light zone, supported by the stromal follicular dendritic cells (FDCs), and the dark zone (DZ), recently described to contain stromal *Cxcl12*-expressing reticular cells (CRCs). GC B cells must cycle to the DZ to achieve efficient antibody affinity maturation, but the properties of CRCs in the DZ are relatively unexplored. Here we find CRCs are present in GC DZs consistently across lymphoid tissues with network morphology and surface marker phenotype distinct from FDCs. CRCs also form smaller networks in the T-zone proximal side of primary follicles. Real-time two-photon microscopy revealed GC B cells explore CRC networks suggesting CRCs may support DZ GC B cell activities through cell-cell interactions. To further explore the heterogeneity of non-endothelial stromal cells supporting LN niches, we used droplet-based single-cell RNA sequencing and identified transcriptional profiles for 8 niche-associated stromal subsets. We found subsets of T-zone reticular cells (TRCs), marginal reticular cells, FDCs and perivascular cells, which have been shown to support the T-zone, subcapsular sinus, follicles and blood vessels, respectively. We also identified and localized new stromal subsets; Ch25h^{+} Ccl19^{lo} TRCs at the T-zone perimeter, Cxcl9^{+} TRCs in the T-zone, CD34^{+} stromal cells in the

capsule and medullary vessel adventitia and Inmt^{+} stromal cells enriched in the medullary cords. Additionally, we validated Tmem119 and Pthlh as novel FDC markers and Sox9 as a novel marker of FDCs and CRCs. These transcriptional profiles enable exploration of niche-associated stromal functions, stromal development and the context-dependent activities of lymphocytes in an immune response.

TABLE OF CONTENTS

LIST OF TABLES

Chapter 3

LIST OF FIGURES

Chapter 2

Chapter 3

CHAPTER 1

Introduction

Chapter 1

Lymph nodes (LNs) are positioned throughout the body and serve as outposts of the immune system. Lymphatics drain antigen and immune cells from other tissues to LNs as naïve lymphocytes circulate through the LNs, Peyer's patches and spleen surveying for foreign material. This tissue organization allows efficient detection of antigen by rare antigen-specific lymphocytes and rapid activation of the adaptive immune response (Gretz et al., 1996). LNs, and the phagocytic cells within them, may also serve as a barrier to systemic infection by filtering out lymph-borne pathogens (Barral et al., 2010; Coombes et al., 2012; Gray et al., 2012; Iannacone et al., 2010a; Kastenmuller et al., 2012; Zhang et al., 2016).

LNs are organized into discrete niches to optimize the cell-cell interactions required for activation of pathogen antigen-specific lymphocytes without inducing autoimmune activation. Each niche is patterned by mesenchymal-derived stromal cells. Initially considered solely structural cells, stromal cells are now appreciated to contribute to tissue organization and lymphocyte survival, migration, antigen encounter and tolerance (Bajénoff et al., 2006; Chang and Turley, 2015; Malhotra et al., 2013; Roozendaal and Mebius, 2011; Schulz et al., 2016).

Marginal reticular cells (MRCs) are stromal cells that line the subcapsular sinus (SCS) floor at the T-zone distal edge of the follicle, where lymph-borne antigen first drains from the afferent lymphatics (Katakai et al., 2004). The LN follicles are B cell rich regions patterned by the stromal follicular dendritic cells (FDCs) at the follicle center (Allen and Cyster, 2008). MRCs and FDCs secrete CXCL13 to attract $CXCR5^{+}$ B cells to survey the follicles for antigen (Ansel et al., 2000; Cyster, 2010).

Chapter 1

Germinal centers develop at the center of B cell follicles during an immune response and are essential for the generation of high affinity antibodies. GCs are further divided into two niches, the dark zone (DZ), where B cells proliferate and mutate their BCR and the light zone (LZ) where they undergo selection and become plasma cells, memory cells or recycle to the DZ for additional rounds of affinity maturation (Bannard and Cyster, 2017). The zones were thus named based on initial histology of GCs (Rohlich, 1930). Primary follicle FDCs upregulate complement receptors, Fc receptors and integrin ligands as they develop into GC LZ FDCs (Allen and Cyster, 2008). They support the functions of the LZ by presenting immune-complexed antigen, secreting trophic factors and regulating chemokine gradients important for GC confinement (Allen and Cyster, 2008; Wang et al., 2011; Yi et al., 2012). FDCs are dependent on lymphotoxin expressed by B cells (Ansel et al., 2000), but how they develop is still unclear. MRCs, pericytes and $CD34^+$ adventitial cells have all been suggested as FDC progenitor cells (Jarjour et al., 2014; Krautler et al., 2012; Sitnik et al., 2016). Features of these rare cells have been notoriously difficult to study because FDCs are difficult to isolate from tissue without lymphocyte or other stromal cell contamination (Heesters et al., 2013; Suzuki et al., 2010; Wilke et al., 2010).

In order to move to the DZ, GCB cells must upregulate CXCR4 to respond to CXCL12 being expressed in the DZ (Allen et al., 2004; Bannard et al., 2013). Experiments with CXCR4-deficient B cells demonstrated that experiencing the DZ is essential for efficient affinity maturation (Bannard et al., 2013). While the DZ niche has long been appreciated to be devoid of LZ FDCs or much extracellular matrix, ultrastructural studies had identified a stromal population in the DZ (Imai and

Yamakawa, 1996; Rademakers, 1992). To investigate what DZ cell was making the critical chemokine CXCL12, Bannard et al. used a GFP reporter of *Cxcl12*-expression and identified a novel stromal population in the DZ they termed *Cxcl12*-expressing reticular cells (CRCs) (Bannard et al., 2013). Beyond their putative role in guiding GC B cells to the DZ, CRC morphology, relationship to surrounding stroma and maintenance requirements remain unclear.

Outside the B cell follicles, T-zone reticular cells (TRCs) are stromal cells that occupy the T-zone and secrete extracellular matrix to form conduits for lymph drainage from the SCS (Mueller and Germain, 2009). Leukocytes enter LNs through high endothelial venules (HEVs) in the T-zone, part of the network of blood vessels supported by adjacent perivascular cells (PvCs) and sometimes adventitial cells (Armulik et al., 2011; Gunn et al., 1998; Sitnik et al., 2016). $CCR7^+$ leukocytes migrate to the T-zone in response to TRC-expressed CCL19 and CCL21 (Luther et al., 2000). These leukocytes include hematopoetic-derived dendritic cells (DCs) that survey the TRC ensheathed, lymph-draining conduits for antigen to present to T cells crawling along the same conduits (Mueller and Germain, 2009). Upon activation, T cells may migrate to the follicular/T-zone interface to interact with activated antigen-specific B cells and trigger a germinal center (GC) response (Ansel et al., 1999).

Without activation, B and T cells circulate in their respective niches and then exit the LN through the medullary cords and medullary sinus and drain to the next LN for continued surveillance (Andrian and Mempel, 2003; Cyster, 2005). Medullary reticular cells (MedRCs) are stromal cells that pattern the medulla where medullary cord macrophages, medullary sinus macrophages and plasma cells reside (Gray and Cyster,

2012a; Link et al., 2007). Medullary CXCL12 expression is suggested to attract $CXCR4^{hi}$ plasma cells, but these stroma are relatively poorly understood (Hargreaves et al., 2001).

How each of these stromal cell types create, maintain and influence their niches is still unclear. No distinct stromal subset has been described for the critical follicle/T-zone interface or for interfollicular regions, early sites of antigen encounter and a location of memory T cells. This implies more stromal heterogeneity may exist to support these unique niches.

Transcriptional profiles for the different niche-associated stromal cell types would be useful to further study their functions, but the stromal heterogeneity and paucity of distinguishing markers has made this difficult. Podoplanin (PDPN) was one of the first markers described for stromal cells and is still the standard for subsetting LN stromal cells for flow cytometric and transcriptional analysis (Farr et al., 1992; Link et al., 2007; Malhotra et al., 2012; Onder et al., 2011). However, PDPN only subsets the non-endothelial LN stromal populations into two groups, $PDPN^{+}$ stromal cells collectively termed fibroblastic reticular cells (FRCs) and $PDPN^{-}$ stromal cells termed double negative cells (DNCs). While the transcriptional profiles of these bulk populations reported by the Immgen consortia have been useful to study stromal contributions to LN function (Malhotra et al., 2012), section staining suggests that FRCs include stromal cells that support many of the major LN niches, namely MRCs, FDCs and TRCs and DNCs include at least MedRCs and PvCs (Link et al., 2007). This low-resolution subsetting obscures the distinct nature of these functionally unique niche-associated stromal subsets. Niche-based resolution is required to study the many remaining

questions regarding lymphoid stromal development, niche formation and stromal-lymphocyte cross-talk.

Here we explore the features of CRCs in the GC DZ and the underappreciated heterogeneity of LN stromal cells. We use imaging to assess the stroma in their native niche and single-cell RNA sequencing to obtain transcriptional information about their functions in their niche. We find that CRCs form in two morphologies in GC DZs across lymphoid tissues as well as forming smaller networks in primary follicles. CRCs are phenotypically distinct from FDCs and do not require lymphotoxin signaling as FDCs do, but likely share a developmental lineage. CRC networks do require CXCR4-signaling and GC B cells explore and potentially interact with CRC processes. Broadening our study of LN stromal cells, we found eight transcriptionally distinct subsets of non-endothelial stroma and mapped each to a specific LN niche. We also found three novel markers of the elusive FDCs, demonstrating how these stromal subset transcriptional profiles can bolster further study of niche-associated stromal participation in the LN immune response.

CHAPTER 2

Phenotypic and morphological properties of germinal center dark zone *Cxcl12*-expressing reticular cells

This chapter was published as:

Rodda, L.B., Bannard, O., Ludewig, B., Nagasawa, T., and Cyster, J.G. (2015). Phenotypic and Morphological Properties of Germinal Center Dark Zone Cxcl12-Expressing Reticular Cells. *The Journal of Immunology 195*, 4781–4791.

Chapter 2

Abstract

The germinal center (GC) is divided into a dark zone (DZ) and a light zone (LZ). GC B cells must cycle between these zones to achieve efficient antibody affinity maturation. Follicular dendritic cells (FDCs) are well characterized for their role in supporting B cell antigen encounter in primary follicles and in the GC LZ. However, the properties of stromal cells supporting B cells in the DZ are relatively unexplored. Recent work identified a novel stromal population of *Cxcl12*-expressing reticular cells (CRCs) in murine GC DZs. Here we report that CRCs have diverse morphologies, appearing in 'open' and 'closed' networks, with variable distribution in lymphoid tissue GCs. CRCs are also present in splenic and peripheral lymph node primary follicles. Real-time two-photon microscopy of Peyer's patch GCs demonstrates B cells moving in close association with CRC processes. CRCs are gp38^{+} with low to undetectable expression of FDC markers, but CRC-like cells in the DZ are lineage marked, along with FDCs and FRCs, by *CD21*-Cre and *Ccl19*-Cre directed fluorescent reporters. In contrast to FDCs, CRCs do not demonstrate dependence on lymphotoxin or TNF for chemokine expression or network morphology. CRC distribution in the DZ does require CXCR4 signaling, which is necessary for GC B cells to access the DZ and likely to interact with CRC processes. Our findings establish CRCs as a major stromal cell type in the GC DZ and suggest CRCs support critical activities of GC B cells in the DZ niche through *Cxcl12* expression and direct cell-cell interactions.

Introduction

Lymphoid tissue stromal cells are specialized mesenchymal cells that establish and maintain the distinct niches necessary to support effective adaptive immune responses. Lymphoid follicles, the B cell rich regions of lymphoid organs, are organized around a complex network of follicular stromal cells (Cyster et al., 2000). Many of the follicular stromal cells in primary (non-reactive) follicles produce the chemokine CXCL13 (BLC) and are involved in attracting B cells into this compartment. Follicular dendritic cells (FDCs) are a subset of these CXCL13-expressing stromal cells situated in the central region of the follicle (Cyster et al., 2000). First defined by their ability to capture opsonized antigens, FDCs are now known to highly express complement receptors-1 and -2 (CD35 and CD21 respectively) and Fcγ receptors to support the process of immune complex capture and display to cognate B cells (Allen and Cyster, 2008; Cyster et al., 2000; Shikh and Pitzalis, 2012). FDCs and the broader CXCL13-producing follicular stromal cell network share a dependence on the cytokines lymphotoxin-α1β2 (LT) and TNF for maintenance and function (Fu and Chaplin, 1999; Lu and Browning, 2014; Ngo et al., 1999).

While FDCs are one of the stromal cell types supporting B cell follicles, fibroblastic reticular cells (FRCs) are mesenchymal stromal cells that support the structure and function of the T zone. FRCs produce the chemokines CCL19 and CCL21 in a LT-dependent manner to guide CCR7-expressing B and T cells into lymph node (LN) and splenic T zones (Chai et al., 2013; Luther et al., 2000; Ngo et al., 1999). FRCs also promote T cell homeostasis by producing IL-7 (Link et al., 2007). Additionally,

FRCs form a network of conduits in the T zone that transport antigen and facilitate T cell encounter with antigen-bearing dendritic cells (Mueller and Germain, 2009).

Following antigen exposure, activated B cells proliferate in B cell follicles and form polarized germinal centers (GCs), each with a light zone (LZ) and a dark zone (DZ). The FDCs within GCs upregulate CD21, CD35, Fc receptors, ICAM1 and VCAM1 and show increased staining for activated complement 4 (C4, FDC-M2) and milk fat globule epidermal growth factor 8 (MFG-E8, FDC-M1) relative to FDCs in primary follicles (Allen and Cyster, 2008). Antigen-bearing FDCs are restricted to the LZ designating this as the site of B cell antigen recognition and selection (Allen et al., 2007a). GC FDCs have also been shown to be essential for GC B cell confinement and viability (Wang et al., 2011). CXCL13 is present in the GC LZ and plays a role in positioning GC B cells in this region. In contrast, the DZ has little CXCL13 and instead is a source of CXCL12 (SDF1). GC B cell movement from LZ to DZ as well as GC polarization into zones depends on GC B cell expression of the CXCL12 receptor CXCR4 (Allen et al., 2004). Once in the DZ, GC B cells express higher amounts of activation-induced cytidine deaminase, undergo somatic hypermutation and are more likely to proliferate before returning to the LZ (Cyster et al., 2000; Victora and Nussenzweig, 2012). Recent work has highlighted the importance of the DZ for affinity maturation and GC participation as these were impaired in CXCR4 knockout GC B cells that could not access the DZ (Bannard et al., 2013).

In contrast to the extensive study of FDCs since their discovery in the 1960's, little is known about the stromal cells in the GC DZ. Ultrastructural studies revealed the presence of stromal cells in the DZ of human tonsil GCs and referred to them as

immature FDCs even though they mostly did not capture or display opsonized antigen, lacked the ‘labyrinth-like’ structure of LZ FDCs and their relationship to true antigen-capturing FDCs was unclear (Imai and Yamakawa, 1996; Rademakers, 1992). Lefevre and coworkers described a mAb, found to bind fibrinogen, that stained DZ stromal cells in bovine and ovine GCs (Lefevre et al., 2007). However, fibrinogen was found not to be made locally by the DZ stroma and was thought to have derived from blood or lymph. In recent work, we followed up on the functional evidence that CXCL12 emanates from the DZ (Allen et al., 2004) to reveal the existence of *Cxcl12*-expressing reticular cells (CRCs) in mediastinal LN GC DZs after influenza (Bannard et al., 2013). While CRCs have only minimal overlap with reticular fibers in the mediastinal LN, CRCs were so named to represent their net-like morphology, as the term ‘reticular’ comes from the latin word for ‘net’ (Cyster et al., 2000). This work also provided initial evidence that related cells were present in Peyer’s patches (PPs) and within peripheral LN (pLN) primary follicles. However, whether CRCs are a homogeneous population across tissues, what lineage relationships they have to surrounding stroma and what distinguishing requirements they have for maturation and maintenance were not established.

Here we demonstrate that CRC networks have two distinct morphologies and are present in the GC DZs of spleens and pLNs after viral infection. We also find CRCs within the chronic GCs of mesenteric LNs (MLNs) as well as PPs. GC B cells migrate over CRC processes in a similar manner to their migration over FDC processes. While CRCs are phenotypically distinguishable from FDCs and FRCs, they are likely related in origin based on lineage tracing experiments using *CD21*-Cre and *Ccl19*-Cre transgenic

mice. Distinct from FDCs, CRCs do not require LT or TNF for short-term maintenance of chemokine expression or morphology. Organization of CRCs into reticular networks, however, depends on CXCR4 function.

Results

Cxcl12-expressing Reticular Cells (CRCs) populate the GC DZ niche with fine, irregular networks

To investigate the distinguishing features of GC DZ stroma across tissues, we infected *Cxcl12*-GFP reporter mice with LCMV-Armstrong and assessed the properties of the GFP-expressing CRCs. Using confocal microscopy, we identified extensive CRC networks in splenic and pLN (inguinal, axillary and brachial) GC DZs located opposite the LZ CD35$^+$ FDCs (Fig. 1A, 1B). Chronic GCs in PPs and MLNs also contained CRC networks in the DZ (Fig. 1C), consistent with previous findings in PPs (Bannard et al., 2013). Blood vessels running through the GC were also GFP$^+$ likely indicating blood endothelial cells (BECs) expressing *Cxcl12* (Fig.1B) (Bannard et al., 2013; Ding and Morrison, 2013).

Previous work (Bannard et al., 2013) established that DZ CRC networks are distinguishable from FDCs and FRCs by their location and distinct morphology. Instead of the thick processes and consistent patterning of T zone FRCs, CRCs have fine, disorganized processes more similar to FDCs. However, CRC networks are far less dense than FDC networks. CRC processes are so thin and dispersed that 30μm stack confocal microscopy was required to visualize the networks. We identified surprising variability in CRC network structure when we imaged splenic and pLN GCs of mice responding to LCMV (Fig. 1D). In pLNs, the DZ CRCs formed mostly ‘open’ mesh structures (Fig. 1B, 1D) similar to those observed in influenza-induced mediastinal LN GCs (Bannard et al., 2013). We define ‘open’ networks as having processes that extend into the LZ FDC network with no clear boundary and that become continuous with the

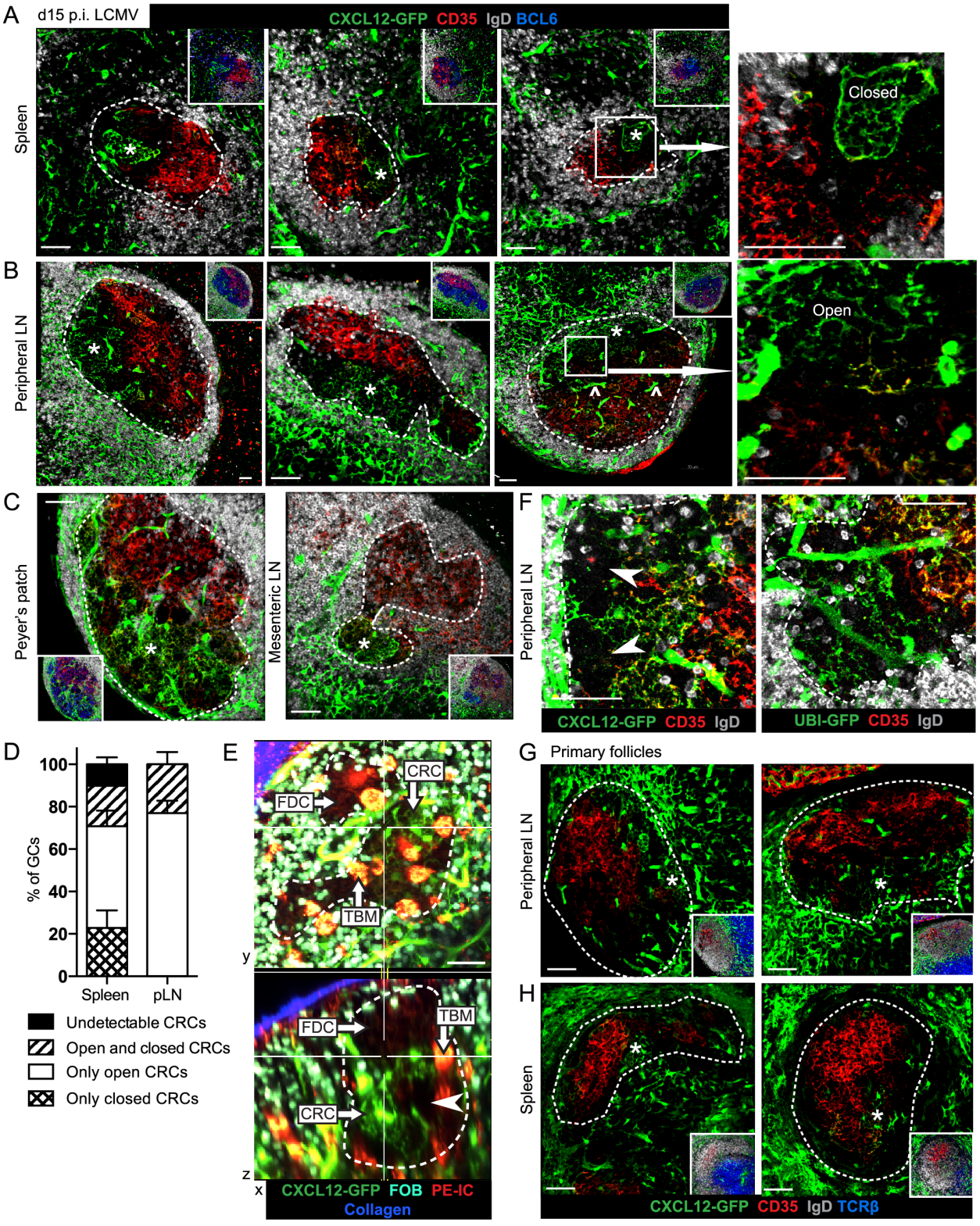
A
d15 p.i. LCMV
CXCL12-GFP CD35 IgD BCL6
Spleen
Closed
B
Peripheral LN
Open
C
Peyer's patch
Mesenteric LN
F
Peripheral LN
CXCL12-GFP CD35 IgD
UBI-GFP CD35 IgD
D
% of GCs
100
80
60
40
20
0
Spleen
pLN
Undetectable CRCs
Open and closed CRCs
Only open CRCs
Only closed CRCs
E
FDC
CRC
TBM
y
z
x
CXCL12-GFP FOB PE-IC
Collagen
G
Primary follicles
Peripheral LN
H
Spleen
CXCL12-GFP CD35 IgD TCRβ

Figure 1. ***Cxcl12*-expressing Reticular Cells (CRCs) populate the DZ niche with fine, irregular networks.**
(A-C) Thick section (30μm) confocal microscopy of *Cxcl12*-GFP$^+$ DZ CRCs (*) and CD35$^+$ FDCs in tissues from *Cxcl12*-GFP mice analyzed at day 15 post-infection (p.i) with LCMV. (^) Blood vessel passing through GC. White box and arrow indicate increased magnification of CRCs in 'closed' formation in spleen (**A**) and in 'open' formation in pLN (**B**). White, dotted line indicates the GC boundary based on BCL6 staining only shown in insets. Data (A-C) are representative of 3 mice and 3-15 GC views per tissue per mouse. **(D)** Average frequency of DZ CRC network morphologies observed in thick sections from 3 LCMV-infected mice with 6-15 GC views per tissue, error bars represent SEM. **(E)** TPLSM of intact *Cxcl12*-GFP MLN GC on day 10 post-immunization with SRBCs and 1 day after transfer of CFP$^+$ naïve B cells (follicular B cells, FOB) to mark the GC edge (white, dotted line) and treatment with PE-IC to label FDCs and TBMs. CRCs, FDCs and TBMs are labeled and areas of undetectable DZ stroma indicated (arrowhead) in XY and XZ sections of the 193μm z-stack shown as maximum intensity projections (x=5.54μm, y=6.09μm, z=30.0μm). Images correspond to Movie S1. Representative of 2 mice and 4 GCs per MLN. **(F)** Regions of undetectable stroma (arrowhead) in pLN GC DZs from *Cxcl12*-GFP mice (3 mice, 3-15 GCs views per mouse) and UBI-GFP mice previously reconstituted with WT BM (2 mice, 1-7 GCs views per mouse) imaged on day 15 p.i. with LCMV. White dotted line indicates the GC boundary based on IgD stain. **(G and H)** Confocal microscopy of CRCs (*) in primary follicles from (**G)** pLN (2 mice, 6-26 follicle views per mouse) and **(H)** spleen (3 mice, 20-90 follicle views per mouse) from unimmunized *Cxcl12*-GFP mice. White, dotted line indicates the boundary of the primary follicle based on TCRβ and IgD stain only shown in insets. Scale bar is 50μm.

FRC-like stroma at the T zone proximal edge of the GC at 3 or greater points. In the spleen, however, one fifth of the GCs contained CRCs with a 'closed' mesh structure (Fig. 1A, 1D). 'Closed' networks are bounded by a continuous perimeter of *Cxcl12*-GFP+ processes and connect to the FRC-like stroma at the T zone proximal edge of the GC at fewer than 3 points. About one fifth of GCs in both tissues contained both types of network (Fig. 1D). CRCs in MLN GCs and PP GCs formed open networks that frequently extended throughout the DZ (Fig. 1C).

Unlike the continuous FDC networks that fill the LZ, CRC networks frequently had an asymmetric distribution in the DZ. Of over 27 single 30μm Z-stack views of GCs from 3 mice, more than half of spleen GC DZs and almost one third of pLN GC DZs appeared only partially populated by CRCs (Fig. 1A, 1B). While tingible body macrophages (TBMs) are present in GCs and do displace stromal processes, these areas were much larger than the size of a TBM and they stained for $BCL6^+$ GC B cells (Fig. 1A, 1B). In the spleen, almost a tenth of the 30μm image stacks had no detectable CRC network in the GC (Fig. 1D). However, analysis of sequential sections of several splenic GCs revealed they all had CRCs in at least one view.

To further investigate the extent of DZ occupancy by CRCs without the extrapolation required by sections, we used two-photon laser-scanning microscopy (TPLSM) to image CRC networks in MLN GCs (Fig.1E, Movie S1) and pLN GCs (Fig. S1A, Movie S2). SRBC-immunized *Cxcl12*-GFP mice were treated with phycoerythrin-immune complex (PE-IC) to label FDCs (TBMs are also strongly labeled) (Allen et al., 2007b; Phan et al., 2007). One day before analysis mice also received CFP transgenic B cells, which populated the follicle and outlined the GC. MLN GCs were frequently

more proximal to the capsule than pLN GCs enabling higher resolution imaging of the DZ, which is orientated distal to the capsule in the GC. In agreement with our section data, we observed CRC networks in separate open and closed structures emerging from the outer edges of the DZ and leaving large areas of DZ unoccupied by detectable CRCs. The thicker 3D view also revealed that each distinct network contained one or more CRC cell bodies, depending on the network size, and many of these cell bodies appeared bi-lobed.

To assess whether the CRC asymmetry in the DZ was a result of CRCs sharing the DZ niche with another stromal cell type or of CRCs having variable *Cxcl12* expression, we analyzed pLNs and spleen from UBI-GFP mice reconstituted with wild-type (WT) bone marrow (BM) and infected with LCMV. In these mice, all stromal cells express GFP. Surprisingly, we observed almost nine tenths of the pLN and splenic GC DZs had CRC-like networks throughout the DZ with no large areas of undetectable stroma (Fig. 1F, S1B). We saw similar results with SRBC immunized mice (Fig. S1C). These data suggest that while CRCs are a major DZ stromal cell type, GCs may contain additional DZ stromal cells that lack detectable *Cxcl12*-GFP expression.

Since CRCs in splenic DZs demonstrated more variability than CRCs in pLN DZs, we expanded on our previous investigation of CRCs in pLN primary follicles (Bannard et al., 2013) to examine CRCs in splenic primary follicles. In unimmunized *Cxcl12*-GFP pLNs, CRC networks extended along the T zone proximal side of the follicle with similar morphology to pLN DZ CRC networks (Fig. 1G) as previously shown (Bannard et al., 2013). In contrast, CRC networks in splenic primary follicles were less extensive than the networks in splenic GC DZs (Fig. 1H). Though they occasionally

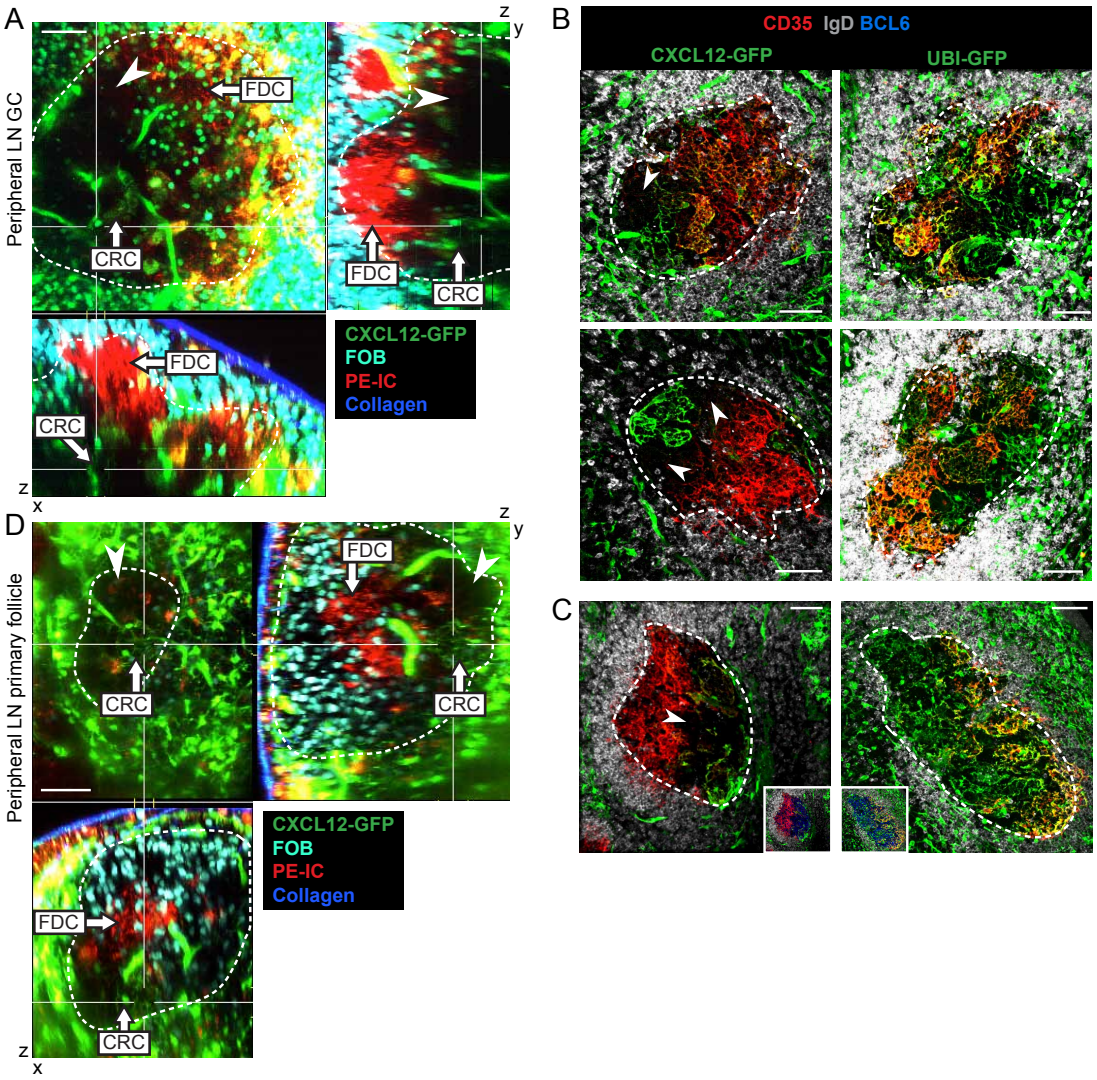

FIGURE S1. Incomplete CRC occupancy of the GC DZ. (A) TPLSM of intact *Cxcl12*-GFP pLN GC on day 10 post-immunization with SRBCs and 1 day after transfer of CFP+ naïve B cells (FOB) to mark the GC edge (white, dotted line) and treatment with PE-IC to label FDCs and TBMs. Due to the high laser power required, CFP+ cells appeared green in the deepest sections, but could be distinguished by their small, lymphocyte morphology. CRCs and FDCs are labeled and areas of undetectable DZ stroma indicated (arrowhead) in sections of the 203μm Z-stack shown as maximum intensity projections (x=19.9μm, y=19.9μm, z=70.0μm). **(B and C)** Confocal microscopy of CRCs and regions of undetectable stroma (arrowhead) in *Cxcl12*-GFP and CRC-like DZ stroma in UBI-GFP splenic GC DZs. UBI-GFP mice previously reconstituted with WT BM. Imaged on **(B)** day 15 p.i. with LCMV (3 *Cxcl12*-GFP mice, 5-14 GC views per mouse, and 2 UBI-GFP mice, 2-18 GC views per mouse) or **(C)** day 14 post-immunization with SRBCs (3 *Cxcl12*-GFP mice, 3-23 GC views per mouse, and 3 UBI-GFP mice, 9-13 GC views per mouse). GCs outlined with white, dotted line based on IgD stain. **(D)** TPLSM of intact *Cxcl12*-GFP pLN primary follicle treated and presented as in (A). Sections of the 256μm Z-stack are shown as maximum intensity projections (x=19.9μm, y=19.9μm, z=30.0μm) and the white, dotted line marks the follicle edge. Images (A and D) correspond to Movie S2 and are representative of 1-2 mice and 1-4 views per mouse. Scale bar is 50μm.

appeared to consist of only one cell in a single 30μm Z-stack, splenic primary CRCs still formed small open and closed networks in the T zone proximal region of the follicle. CRCs were detectable with a similar average frequency in pLN primary follicles (96.2% ± 3.8, n=2) as in LCMV-induced pLN GCs (100% ± 0, n=3) and in splenic primary follicles (87.1% ± 2.0, n=3) as in splenic GCs (89.8% ± 3.3, n=3). We also assessed the 3D organization of pLN primary follicle CRCs using the TPLSM analysis as described above for intact pLN DZ CRCs (Fig. S1D, Movie S2). Based on their shared *Cxcl12* expression, morphology and location, our current work and previous data (Bannard et al., 2013) support the conclusion that both pLN and splenic GC CRCs arise from primary follicle CRCs.

Movement dynamics of GC B cells in association with DZ CRCs

We next investigated whether cell-cell interactions might be important to CRC support of GC B cells in the DZ by determining if GC B cells interact with CRC processes as they move through the DZ. We attempted to visualize the interaction using TPLSM on explanted pLNs (Suzuki et al., 2009), but the DZ in LN GCs is orientated distal to the capsule and the fine CRC processes were too deep in the tissue to be imaged using laser intensities that preserved cell viability. In PPs, GCs form with the DZ proximal to the serosal surface and with the LZ embedded deeper in the tissue facing the subepithelial dome (Lelouard et al., 2012). To take advantage of this superficial positioning of the DZ, we developed an approach to label a fraction of the B cells within PP GCs. We found that when a mixture of 20% CFP transgenic B cells and 80% WT B cells was transferred into hen egg lysozyme-specific (MD4) Ig-transgenic mice for two

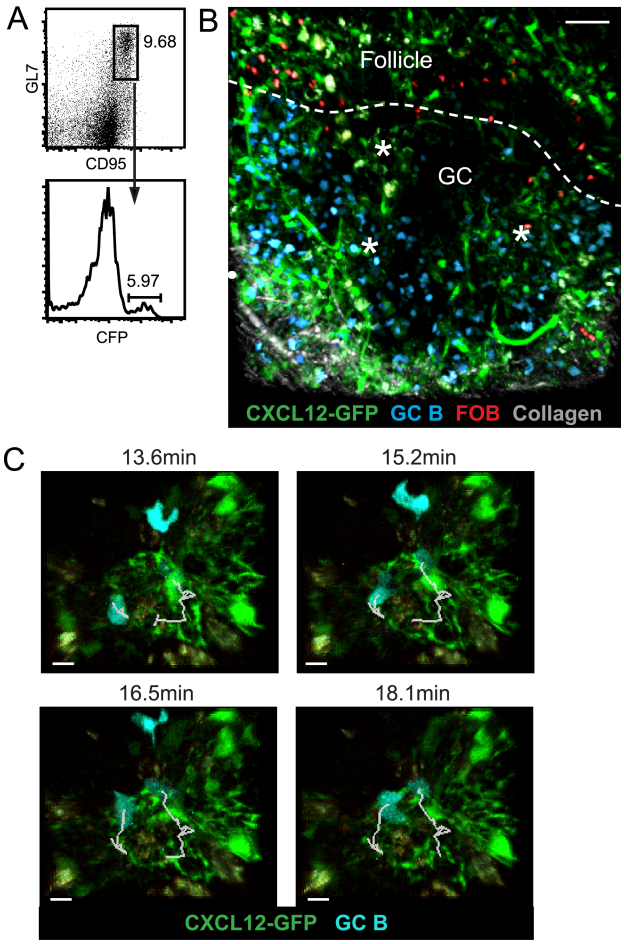

FIGURE 2. Movement dynamics of GC B cells in association with DZ CRCs. TPLSM of *Cxcl12*-GFP MD4 PPs 2 weeks after transfer of WT and CFP^+ B cells and 1 day after transfer of CMTMR-labeled WT B cells to label a portion of the FOB cells and outline the GC (white, dotted line). **(A)** Representative flow cytometry plots showing percent of CFP^+ GC B cells ($B220^+$ IgD^- $GL7^+$ $CD95^+$) in PPs on day of imaging. Pre-gated for $B220^+$ IgD^- cells, numbers indicate percent of parent gate. **(B)** CRC networks (*) in explant PP GC DZ (60μm z-stack) surrounded by CFP^+ GC B cells. Collagen marks the serosal edge of the PP. Images correspond to Movie S3 and S4. Scale bar is 50μm. **(C)** Time lapse images of CFP^+ GC B cells moving through GFP^+ CRC networks in an explant PP (69μm z-stack). Tracks of GC B cells indicated in white. Images correspond to Movie S5. Scale bar is 10μm. Images representative of 6 movies from 3 mice in 3 experiments.

weeks, the host GCs became dominated by the transferred B cells and about 6% of the GC B cells were CFP^+ (Fig. 2A). To visualize CRC-GC B cell interactions, we transferred this mixture of CFP transgenic and WT B cells into *Cxcl12*-GFP MD4 mice and, one day before imaging, injected additional CMTMR-labeled WT B cells to label a portion of the follicular B (FOB) cells and outline the GC (Fig. 2B, Movie S3). CFP^+ GC B cells were observed crawling in and out of the visible DZ CRC networks, sometimes in contact with multiple processes at once, and were seen displacing the fine CRC processes as they moved (Fig. 2C, Movie S4, Movie S5). Rotation of the images showing the 3D networks revealed that the GC B cells were often completely surrounded by CRC processes (Movie S3). GC B cells in CRC networks moved with an average median velocity of 5.44μm/min ± 0.56 (n=5) and an average median turning angle of 68.04^o ± 2.06 (n=5). The average median velocity was in the range described for GC B cells in pLN GCs and the average median turning angle was at the high-end of the previously described range (Allen et al., 2007b; Suzuki et al., 2009).

CRCs are phenotypically distinct from FDC and FRC across tissues, but likely lineage related

Since the properties and origin of FDCs in the LZ vary between secondary lymphoid tissues (Jarjour et al., 2014; Krautler et al., 2012; Wang et al., 2011), we investigated whether splenic DZ CRCs had a different relationship to FDCs and FRCs than did pLN DZ CRCs. Expanding on the initial characterization of flu-infected mediastinal LN CRCs (Bannard et al., 2013), we stained lymphoid tissues from LCMV-

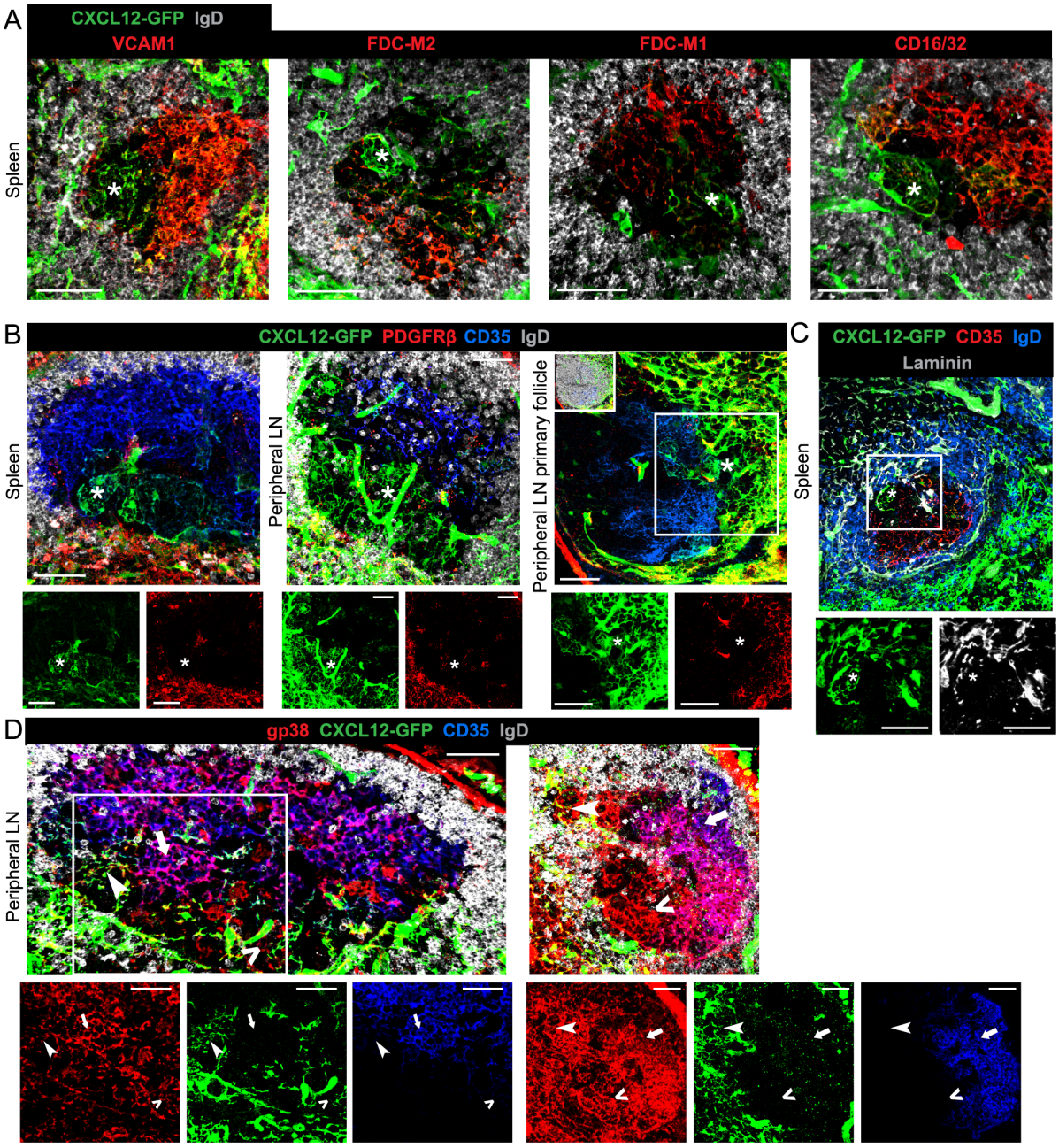

FIGURE 3. CRCs are phenotypically distinct from FDCs and FRCs across tissues. Confocal microscopy of CRCs (*) in GCs from SRBC-immunized *Cxcl12*-GFP mice stained for **(A)** VCAM1, FDC-M2, FDC-M1 and CD16/32 (each image representative of 1-3 mice, 2-20 GC views per spleen), **(B)** GCs and primary follicles stained for PDGFRβ (1-3 mice, 14 GC views per spleen, 2-3 GC views per pLN, 4 follicle views per pLN). In primary pLN panel, IgD is only shown in inset and white box indicates area shown in single channels. **(C)** GC stained for laminin (3 mice, 1-3 GC views per spleen). **(D)** PLN GCs from *Cxcl12*-GFP mice on day 15 p.i. with LCMV stained for gp38 (2 mice, 1-18 GC views per mouse). Examples of CRCs (arrowhead), FDCs (arrow) and gp38^{+} CD35^{-} *Cxcl12*-GFP^{-} stroma (^) are indicated. (C and D) Individual channels shown below merged image and if enlarged, area indicated by white box. Scale bar is 50μm.

infected and SRBC-immunized *Cxcl12*-GFP mice for canonical markers of FDCs. In splenic GCs, CRCs expressed low to undetectable levels of CD21/35 and VCAM1 (Fig.1A, 3A) and undetectable levels of FDC-M2, FDC-M1 and CD16/32 (FcγRIII/II) (Fig. 3A). CRCs in pLN, MLN and PP GCs also expressed low to undetectable levels of CD21/35 and undetectable levels of CD16/32 (Fig. 1B, 1C, S2A) as supported by our previous work (Bannard et al., 2013). PDGFRβ is widely expressed by FRCs, pericytes and other mesenchymal cells (Krautler et al., 2012; Mueller and Germain, 2009), but this marker was undetectable on CRCs in splenic and pLN GCs as well as pLN primary follicles (Fig. 3B). Also unlike FRCs, CRCs in splenic GCs had minimal association with the reticulum, stained for with anti-laminin (Fig. 3C) and anti-type IV collagen (Fig. S2B), except at the T zone proximal edge of the GC where the CRC network meets the FRC network. This is consistent with findings in mediastinal LN GCs (Bannard et al., 2013).

DZ CRCs in pLN GCs did express gp38 (podoplanin), a defining marker of FRCs, as did LZ FDCs (Fig. 3D, S2C) (Mueller et al., 2007). Interestingly, we also observed gp38^{+} stromal processes in the pLN GC DZ that were undetectable for *Cxcl12*-GFP and low to undetectable for CD35 (Fig. 3D, S2C). This is consistent with the data in Fig. 1F, S1B and S1C suggesting the presence of an additional stromal cell type in the DZ. By comparing the areas occupied by gp38^{+} CD35^{-} *Cxcl12*-GFP^{+} CRC processes and gp38^{+} CD35^{-} *Cxcl12*-GFP^{-} CRC processes in each of several GC DZs, we found non-CRC DZ stroma accounted for half of the DZ stromal network (50.06% ± 26.56, n=7). However, this proportion varied widely between individual GCs.

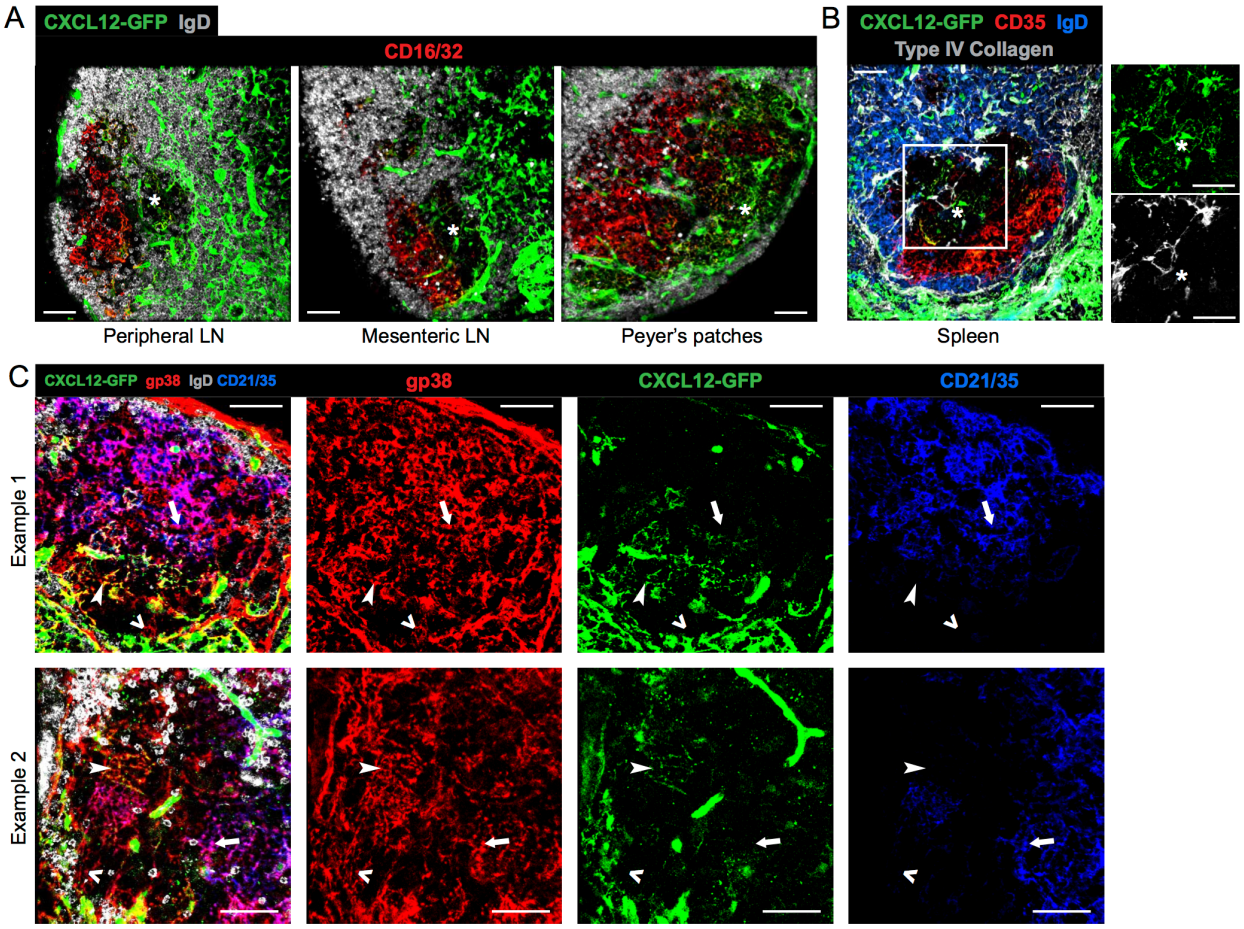

FIGURE S2. Phenotypic characterization of heterogeneous DZ stroma. Confocal microscopy of tissues from SRBC-immunized *Cxcl12*-GFP mice stained for **(A)** CD16/32 (representative of 1-2 mice and 4-9 GC views per tissue per mouse) and **(B)** Type IV collagen (3 mice and 1-7 GC views per spleen). White box indicates area enlarged in single channel images. **(C)** Additional examples of gp38 staining on *Cxcl12*-GFP pLN GCs on day 15 p.i. with LCMV (2 mice, 1-18 GC views per mouse). Examples of CRCs (arrowhead), FDCs (arrow) and gp38+ CD35- *Cxcl12*-GFP- stroma (^) are indicated. Scale bar is 50μm.

While we found CRCs to be phenotypically distinct from FDCs and FRCs, we inquired whether they might still share a precursor with these cells. To test for a relationship with FDCs, *CD21*-Cre mice (Kraus et al., 2004) were crossed with *R26*-ZsGreen reporter mice. Analysis of the resulting mice revealed CD21/35$^{lo/-}$ ZsGreen^{+} CRC-like stromal cells in spleen, MLN and pLN GC DZs and pLN primary follicles along with the expected CD21/35^{hi} ZsGreen^{+} FDCs in these tissues (Fig. 4A). We also observed the recently reported CD21/35^{-} ZsGreen^{+} 'versatile stromal cells' (VSCs) in the T zone in pLNs (Mionnet et al., 2013) and similar CD21/35^{-} ZsGreen^{+} FRC-like cells, possibly also VSCs, in the GC-proximal T zone in spleen and MLN (Fig. 4A). To mark *Ccl19*-expressing FRC and lineage-related cells, we crossed *Ccl19*-Cre mice (Chai et al., 2013) to *R26*-EYFP reporter mice. We found CD21/35$^{lo/-}$ EYFP^{+} CRC-like stromal cells in spleen, pLN, MLN and PP GC DZs of *Ccl19*-Cre *R26*-EYFP mice along with the expected EYFP^{+} T zone FRCs (Fig. 4B) (Chai et al., 2013). The majority of CD35^{hi} FDCs in splenic, pLN and MLN LZs were also *Ccl19*-Cre lineage marked in agreement with previous work (Chai et al., 2013; Fasnacht et al., 2014). However, in PPs the extent of lineage marking of FDCs was variable (Fig. 4B). With both reporters, stroma throughout the GC DZ was lineage-marked providing strong support for the conclusion that DZ CRCs were labeled as well as any non-CRC DZ stroma. In summary, CRCs do not express most of the distinguishing markers of FDCs or FRCs, but may share a lineage precursor with both stromal cell types.

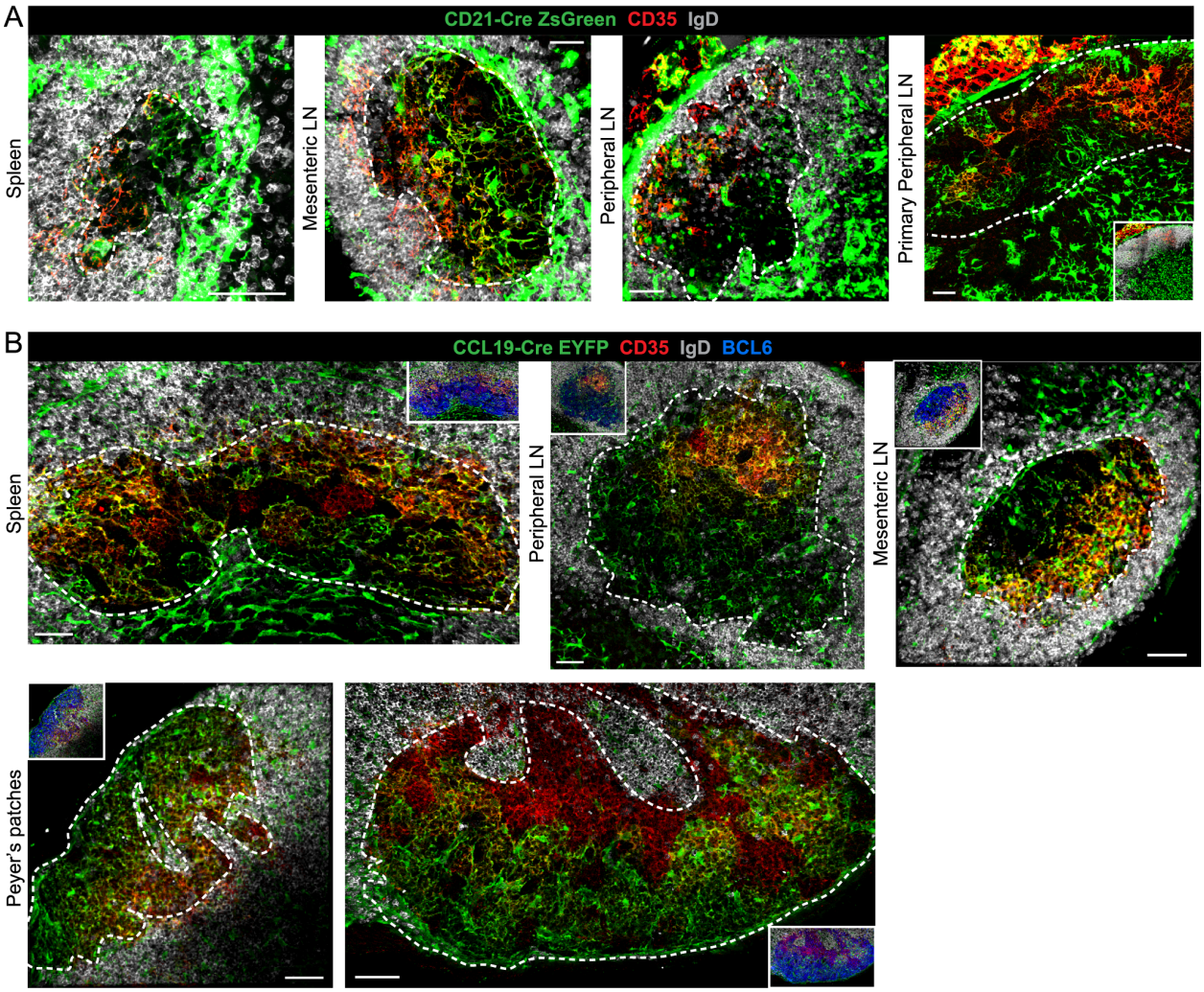

FIGURE 4. CRCs are likely lineage related to FDCs and FRCs.
Confocal microscopy of CRCs (*) in GCs from SRBC-immunized **(A)** *CD21*-Cre *R26*-Z-sGreen lineage reporter mice (1-4 mice, 3-14 GC views per spleen, 2-5 GC views per MLN, 3-10 GC views per pLN and 2 follicle views per primary pLN) and **(B)** *Ccl19*-Cre *R26*-EYFP lineage reporter mice (3 mice, 6-7 GC views per spleen, 2-6 GC views per pLN, 1-7 GC views per MLN and 1-3 GC views per PP). White, dotted line outlines GCs **(A and B)** based on $BCL6^+$ GC B cell stain (inset only) and pLN primary follicle **(A)** based on IgD^+ FOB cell stain (inset only). Scale bar is 50μm.

CRCs do not require LT or TNF for maintenance of *Cxcl12* expression or network morphology

FDCs require LT and TNF signaling for their maintenance (Fu and Chaplin, 1999; Lu and Browning, 2014; Ngo et al., 1999). To study whether CRCs similarly required intact LT or TNF signaling, we immunized *Cxcl12*-GFP mice with SRBCs and, on day 10, treated them with LTβR-Fc and TNFR-Fc to block signaling from the respective receptors. Four days post-treatment we observed CRC networks still visible in, and predominantly confined to, the T zone proximal side of GCs in spleen, MLN and PP (Fig. 5A, 5B). FDCs, however, no longer expressed CD35 indicating the initial decline of this population as expected with effective blockade (Fig. 5A, 5B)(Fu and Chaplin, 1999). CRC networks retained morphologies similar to those in the saline treated mice, though some splenic GCs additionally contained GFP^+ stromal cells in the T zone distal region of the GC (Fig 5A) and CRC networks in PPs receded slightly towards the serosal surface as a proportion of the GC diameter (Fig. 5A). FDCs in MLN GCs were less affected at this time-point. Therefore, across the tissues, we only quantified CRC presence in GCs with complete loss of CD35 expression on FDCs (Fig. 5B).

To better relate the observed CRC independence from LT and TNF signaling to the well-reported FDC requirement, we attempted to test whether FDCs are lost from the LZ after this short blockade or have just lost expression of essential surface markers. With the same treatment as before, we analyzed the GC stroma in UBI-GFP mice previously reconstituted with WT BM as FDCs would still be detectably GFP^+ in these mice even if they lost CD35 expression. Four days post-treatment, stromal cells were still present throughout the GC in spleen, MLN and PP (Fig. 5C, S3) suggesting

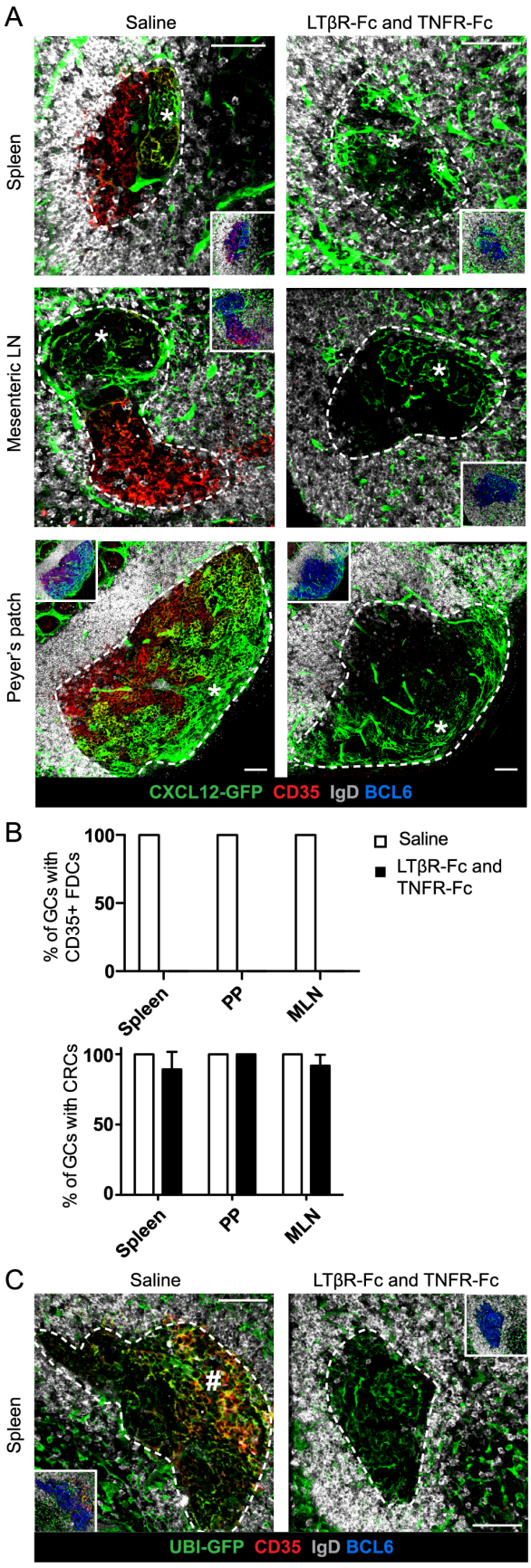
A
Saline
LTβR-Fc and TNFR-Fc
Spleen
Mesenteric LN
Peyer's patch
CXCL12-GFP CD35 IgD BCL6
B
% of GCs with CD35+ FDCs
100
50
0
Spleen
PP
MLN
Saline
LTβR-Fc and TNFR-Fc
% of GCs with CRCs
100
50
0
Spleen
PP
MLN
C
Saline
LTβR-Fc and TNFR-Fc
Spleen
UBI-GFP CD35 IgD BCL6

FIGURE 5. CRCs do not require LT or TNF signaling for maintenance of *Cxcl12* expression or network morphology.
(A) Confocal microscopy images of GC CRC networks (*) in *Cxcl12*-GFP mice immunized with SRBC and, on day 10, treated with 1mg/ml LTβR-Fc and 1mg/ml TNFR-Fc or saline. Mice were analyzed on day 14. **(B)** Percent of GCs containing $CD35^+$ FDCs (top) or CRC networks (bottom). Data from 3 mice treated with saline (6-23 GC views per spleen, 5-14 GC views per MLN, 5-6 GC views per PP) and 4 mice treated with LTβR-Fc + TNFR-Fc (8-26 GC views per spleen, 2-13 GC views per MLN, 2-9 GC views per PP) represented as mean and error bars represent SEM. **(C)** Splenic GCs from UBI-GFP mice reconstituted with WT BM and treated as in (A). Dense, mesh structure of $CD35^+$ FDCs indicated (#). Data are representative of 3 mice treated with saline (9-13 GC views per spleen) and 3 mice treated with LTβR-Fc + TNFR-Fc (10-17 GC views per spleen). **(A and C)** GCs outlined with white, dotted line based on $BCL6^+$ GC B cell stain (inset only). Scale bar is 50μm.

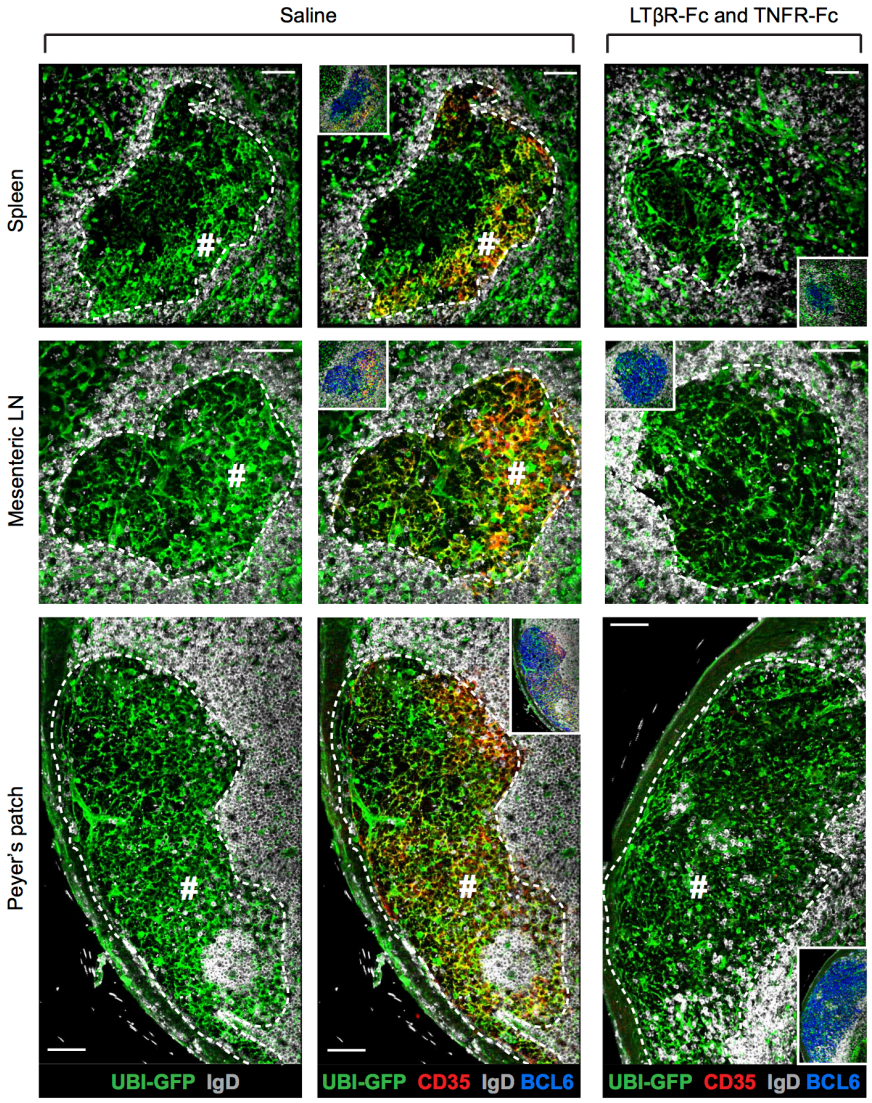

FIGURE S3. Loss of FDC surface markers and altered FDC morphology with blockade of LT and TNF signaling. GCs from UBI-GFP mice reconstituted with WT BM, immunized with SRBC and, on day 10, treated with 1mg/ml LTβR-Fc and 1mg/ml TNFR-Fc or saline. Mice were analyzed on day 14. Dense, mesh structure of CD35+ FDCs indicated (#). For saline, duplicate images with select channels shown. Data are representative of 3 mice treated with saline (9-13 GC views per spleen, 3-7 GC views per MLN, 3-8 GC views per PP) and 3 mice treated with LTβR-Fc + TNFR-Fc (10-17 GC views per spleen, 6-10 GC views per MLN, 2-6 GC views per PP). GCs outlined with white, dotted line based on BCL6+ GC B cell stain (inset only). Scale bar is 50μm.

FDCs were not completely lost. However, the T zone distal GC stroma no longer had the dense, mesh structure of LZ FDCs and instead consisted of dispersed processes with a morphology similar to CRCs (Fig. 5C, S3). We propose that these dispersed networks are former FDCs that have lost CD35 expression and adopted a CRC-like morphology in the absence of LT and TNF signaling. Despite the morphological similarity, we suggest these cells are not expanded CRCs based on our observation that CRCs in LTβR-Fc and TNFR-Fc treated *Cxcl12*-GFP tissues did not expand into the LZ. Thus, in a timeframe when FDCs rely on LT and TNF signaling for functional and structural maintenance, CRCs do not require LT and TNF signaling to maintain *Cxcl12* expression and network morphology.

CXCR4 blockade disrupts CRC distribution in the GC DZ

Since GC B cells must upregulate CXCR4 to travel to the CXCL12-rich DZ (Allen et al., 2004), we investigated whether CXCR4 signaling plays a role in CRC network maintenance. Blockade of CXCR4 with genetic knockout mice or inhibitors causes GC depolarization marked by appearance of FDCs throughout the GC instead of predominantly in the LZ (Allen et al., 2004). We hypothesized that the depolarization of FDCs indicated that either CRCs were converting into FDCs or CRCs were being displaced from the DZ in absence of CXCR4 signaling. To investigate these possibilities, we treated SRBC-immunized *Cxcl12*-GFP mice with the CXCR4 inhibitor 4F-benzoyl-TE14011 or saline for 12 hours via osmotic pumps. Since the half-life of GFP *in vivo* has been estimated to be 26 hours or longer (Corish and Tyler-Smith, 1999), this time point allowed us to assess the conversion of CRCs to FDCs even if the

CRCs no longer expressed *Cxcl12*. As expected with an effective CXCR4 blockade, $CD35^+$ FDCs were detectable throughout GCs in spleen and PPs (Fig. 6). However, the dispersed stroma did not include *Cxcl12*-GFP^+ stroma expressing FDC markers as would have been expected if CRCs were converting to FDCs. Instead, *Cxcl12*-GFP^+ CRC networks were found collapsed against the DZ boundary with the T zone in splenic GCs or against the serosal-proximal lymphatics in PP GCs. Collapse of CRC networks was not observed in the GCs of saline treated mice (Fig. 6). We suggest that CRCs require CXCR4 signaling, likely in GC B cells, for structural maintenance, but not for sustaining phenotypic distinction from FDCs.

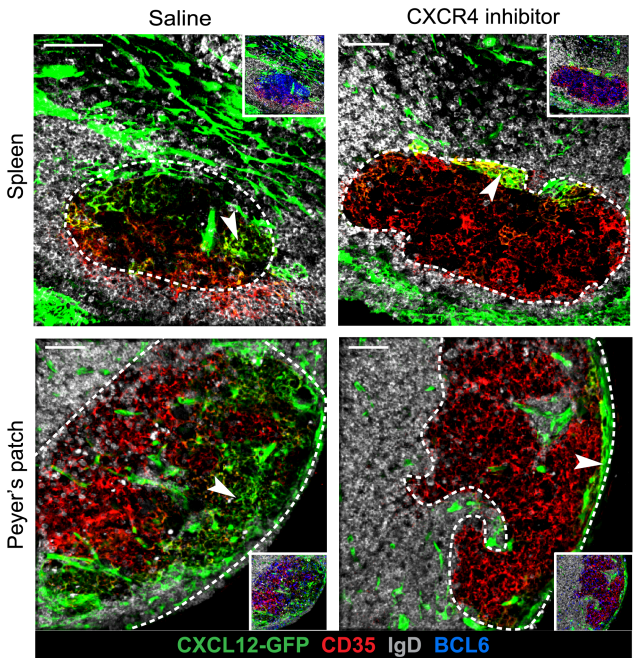

FIGURE 6. **CXCR4 blockade disrupts CRC distribution in the GC DZ**. Confocal microscopy of CRC networks (arrowheads) in splenic and PP GCs of *Cxcl12*-GFP mice after treatment with a CXCR4 inhibitor for 12 hours. GCs outlined with white, dotted line based on $BCL6^{+}$ GC B cells (inset only). Images are representative of 1 mouse treated with saline (6-39 GC views per tissue) and 1-2 mice treated with CXCR4 inhibitor (4-27 GC views per tissue). Similar results found with treatment for 24 hours (1 mouse treated with saline and 1 mouse treated with CXCR4 inhibitor). Scale bar is 50μm.

Discussion

The above findings build from recent work (Bannard et al., 2013) to establish the morphology, distribution, lineage and maintenance requirements of CRCs in splenic, pLN, MLN and PP GC DZs. Our observations that DZ CRCs have low network density and variable morphology are in accord with ultrastructural studies of human tonsil GC stroma which described 'FDCs' in the DZ as half as dense as FDCs in the LZ and lacking in the LZ FDC 'labyrinth-like structure' (Imai and Yamakawa, 1996; Rademakers, 1992). Despite structural differences between CRCs and FDCs, we show GC B cells crawl in and around CRC networks with a motion similar to their activity in FDC networks (Allen et al., 2007b; Wang et al., 2011). These data suggest CRCs could likewise support GC B cells in the DZ niche through structural maintenance of the compartment and direct cell-cell interactions.

While previous studies of human tonsil GCs proposed that DZ stromal cells were a less differentiated form of LZ FDCs (Imai and Yamakawa, 1996; Rademakers, 1992), we find that CRCs and FDCs are already established as distinct populations in both pLN (Bannard et al., 2013) and splenic primary follicles prior to GC formation. The role of CRCs in primary follicles is not yet clear. While naïve B cells have been shown to respond to CXCL12 for entry into pLN and entry and exit from PP (Okada et al., 2002; Schmidt et al., 2013), further study is needed to characterize the effect of CRC-derived CXCL12 on naïve B cell dynamics in the primary follicle and during GC formation.

Our findings in this and previous work (Bannard et al., 2013) that DZ CRCs share almost no canonical surface markers with LZ FDCs or FRCs distinguishes CRCs as a distinct cell type across different lymphoid tissues. Lacking these FDC mediators of

antigen capture and integrin interaction with GC B cells (Wang et al., 2014), DZ CRCs likely make distinct contributions to the GC that meet the specialized requirements for the DZ niche (Allen and Cyster, 2008; Cyster et al., 2000; Shikh and Pitzalis, 2012). In human tonsil and LN, DZ stromal cells have similarly been reported to not express FDC markers, but have been found to express members of the S100a family of intracellular calcium binding proteins (Kasajima-Akatsuka and Maeda, 2006; Maeda et al., 2002; Tsunoda et al., 1999). Future studies will be needed to discern whether murine CRCs express S100a family members uniquely among lymphoid stroma and if they contribute to CRC function in the GC.

We did find that DZ CRCs express the FRC-associated surface glycoprotein, gp38. Recently, gp38 has been described as playing a role in regulating the contraction of the LN FRC network and, as a result, the expansion of the LN after immunization (Acton et al., 2014; Astarita et al., 2015). Whether gp38 has a similar role in regulating FDC and CRC network expansion during GC formation will require future study. Additionally, our combined phenotypic characterization of CRCs as *Cxcl12*-GFP$^+$ gp38$^+$ CD31$^-$ PDGFRβ$^-$ from this and previous work (Bannard et al., 2013) suggests a strategy for flow cytometric separation of CRCs from the other known *Cxcl12*-GFP$^+$ lymphoid stroma. This will likely be useful for investigating CRC-specific expression patterns and functions in the future.

CRCs are likely not the only stromal cells in the GC DZ. We observed that CRCs often only partially occupy GC DZs, that ubiquitous labeling of stroma shows more extensive DZ networks and that gp38$^+$ CD35$^-$ *Cxcl12*-GFP$^-$ reticular networks are visible in pLN DZs. These data support either the presence of an additional stromal cell type or

variable *Cxcl12* expression by CRCs. GC stromal heterogeneity has precedent in an ultrastructural study of human tonsil that described 3 morphological types of DZ 'FDCs' and 4 morphological types of LZ 'FDCs' (Rademakers, 1992). Future study of the prevalence and properties of *Cxcl12*-GFP^{-} DZ stroma will be needed to fully understand their relationship to CRCs and their role in the GC response.

Our lineage tracing experiments conservatively suggest that DZ stromal cells, with morphology, location and surface marker expression similar to CRCs, share a lineage relationship with FDCs, VSCs and FRCs (Mionnet et al., 2013). Recent studies have provided evidence that splenic FDCs develop from perivascular cells (Krautler et al., 2012) whereas LN FDCs develop from marginal reticular cells (MRCs) in the outer region of the follicle (Jarjour et al., 2014). These cell types may similarly function as precursors for CRCs. Previous studies have shown that FDCs and FRCs are both marked by the *Ccl19*-Cre lineage reporter in pLN GCs (Chai et al., 2013; Fasnacht et al., 2014). Our findings suggest that DZ CRC-like stroma share this lineage across tissues. The likely common progenitor for these lymphoid stromal cells is the *Ccl19*-expressing lymphoid tissue organizer (LTo) that functions early in LN development (van de Pavert and Mebius, 2010). However, our finding of heterogeneity in PP FDC labeling may indicate an additional progenitor cell of distinct lineage for this population.

Our finding that DZ CRCs do not require LT and TNF signaling for short-term maintenance of *Cxcl12* expression or network morphology further distinguishes them from LZ FDCs that require these factors for their maturation and maintenance (Fu and Chaplin, 1999; Lu and Browning, 2014; Ngo et al., 1999). Previous work supports the independence of *Cxcl12*-expressing stromal cells from LT and TNF signaling as *Cxcl12*

expression was unaffected in spleens of LT and TNF deficient mice while *Cxcl13* expression was significantly diminished (Ngo et al., 1999). These data do not exclude that DZ CRCs could depend on LT and TNF signaling for other functions.

We demonstrate that DZ CRCs depend on CXCR4, likely in GC B cells, for network distribution. We propose that the collapse of CRC networks after CXCR4 inhibition is due to GC B cells losing attraction to the CXCL12-rich DZ and collecting in the LZ, thus removing structural support from the CRC networks. The substantial hourly exchange of cells between DZ and LZ under normal conditions (Beltman et al., 2011; Victora et al., 2010) supports the possibility that the majority of DZ B cells could relocate to the LZ during the 12-hour inhibition. While DZ CRCs do not acquire an FDC phenotype with CXCR4 inhibition, CRC functions may still be impacted. While it was not possible to investigate the impact of inhibition on non-CRC DZ stroma, the complete occupancy of the GC by FDCs suggests expansion of non-CRC DZ stroma is unlikely to be the cause of CRC collapse.

Production of CXCL12 is likely one of the essential functions of CRCs in the GC DZ. However, most other secondary lymphoid stromal cells, including FRCs, BECs, lymphatic endothelial cells and red pulp fibroblasts, express *Cxcl12* outside the GC (Bannard et al., 2013). Within secondary lymphoid organs, CXCL12 has established roles in promoting B and T cell entry to LNs and PPs (Okada et al., 2002), in supporting DC entry to spleen (Umemoto et al., 2012), in regulating egress from PPs and retention in LNs (Nakai et al., 2014; Schmidt et al., 2013), in aiding vascular development (Griffith et al., 2014) and in guiding plasma cells to the splenic red pulp or LN medulla (Hargreaves et al., 2001). The requirement for different stromal cell sources of CXCL12

in adjacent niches suggest there is tight control over chemokine protein distribution to create the appropriate gradients. For example, in this and previous work (Bannard et al., 2013), we observed *Cxcl12* expression on blood vessels traversing both the LZ and DZ that did not seem to affect GC polarity. This is possibly due to vascular endothelial cells expressing CXCR7, a sink receptor for CXCL12 (Sierro et al., 2007). How CRCs maintain the CXCL12 gradient in the DZ when *Cxcl12* is being expressed in all bordering niches remains an important question for future investigation.

Materials and Methods

Mice and chimeras

C57BL/6 (B6) and B6-CD45.1 mice were obtained from The Jackson Laboratory or the National Cancer Institute. *B6.Cg-Cxcl12*^{tm2Tng} (*Cxcl12*-GFP) gene-targeted mice were backcrossed to the C57BL/6 background more than 7 generations and provided by T. Nagasawa (Ara et al., 2003a; Cyster et al., 2000). *Tg(UBC-GFP)30Scha/J* (UBI-GFP) transgenic mice were backcrossed to the C57BL/6 background for more than 8 generations and were from The Jackson Laboratory (Allen and Cyster, 2008; Cyster et al., 2000; Schaefer et al., 2001; Shikh and Pitzalis, 2012). *B6.Tg(Cr2-Cre)3Cgn* (*CD21*-Cre) BAC-transgenic mice were fully backcrossed to C57BL/6 and provided by K. Rajewsky (Immune Disease Institute, Boston, MA) (Fu and Chaplin, 1999; Kraus et al., 2004; Lu and Browning, 2014; Ngo et al., 1999). *B6.Cg-Gt(ROSA)26Sor*$^{tm6(CAG-Zsgreen1)Hze/J}$ (*R26*-ZsGreen) mice have a CAG promoter, a floxed stop sequence and ZsGreen1 knocked into the Gt(ROSA)26Sor locus and were from The Jackson Laboratory. *C57BL/6N-Tg(Ccl19-cre)*^{489Biat} (*Ccl19*-Cre) BAC-transgenic mice (Chai et al., 2013; Luther et al., 2000; Ngo et al., 1999) were provided by C. Lowell. *Gt(ROSA)26Sor*$^{tm1(EYFP)Cos}$ (*R26*-EYFP) transgenic mice express EYFP from the Gt(ROSA)26Sor locus after Cre-mediated deletion of floxed stop cassette (Link et al., 2007; Srinivas et al., 2001) and were provided by L. Lanier. *Tg(CAG-ECFP)CK6Nagy* (CFP) transgenic mice were backcrossed to the C57BL/6 background more than 5 generations and were from The Jackson Laboratory. *Tg(IghelMD4)4Ccg* (MD4) transgenic mice were fully backcrossed to C57BL/6 and were from an internal colony.

To make bone marrow (BM) chimeras, UBI-GFP mice were treated intraperitoneally (i.p.) with 500µg anti-Thy1.2 (clone 30H12) before being lethally irradiated and reconstituted for at least 8 weeks with wild-type CD45.1 BM. *CD21*-Cre mice were crossed to *R26*-ZsGreen mice and lethally irradiated and reconstituted for at least 8 weeks with wild-type CD45.1 BM as described previously (Bannard et al., 2013; Mueller and Germain, 2009).

Animals were housed in a specific pathogen–free environment in the Laboratory Animal Research Center at the University of California, San Francisco (UCSF), and all experiments conformed to ethical principles and guidelines approved by the UCSF Institutional Animal Care and Use Committee.

Infections and Immunizations

Mice were infected with acute LCMV-Armstrong intravenously (i.v.) at $2.5x10^5$ pfu and analyzed at day 15 for GCs in pLN and spleen (Allen and Cyster, 2008; Clingan and Matloubian, 2013). For induction of spleen GCs, mice were immunized i.p. with $2x10^8$ SRBCs (Colorado Serum Company) on day 0 and day 5 and were analyzed on day 10-12. For induction of pLN GCs, animals were immunized subcutaneously (s.c.) at the shoulders, flanks and above the tail with SRBCs on day 0 and day 5. Draining pLNs (axillary, brachial and inguinal) were analyzed on day 10-12.

Treatments and Transfers

For LTβR and TNFR signaling blockade, *Cxcl12*-GFP mice were immunized i.p. or s.c. with SRBCs on day 0 and day 5 and on day 10 treated i.v. with 100µl each of

1mg/ml mLTβR-huIgG1 (LTβR-Fc, provided by J. Browning) and 1mg/ml TNFR55-huIgG1 (TNFR-Fc, provided by J. Browning) or saline. Tissues were analyzed 4 days later.

For CXCR4 inhibitor treatment, *Cxcl12*-GFP mice were immunized with SRBC i.p. on day 0 and day 5. On day 8, Alzet osmotic pumps (1-day duration, 8.4µl/h pumping rate; Model 2001D; Durect Corporation) loaded with saline or 5mg/ml of the CXCR4 antagonist 4F-benzoyl-TE14011 (Allen et al., 2007a; Tamamura et al., 2003) in saline were implanted dorsally s.c. according to the manufacturer's instructions. As analgesics, Buprenorphine (0.05–0.1 mg/kg, Sigma-Aldrich) was given i.p. before and after surgery, Carprofen (5mg/kg, Pfizer Animal Health) was given i.p. before surgery and Bupivicaine (100µl of 0.25%, Hospira, Inc.) was given topically during surgery. Tissues were analyzed 12 or 24 hours later.

For two-photon laser scanning microscopy (TPLSM) of intact GCs from pLNs and MLNs, *Cxcl12*-GFP mice were immunized with SRBC s.c. on day 0 and day 5. On day 8, mice were injected with 2 mg rabbit IgG anti-PE (200-4199, Rockland) i.p. and 12 hours later injected with 75 µg PE (P-801, Invitrogen Molecular Probes) s.c. as previously described (Allen et al., 2007b; Phan et al., 2007; Wang et al., 2011). On day 9, mice were transferred 1.5 x 10^8 CFP transgenic B cells purified from donor spleens using anti-CD43 microbeads (Miltenyi Biotec) i.v. as previously described (Allen et al., 2004; 2007b). PLNs and MLNs were mounted and imaged 24 hours later.

For TPLSM of PPs, *Cxcl12*-GFP mice were crossed to MD4 mice and transferred with 20% CFP transgenic B cells and 80% CD45.1 WT B cells. B cells were purified from donor spleens as above and 1.2 x 10^7 total B cells were injected i.v. into *Cxcl12*-

GFP MD4 mice. Two weeks later the mice were injected i.v. with 2 x 10^7 purified CD45.1 WT B cells labeled with CellTracker orange 5-(and-6)-(((4-chloromethyl)benzoyl)amino)tetramethylrhodamine (CMTMR, C2927, Invitrogen) as previously described (Allen et al., 2007b; Cyster et al., 2000; Victora and Nussenzweig, 2012). Experiment was repeated as above with transfer of 5% CFP transgenic B cells for 4 weeks and 10% CFP transgenic B cells for 2 weeks with similar results. PPs were mounted and imaged 24 hours later.

Confocal Microscopy

Confocal microscopy was preformed as described previously with some modifications (Bannard et al., 2013). Tissues were fixed in 4% PFA in PBS for 2 hours at 4^{o}C, washed 3 times for 10 min in PBS, then moved to 30% sucrose in PBS overnight. Tissues were flash frozen in TAK tissue-mounting media the following day, and 30μM sections were cut and then dried for 1 hour prior to staining. Sections were rehydrated in PBS with 1% BSA for 10 min and then blocked for 1 hour at room temperature, stained in primary antibody overnight at 4^{o}C and stained for subsequent steps for 2 hours at room temperature all in PBS with 2% mouse serum, 0.1% BSA, 0.3% Triton X-100 and 0.1% NaN3.

For gp38 staining, LNs were fixed in 4% PFA in PBS overnight at 4^{o}C, washed 3 times in PBS, then moved to 20% sucrose in PBS overnight. Sections were processed as above except for rinse in PBS and peroxidase quench in PBS with 0.045% H_2O_2 for 15 min prior to blocking for 30 min. Sections were then stained with primary antibody for 1 hour at room temperature and then with streptavidin–horseradish peroxidase

(Jackson Immunoresearch) for 30 min followed by treatment with the TSA Bioin System tyramide staining kit (Perkin Elmer) according to the manufacturer's instructions. Sections were then stained with remaining secondary antibodies for 1 hour at room temperature. Slides were mounted with Fluoromount-G (Southern Biotech), and images were taken with a Leica SP5 inverted microscope with 40x and 63x oil immersion objectives. Images were analyzed and processed with the Imaris software and the statistics reported are average values with variability represented as standard error of the mean (SEM).

Antibodies, Immunofluorescence and Flow Cytometry

For immunofluorescence, sections were stained with primary antibodies: Rabbit anti-GFP (A11122, Life Technologies), biotin-conjugated anti-CD35 (8C12, BD Pharmingen), goat anti-mouse IgD (goat polyclonal GAM/IGD(FC)/7S, Cedarlane Labs), APC-conjugated anti-TCRβ (457-597, eBioscience), Alexa647-conjugated anti-Bcl6 (K112-91, BD Pharmingen), biotin-conjugated anti-gp38 (8.1.1, Biolegend), APC-conjugated anti-CD21/35 (7E9, Biolegend), rat anti-mouse CD16/32 (FcγRII/III; UCSF Hybridoma Core), biotin-conjugated anti-FDC-M2 (RmC16D2, Cedarlane Labs), rat anti-mouse FDC-M1 (551320, BD Pharmigen), rabbit anti-PDGFRβ (28E1, Cell Signaling, gift from J. Rock), rabbit anti-laminin (L9393, Sigma), rat anti-VCAM1 (553330, BD Pharmingen), rabbit anti-collagen IV (ab19808, AbCam) and Alexa488 conjugated anti-GFP (A21311, Life Technologies, gift from A. Gerard). Sections were then stained with the following secondary antibodies: Alexa488-conjugated donkey anti-rabbit (A-21206, Life Technologies), Alexa555-conjugated streptavidin (S-21381, Life Technologies), AMCA-conjugated donkey anti-goat (705-156-147, Jackson Immunoresearch), biotin-

conjugated donkey anti-rat (712-065-153, Jackson Immunoresearch) and Alexa647-conjugated donkey anti-rabbit (711-606-152, Jackson Immunoresearch).

For flow cytometry, single cell suspensions were generated and stained as previously described (Allen et al., 2007b; Imai and Yamakawa, 1996; Rademakers, 1992). The following antibodies were used for cell staining: APC-Cy7-conjugated CD45R/B220 (RA3-6B2, Biolegend), PerCp-Cy5.5-conjugated anti-IgD (11-26c.2a, Biolegend), Alexa647-conjugated anti-T- and B-Cell Activation Antigen (GL7, Biolegend) and PE-Cy7-conjugated Fas (Jo2, BD Biosciences/Fisher). Samples were acquired and analyzed with a BD LSR II and Flowjo (Treestar).

Two-photon laser-scanning microscopy

Explant pLNs, MLNs and PPs were prepared for TPLSM as previously described for explant pLN (Allen et al., 2007b; Lefevre et al., 2007) except that PP were mounted with the serosal side face-up. PPs were stabilized in a customized plastic coverslip window with Vetbond tissue glue (3M) to counter the peristaltic motion of the small intestine. The temperature at the PP during and at the end of several imaging sessions was measured using a dual-temperature controller (TC-344B, Warner Instruments) equipped with a CC-28 cable containing a bead terminator and was found to remain between 36–37 ^{o}C.

Images were acquired with ZEN2012-Black Edition (Carl Zeiss) using a 7MP two-photon microscope (Carl Zeiss) equipped with a Chameleon laser (Coherent). For video acquisition from MLNs and pLNs, a series of planes of 0.5μm (MLN) or 1μm (pLN and primary follicle pLN) Z-spacing spanning a depth of 190–260μm were collected. Each

XY plane spans 283.40μm × 283.40μm at a resolution of 0.55μm per pixel (MLN, primary pLN) or 327.00μm × 327.00μm at a resolution of 0.64μm per pixel (pLN). Some images have been cropped in XY plane for optimal visualization. Excitation wavelength was 920nm. For video acquisition from PPs, a series of planes of 3μm Z-spacing spanning a depth of 50–100μm were collected every 15–30s. Each XY plane spans 425.10μm × 425.10μm at a resolution of 0.83μm per pixel or 212.55μm × 212.55μm at a resolution of 0.42μm per pixel. Excitation wavelength was 870nm. For all TPLSM imaging, emission filters were <452nm for second harmonic, 460-480nm for CFP, 500–550nm for GFP and 570–640nm for CMTMR. Videos were made and analyzed with Imaris 7.4.2 364 (Bitplane).

To track cells, surface seed points were created and tracked over time. Tracks were manually examined and verified. Data from cells that could be tracked for at least 10 min were used for analysis. Tracking data were analyzed in Microsoft Excel with a custom macro written in Microsoft Visual Basic for Applications as previously described (Allen et al., 2004; 2007b). Movies were adjusted for tissue drift in Imaris 7.4.2 364 (Bitplane) and annotation and final compilation of videos were performed with iMovie (Apple). Video files were saved as .mov (Quicktime).

Acknowledgements

We thank Y. Xu and J. An for technical assistance, A. Reboldi and H. Chen for help with TPLSM and confocal microscopy, A. Reboldi for helpful discussion, M. Matloubian for the LCMV-Armstrong, T. Nagasawa for the *Cxcl12*-GFP mice, C. Lowell for the *Ccl19*-Cre mice, L. Lanier for the *R26*-EYFP mice, K. Rajewsky for the *CD21*-Cre mice, A. Lechner and J. Rock for the PDGFRβ antibody, A. Mujal and A. Gerard for the Alexa488 conjugated anti-GFP antibody and J. Browning for LTβR-Fc and TNFR-Fc.

CHAPTER 3

Single-cell RNA sequencing of lymph node stromal cells reveals niche-associated heterogeneity

As of submission this chapter is under review as:

Rodda L.B., Lu E., Bennett M.L., Sokol C.L., Wang X., Luther S.A., Barres B.A., Luster A.D., Chun J.Y., and Cyster J.G. Single-cell RNA sequencing of lymph node stromal cells reveals niche-associated heterogeneity. *Immunity* (Under Review 2017 Nov. 25).

Abstract

Stromal cells establish the compartmentalization of lymphoid tissues critical to the immune response. However, the full diversity of lymph node (LN) stromal cells remains undefined. Using droplet-based single-cell RNA sequencing we identified transcriptional profiles for 8 non-endothelial stromal cell subsets from peripheral LNs. This included the established T-zone reticular cells (TRCs), marginal reticular cells, follicular dendritic cells (FDCs) and perivascular cells. We also identified novel clustering of cholesterol-25-hydroxylase (Ch25h)$^{+}$ Ccl19^{lo} TRCs enriched at the T-zone perimeter, Cxcl9^{+} TRCs in the T-zone, CD34^{+} stromal cells (SCs) in the capsule and medullary vessel adventitia and indoethylamine methyltransferase (Inmt)$^{+}$ SCs enriched in the medullary cords. Tmem119, parathyroid hormone like hormone (Pthlh) and Sox9 were validated as novel FDC markers and, using data from LCMV-infected mice, Sox9 was also validated as a marker of germinal center CXCL12-expressing reticular cells. These transcriptional profiles enable exploration of niche-associated stromal functions, stromal activation states and stromal development.

Introduction

Lymph nodes (LNs) are organized into discrete niches to support the efficient antigen encounter and lymphocyte activation required for an effective adaptive immune response (Mueller and Germain, 2009). The stromal cells that pattern these niches contribute to both their structural and functional specificity. Stromal cells influence lymphocyte survival, migration, antigen encounter and tolerance (Chang and Turley, 2015; Malhotra et al., 2013; Roozendaal and Mebius, 2011; Schulz et al., 2016). The existence of stromal cells in lymphoid tissues was initially recognized through ultrastructure studies that detected large numbers of fibroblastic cells forming a reticular meshwork. These cells became known as fibroblastic reticular cells (FRCs) (Cyster et al., 2000; Mueller and Germain, 2009). Early studies also identified antigen-trapping cells with dendritic morphology within follicles that became known as follicular dendritic cells (FDCs) (Allen and Cyster, 2008; Cyster et al., 2000; Imai and Yamakawa, 1996). Podoplanin (PDPN, gp38) was established as a stroma-specific marker allowing the network of FRCs throughout the T-zone and follicle to be stained and stromal functions studied (Farr et al., 1992; Link et al., 2007; Onder et al., 2011).

One such function is to guide lymphocytes into distinct niches through the expression of chemokines. B cells cluster in follicles as a result of follicular stromal cells (FSCs), $CR2^{+}$ FDCs and $RANKL^{+}$ (Tnfsf11) marginal reticular cells (MRCs) expressing CXCL13. FSCs surround the FDC network in follicles and the MRCs sit at the edge of the follicle adjacent to the subcapsular sinus (SCS) (Cyster et al., 2000; Katakai et al., 2004; Mueller and Germain, 2009). Recent work identified an additional stromal cell type found at the T-zone proximal side of primary follicles and in the germinal center

(GC) dark zone (DZ) termed *Cxcl12*-expressing reticular cells (CRCs) (Bannard et al., 2013; Rodda et al., 2015). These cells have fine dendritic processes like FDCs, but lack most FDC markers. Their functional properties beyond CXCL12 production are unknown.

CCL21 and CCL19-expressing stromal cells termed T-zone reticular cells (TRCs) populate the T-zone and attract $CCR7^+$ lymphocytes (Bajénoff et al., 2006; Cyster, 2005; Link et al., 2007). In addition to making chemokines, TRCs produce trophic factors such as IL7 and maintain the extracellular matrix (ECM)-rich conduit network that provides structural support to lymphoid tissues and allows rapid diffusion of small molecules throughout the tissue (Link et al., 2007; Mueller and Germain, 2009). Adding to the complexity of the T-zone stroma is the cortical ridge, a specialized region of the outer T-zone bordering the follicle (Katakai et al., 2004). Whether the stromal cells in this region differ from the rest of the TRCs has been unclear.

LNs contain another niche, the medulla, which comprises of lymphatic sinuses weaving around medullary cords structured by medullary reticular cells (MedRCs). Cells can enter and exit the LN through the medullary cords, which are populated by macrophages and plasma cells. While MedRCs highly express CXCL12 (Bannard et al., 2013; Hargreaves et al., 2001), little else is known about them including no specific, positive markers.

Finally, blood vessels including high endothelial venules (HEVs) thread through the node bringing nutrients and leukocytes to the anlagen (Girard et al., 2012). $ITGA7^+$ perivascular cells (PvCs), including pericytes and vascular smooth muscle cells (vSMCs), surround and support the blood endothelial cells that make up these vessels

(Armulik et al., 2011). $CD34^+$ adventitial cells have been described to surround PvCs supporting large vessels in the LN medulla (Díaz-Flores et al., 2014; Sitnik et al., 2016).

By flow cytometry, LN stromal cells have been partitioned based on PDPN and CD31 (PECAM1) expression into $PDPN^+CD31^-$ FRCs, $PDPN^-CD31^-$ double negative cells (DNCs), $PDPN^+CD31^+$ lymphatic endothelial cells (LECs) and $PDPN^-CD31^+$ blood endothelial cells (BECs) (Link et al., 2007). The Immgen consortium has reported the gene expression pattern of FRCs, DNCs, LECs and BECs (Malhotra et al., 2012). This work provided important insight into the possible chemokine, cytokine and extracellular matrix (ECM) contributions of FRCs, and the contribution of PvCs to the DNC signature (Malhotra et al., 2012). However, based on staining of LN sections, the FRC population includes at least TRCs, MRCs, FDCs and MedRCs, each of which serve the needs of a different LN niche.

We set out to advance understanding of the heterogeneous lymphoid stromal cell populations and in particular learn more about rare stromal cell types, such as FDCs, whose transcriptomes are obscured in bulk assessments. We used droplet-based single-cell RNA (scRNA) sequencing to capture gene expression data from 2,732 peripheral LN (pLN), non-endothelial stromal cells. We identified 8 stromal clusters, revealing a greater degree of heterogeneity in the FRC and DNC populations than previously appreciated. Based on these profiles, we were able to associate novel clusters with specific niches and validate novel markers for MedRCs and FDCs.

Results

Single-cell RNA sequencing revealed eight clusters of lymph node, non-endothelial stromal cells

In order to investigate the heterogeneity of mouse pLN stromal cells we performed droplet-based scRNA sequencing. We collagenase-digested mouse inguinal, brachial and axillary LNs and depleted $CD45^+$ cells. We then ran FACS-isolated $CD45^-$ $CD31^-$ cells on the 10X Chromium instrument for single-cell mRNA capture and on the HiSeq4000 for Illumina sequencing (Fig. 1A). After quality control, we retained 2,870 cells with 5,542 median unique transcripts detected per cell and 2,148 median genes detected per cell. Using Seurat (Satija et al., 2015), we performed unsupervised, graph-based clustering and t-distributed stochastic neighbor embedding (tSNE) to characterize and visualize transcriptional heterogeneity amongst the LN cells (Fig. S1A).

We identified the majority of cells (95.2%) as $Pdgfr\beta^+$ and/or $Pdgfr\alpha^+$ stromal cells. The remaining cells formed distinct, minor populations of neutrophils (*Lyz2*$^+$), mast cells (*Mcpt8*$^+$), BECs (*Clnd5*$^+$), LECs (*Lyve1*$^+$), Schwann cells (*Mbp*$^+$) and keratinocytes (*Krt18*$^+$) as defined by their top differentially expressed markers (Fig. S1A, Table S1). These cells may have been included because of low CD45 expression, low CD31 expression or sorting impurity. The Schwann cells likely represent pLN nerve fiber associated cells. These cell types were not further studied here.

To increase the resolution on $Pdgfr\beta^+$ and/or $Pdgfr\alpha^+$ non-endothelial stromal cell transcriptional heterogeneity, we excluded the minor Pdgfrβ- Pdgfrα- populations and repeated the graph-based clustering on the remaining 2,732 cells. Since MRCs were not resolved with this unsupervised clustering, possibly because their marker genes

were lowly expressed, we used least absolute shrinkage and selection operator (LASSO) supervised clustering (Satija et al., 2015) to add landmark LN stromal genes curated from the literature (Table S2) to the highly variable genes being used to guide the graph-based clustering. This allowed us to resolve MRCs (as determined below) along with the other clusters previously identified in the unsupervised assessment.

In the interest of studying GC stromal cells, we performed the same droplet-based scRNA sequencing and analysis on CD45- CD31- pLN stromal cells from mice at day 15 post-infection with LCMV-Armstrong. At this time-point, large GCs have formed and the LNs have reached their peak cellularity, while the LCMV has been cleared and the percentage of $CD45^-$ $VCAM1^+$ $PDPN^+$ stromal cells has almost recovered from the infection (Mueller et al., 2007; Rodda et al., 2015; Scandella et al., 2008). By this time point the B and T-zone organization orchestrated by these chemokines is recovered (Mueller et al., 2007; Rodda et al., 2015; Scandella et al., 2008). In our dataset, we found the expression of *Cxcl13*, *Ccl19* and *Ccl21* by the post-infection stromal cells were within 2-fold of the uninfected controls by day 15 (Fig. S1B).

Since most of the stromal cells are recovered at this time point post-infection, we combined the uninfected and post-infection datasets to identify the stromal clustering conserved between them. After quality control, we retained 12,713 post-infection pLN cells with 4,477 median unique transcripts detected per cell and 1,937 median genes detected per cell. Removing Pdgfrβ- Pdgfrα- cells as before, 12,064 non-endothelial stromal cells were used for further analysis. To identify conserved clusters between the uninfected and post-infection cells, we combined the datasets for diagonal Canonical Correlation Analysis (CCA) (Butler and Satija, 2017). Using the expression of

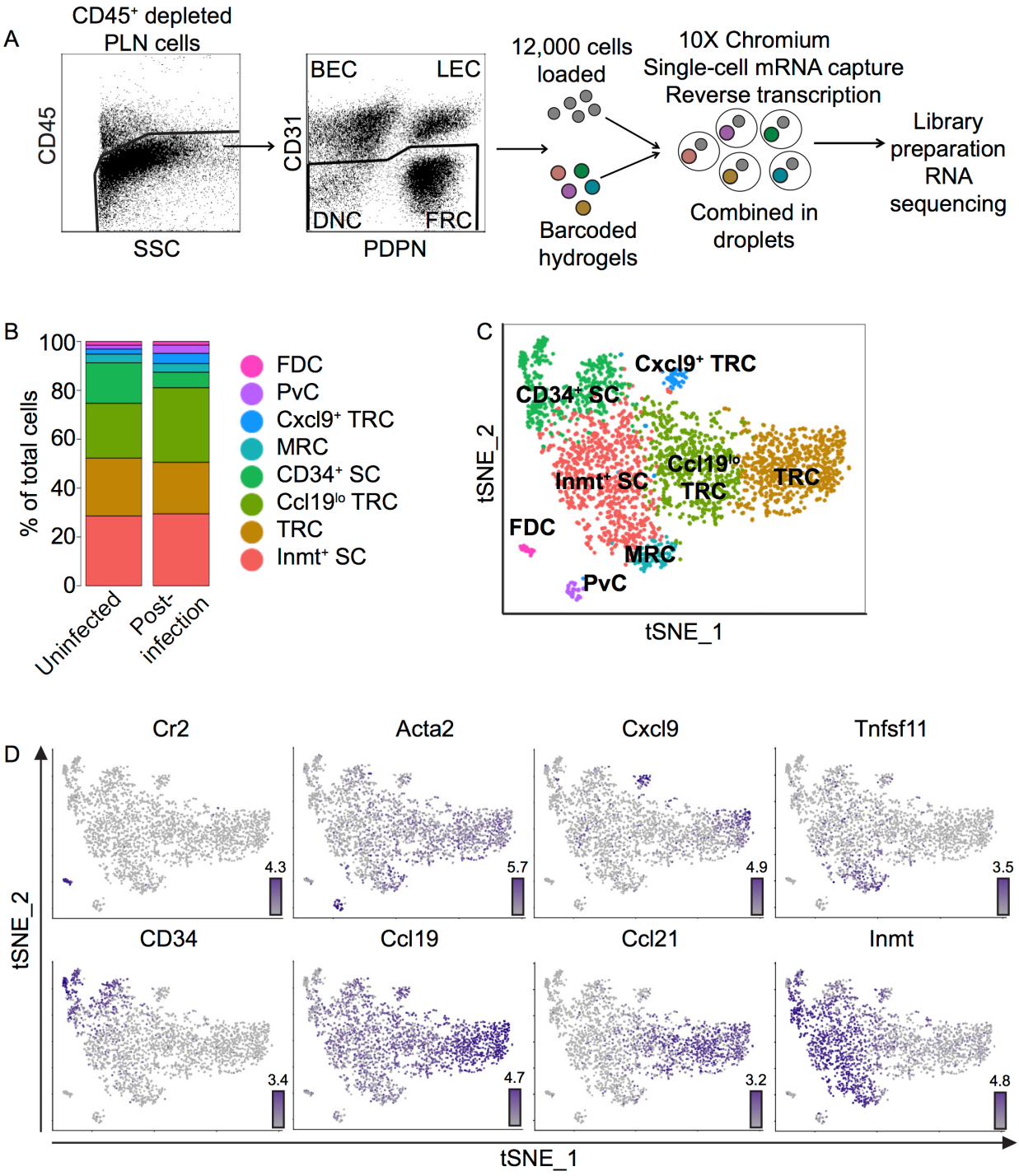
A
CD45⁺ depleted PLN cells
CD45
SSC
BEC
LEC
CD31
DNC
FRC
PDPN
12,000 cells loaded
Barcoded hydrogels
10X Chromium
Single-cell mRNA capture
Reverse transcription
Combined in droplets
Library preparation
RNA sequencing
B
% of total cells
100
80
60
40
20
0
Uninfected
Post-infection
FDC
PvC
Cxcl9⁺ TRC
MRC
CD34⁺ SC
Ccl19ˡᵒ TRC
TRC
Inmt⁺ SC
C
Cxcl9⁺ TRC
CD34⁺ SC
Inmt⁺ SC
Ccl19ˡᵒ TRC
TRC
FDC
MRC
PvC
tSNE_2
tSNE_1
D
Cr2
Acta2
Cxcl9
Tnfsf11
4.3
5.7
4.9
3.5
CD34
Ccl19
Ccl21
Inmt
3.4
4.7
3.2
4.8
tSNE_2
tSNE_1

Figure 1. Identification of eight pLN, non-endothelial stromal clusters by scRNA sequencing

(A) Work-flow of droplet-based scRNA sequencing. CD45-depleted, sorted, $CD45^-$ $CD31^-$ pLN stromal cells from C57BL/6 mice were run on the 10X Chromium and then processed for sequencing. (B) Proportions of the 8 non-endothelial stromal cell clusters in two datasets: uninfected pLN stroma (Uninfected) and CCA aligned day 15 post-LCMV-Armstrong infection pLN stroma (Post-infection). See also Fig. S1. (C) Semi-supervised, graph-based clustering of uninfected, non-endothelial stromal cells visualized with tSNE. Each point represents a single cell (droplet barcode) colored by cluster assignment. (D) Expression of marker genes used to distinguish the 8 stromal clusters projected onto tSNE plots. Color scaled for each gene with highest log-normalized expression level labeled above the key.

variable genes from both datasets, a shared gene correlation structure was identified that explained more than 50% of the variance of 96.4% of uninfected cells and 98.4% of post-infection cells. The remaining cells were considered ‘dataset specific’ and removed. Based on the cluster assignments of the removed cells from analysis of the datasets separately, the maximum percentage of cells found to be dataset specific was 24% (post-infection FDCs) (Fig. S1C). The cells adequately described by the structure were then aligned in a conserved low-dimensional space (mean gene expression compared between datasets, $r = 0.99$, p-value $< 2.2 \times 10^{-16}$, Pearson correlation; Fig. S1D).

Repeating the unsupervised, graph-based clustering as above revealed 8 conserved clusters with similar proportional representation in each dataset (Fig. 1B, S1E). We chose the clustering resolution that grouped the cells into the maximum number of clusters where each cluster had at least 20 genes more than 2-fold differentially expressed (FDR < 0.05) between the average expression by cells in the cluster and the average expression by cells not in the cluster. The genes also had to be expressed in at least 10% of the cells in the cluster of interest. We have included the averaged gene expression profile for each cluster in the uninfected and aligned post-infection datasets in the Supplemental Table S3. In order to include all the quality-controlled, non-endothelial stromal cells detected in the uninfected dataset, we pursued analysis of these cells and their clustering separately from their post-infection counterparts (Fig. 1C, Fig. S1F).

Based on the distinguishing expression profiles of the 8 stromal cell clusters, which could represent distinct cell types or cell states, we were able to suggest

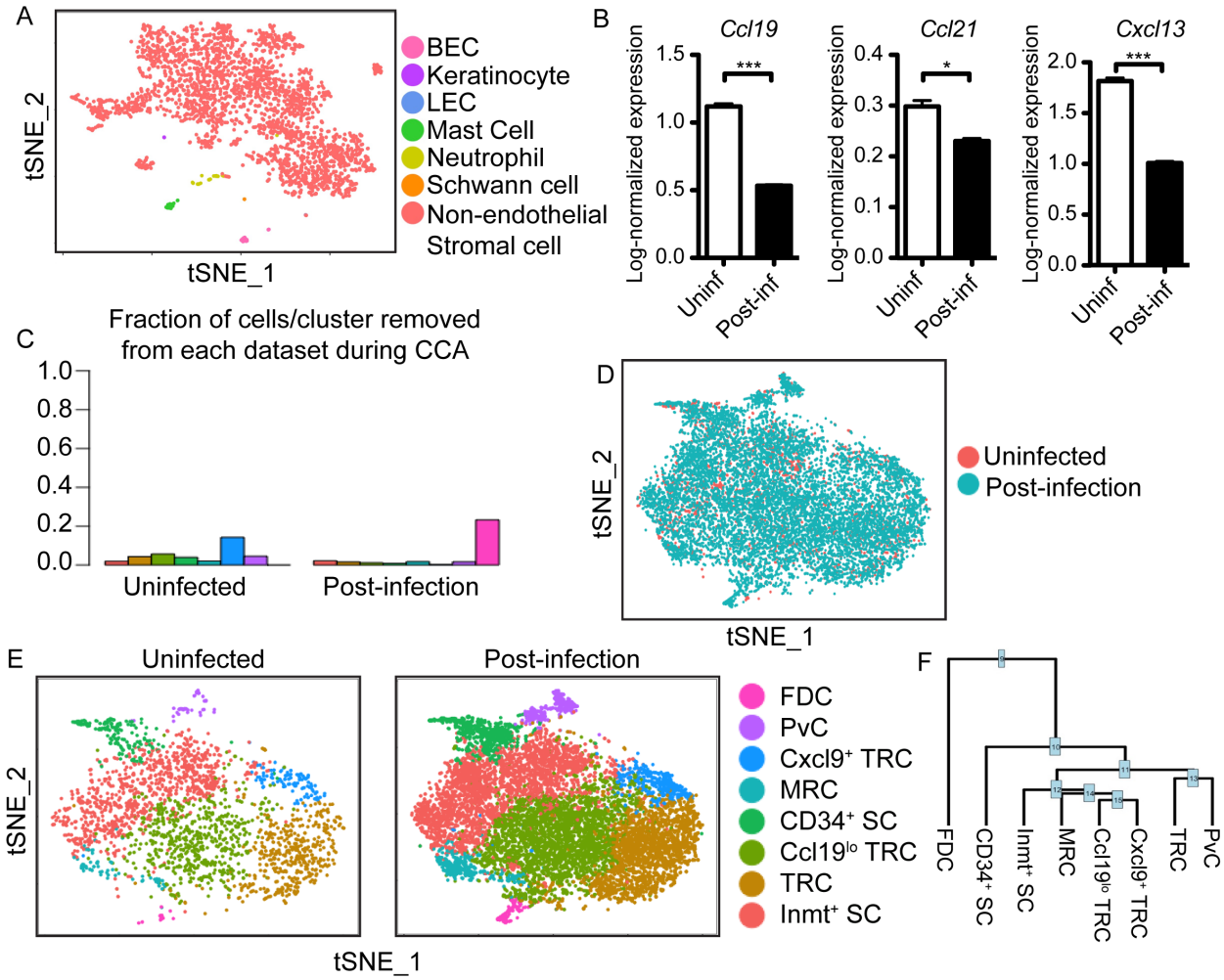

Figure S1. Eight pLN, non-endothelial stromal clusters conserved between uninfected and post-infection samples. Related to Figure 1.

(A) Unsupervised, graph-based clustering of scRNA sequencing data visualized with tSNE. Non-endothelial Stromal cells (Pdgfrβ$^+$ and/or Pdgfrα$^+$) were used in subsequent analyses. Each point represents a single cell (droplet barcode) colored by cluster assignment. (B) Log-normalized expression of *Ccl19*, *Ccl21* and *Cxcl13* by non-endothelial stromal cells isolated from uninfected (Uninf) and day 15 post-LCMV infection pLNs (Post-Inf). Data represents mean and error bars indicate SEM (* $p < 0.01$, *** $p < 0.0001$; Mann-Whitney U test). (C) Distribution of dataset specific cells removed during CCA and grouped by cluster assignments from analysis of the datasets separately. Clusters colored as in E. (D) tSNE visualization of CCA alignment of uninfected and post-infected pLN, non-endothelial stromal cells. (E) Graph-based clustering of the aligned datasets visualized with tSNE with the cells from each dataset plotted separately and colored by conserved cluster assignment. (F) Hierarchical clustering of the uninfected non-endothelial stromal cells demonstrating the distance matrix in gene expression space between an averaged cell from each cluster.

assignment of several of the clusters to previously described niche-associated stromal cell types. We identified Tnfsf11^{+} MRCs, Cr2^{+} FDCs, Itga7^{+} Acta2^{+} PvCs and Ccl19^{+} TRCs (Fig. 1D). The proportions of these cells in our sample corresponded to expectations based on sectioning and flow cytometric work (Jarjour et al., 2014; Link et al., 2007) (Fig.1B). The TRCs contained heterogeneity that has not been previously described and the subsets could be distinguished as Ccl21^{+} Ccl19^{hi} TRCs, Ccl21^{+} Ccl19^{lo} Tnfsf13b^{hi} TRCs and Ccl19^{lo} Cxcl9^{+} TRCs. We also found two additional clusters that could be distinguished as Inmt^{+} CD34^{-} Tnfsf11^{-} stromal cells (Inmt^{+} SCs) and CD34^{+} SCs (Fig. 1D). These markers also distinguished the clusters of aligned post-infection cells and the mean expression profile for each cluster was highly correlated between the uninfected and aligned post-infected samples ($r > 0.96$, p-value $< 2.2 \times 10^{-16}$, Pearson correlation; Fig. S2, Table S3).

To study the clusters further, we identified differentially expressed genes (DEGs) (log2-fold change >1, FDR < 0.05, percent in cluster expressing > 10%) for each cluster of uninfected, non-endothelial stromal cells (Fig. 2A, Table S4-S11). Comparing numbers of DEGs, FDCs were the most distinct with 660 DEGs and Ccl19^{lo} TRCs the least distinct with 24 DEGs (Fig. 2B). We found significant overlap of the DEGs for each cluster between the uninfected and post-infection samples ($p < 1 \times 10^{-20}$ for all pairwise cluster comparisons, hypergeometric test). In contrast, some canonical stromal genes, such as Pdpn, Pdgfrα and Pdgfrβ, were insufficient to distinguish the clusters (Fig. 2C). We proceeded to investigate the distinctive features of each cluster of uninfected, pLN, non-endothelial stromal cells.

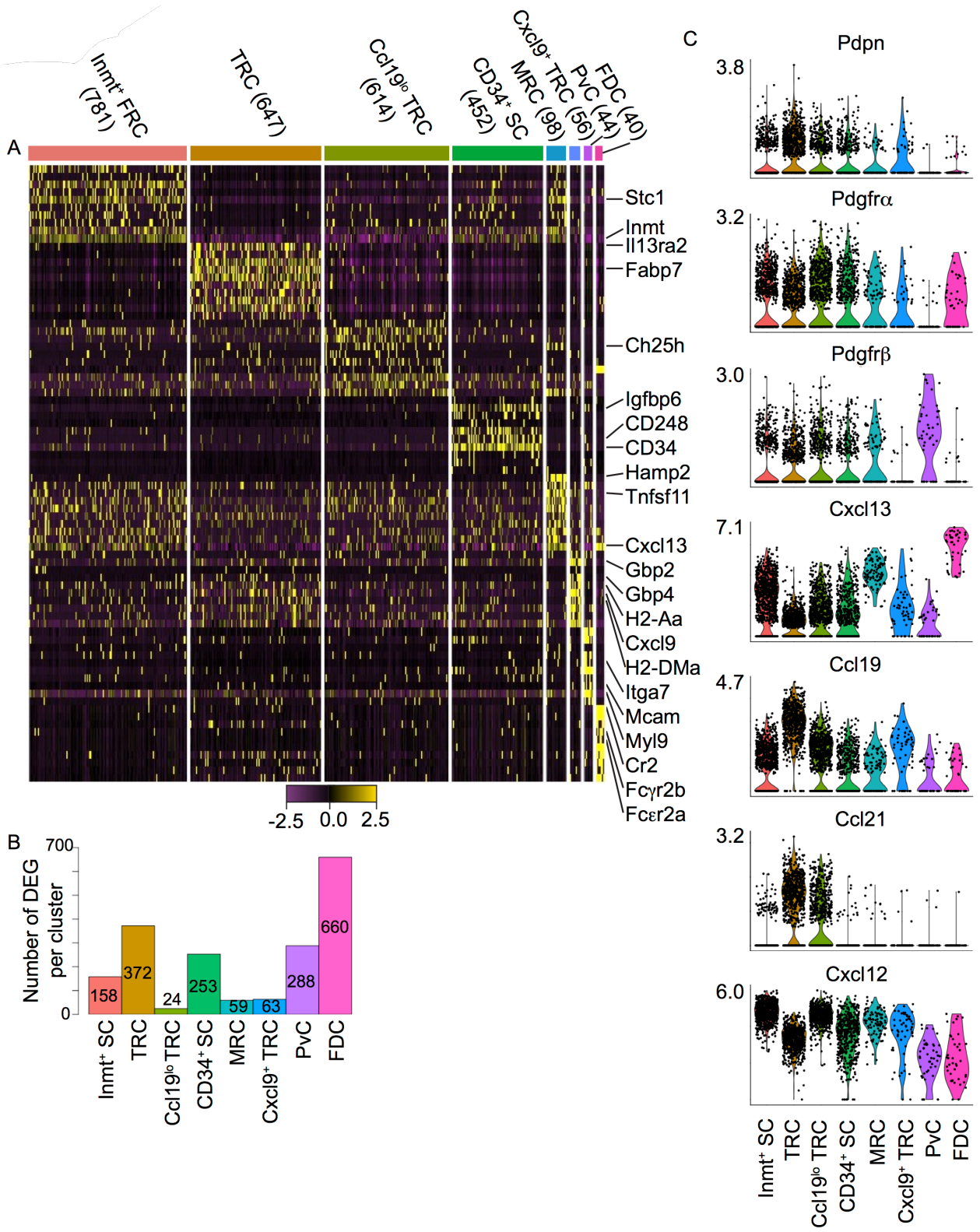
A
Inmt+ FRC (781)
TRC (647)
Ccl19lo TRC (614)
CD34+ SC (452)
Cxcl9+ TRC MRC (98)
PvC (56)
FDC (44)
(40)
Stc1
Inmt
Il13ra2
Fabp7
Ch25h
Igfbp6
CD248
CD34
Hamp2
Tnfsf11
Cxcl13
Gbp2
Gbp4
H2-Aa
Cxcl9
H2-DMa
Itga7
Mcam
Myl9
Cr2
Fcγr2b
Fcεr2a
-2.5 0.0 2.5
B
Number of DEG per cluster
700
0
158
372
24
253
59
63
288
660
Inmt+ SC
TRC
Ccl19lo TRC
CD34+ SC
MRC
Cxcl9+ TRC
PvC
FDC
C
Pdpn
3.8
Pdgfrα
3.2
Pdgfrβ
3.0
Cxcl13
7.1
Ccl19
4.7
Ccl21
3.2
Cxcl12
6.0
Inmt+ SC
TRC
Ccl19lo TRC
CD34+ SC
MRC
Cxcl9+ TRC
PvC
FDC

Figure 2. Differential gene expression of eight pLN, non-endothelial stromal clusters

(A) Single-cell expression heatmap displaying the expression in each uninfected pLN non-endothelial stromal cell (columns) of the top 10 differentially expressed genes (DEGs) per cluster (rows) (log2foldchange >1, FDR < 0.05, percent of cells expressing the gene within the cluster > 10%). Select genes are labeled and log-normalized expression scaled for each gene across all cells reported by color. Cluster name and the number of cells in the cluster displayed above. See also Fig. S2. (B) Number of DEGs found for each cluster. (C) Violin plots of canonical stromal gene expression grouped by cluster. Each point is a single cell. Highest log-normalized expression value is labeled on the y-axis for each gene.

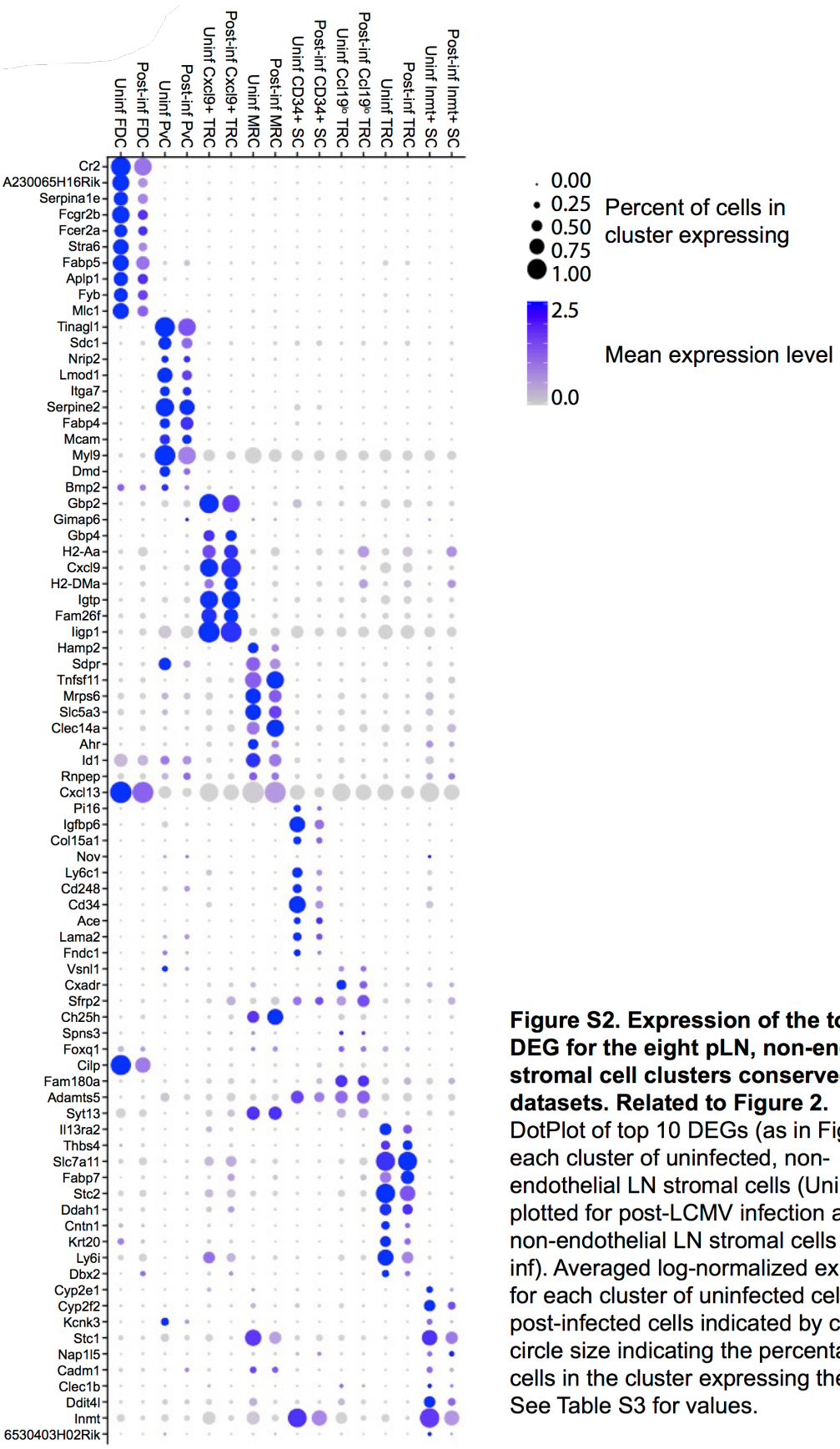

Figure S2. Expression of the top 10 DEG for the eight pLN, non-endothelial stromal cell clusters conserved across datasets. Related to Figure 2.
DotPlot of top 10 DEGs (as in Fig. 2A) for each cluster of uninfected, non-endothelial LN stromal cells (Uninf) also plotted for post-LCMV infection aligned non-endothelial LN stromal cells (Post-inf). Averaged log-normalized expression for each cluster of uninfected cells or post-infected cells indicated by color with circle size indicating the percentage of cells in the cluster expressing the gene. See Table S3 for values.

TRC expression suggests additional mechanisms for lymphocyte support and conduit maintenance

TRCs are stromal cells that support the LN T-zone and have been among the most in depth studied LN stromal cells (Mueller and Germain, 2009). TRCs express CCL19 and CCL21 for the attraction of leukocytes into the T-zone (Cyster, 2005; Fletcher et al., 2015; Mueller and Germain, 2009). TRCs support naïve, effector and memory T cells by producing IL7 (Link et al., 2007). Since we found these features enriched on cells in two of the clusters, we deemed these TRCs and Ccl19^{lo} TRCs (Fig.1D, 2C, Table S3 and S4); the latter will be discussed in more detail in the next section. We also identified a third cluster as a subset of TRC because they were enriched for *Ccl19* expression in the uninfected sample and a portion of the cells expressed *Ccl19*, *Ccl21* and *IL7* in the post-infection sample (Fig. 2C, Table S3). We have termed these Cxcl9^{+} TRCs and will discuss them in detail in a subsequent section.

Cells in the TRC cluster expressed multiple surface and secreted molecules that could augment interactions with T cells and DCs. As shown previously, TRCs expressed *Pdpn*, which supports DC motility and signaling from DCs to TRCs during LN expansion (Acton et al., 2014; Astarita et al., 2015) (Fig. 2C). TRCs had almost exclusive expression of *IL13ra2*, an IL13 receptor chain that is thought to act as a decoy receptor for IL13 signaling, perhaps limiting the signaling of this type 2 cytokine in the T-zone microenvironment (Fichtner-Feigl et al., 2006; Zhang et al., 1997) (Fig. 2A, S3). TRCs were also enriched in our dataset for *Cx3cl1*, the chemokine ligand for CX3CR1^{+} activated CD8^{+} T cells, macrophages, monocytes and recently described T-zone macrophages (Baratin et al., 2017) (Fig. S3). Staining for CX3CL1 has been previously

shown in the LN T-zone, SCS and interfollicular regions (IFR) and is expressed by BECs and DCs, but has not been attributed to TRCs (Johnson and Jackson, 2013; Kanazawa et al., 1999). *IL4i1* was enriched in TRCs and FDCs and has not been previously described in stromal cells (Fig. S3). IL4i1 is an L-amino acid oxidase induced by IL4 in B cells *in vitro* (Chu and Paul, 1997) can inhibit the $CD8^+$ T cell anti-tumor response *in vivo* (Lasoudris et al., 2011) and may have antibacterial properties (Puiffe et al., 2013).

TRCs make critical components of the reticular conduit network and themselves ensheath the conduits (Mueller and Germain, 2009; Sixt et al., 2005). Highlighted previously as expressed by FRCs, we found TRCs specifically expressed collagen 14 (*Col14a1*) and fibromodulin (*Fmod*), components of the conduit core (Malhotra et al., 2012) (Fig. S3). Previously DNCs had been reported to express higher *Col12a1* than TRCs (Malhotra et al., 2012), but we see *Col12a1* expression enriched in TRCs and do not detect expression on any of the $Pdpn^{lo}$ clusters in our data (Fig. S3). Along with enrichment for expression of cadherin 11 (*Cdh11*), previously suggested to support FRC-FRC interactions (Malhotra et al., 2012), we found TRCs expressed desmocolin-2 (*Dsc2*), a cadherin-type protein, that functions to link adjacent cells together through desmosomes (Fig. S3) (Jarjour et al., 2014). TRCs also expressed the latrophilin adhesion-type GPCR *Adgrl3* (Lphn3) and one of its ligands *Flrt3* that might act in cell-cell adhesion (O'Sullivan et al., 2012) (Fig. S3).

We also identified factors possibly involved with TRC development and maintenance. TNF family molecules have strong influences on TRCs (Lu and Browning, 2014) and we found these cells expressed *Nradd* and shared *Relt* (*Tnfrsf19l*) and

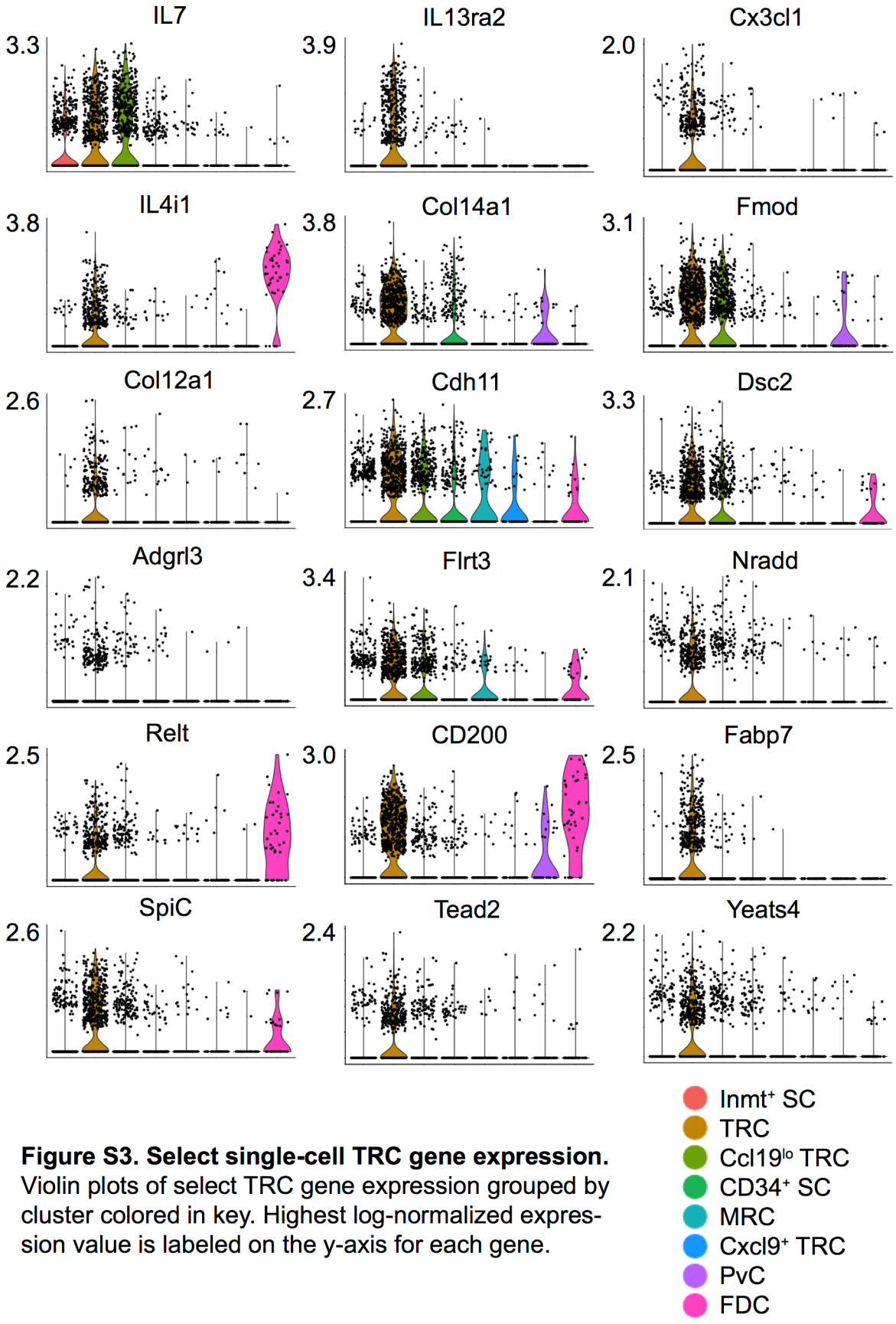

Figure S3. Select single-cell TRC gene expression. Violin plots of select TRC gene expression grouped by cluster colored in key. Highest log-normalized expression value is labeled on the y-axis for each gene.

CD200 expression with a majority of FDCs (Fig. S3). We found TRCs specifically expressed *Fabp7*, a transport protein for fatty acids, eicosanoids, retinoids and other lipophilic molecules that may function to deliver lipids to nuclear hormone receptors (Fig. 2A, Fig. S3). In accord with these data, an immunofluorescence study demonstrated Fabp7 protein expression is restricted to TRCs in LNs and spleen (Tokuda et al., 2010). Finally, we found TRCs were enriched for expression of the transcription factors *SpiC*, *Tead2* and *Yeats4* among others (Fig. S3). These factors may have roles in TRC development. Our findings support the known TRC roles in cell localization, trophic support for T cells and DCs and building the conduit matrix while suggesting additional mechanisms to fulfill these roles.

Ch25h-expresssing Ccl19^{lo} TRCs populate the follicle/T-zone interface and IFRs

The Ccl19^{lo} TRC cluster expressed features of both the T cell-zone and B cell follicle and was the least transcriptionally distinct cluster. In particular, Ccl19^{lo} TRCs expressed *Ccl21* and *Cxcl13*, though below FDC expression of *Cxcl13* (Fig. 2C). They expressed *IL7* and *Baff* (*Tnfsf13b*), a cytokine critical for B cell survival (Fig. 3A, S3). *Baff* expression by FRCs has been previously described and associated with the B cell follicle (Cremasco et al., 2014). In our analysis, TRCs and Inmt^{+} SCs also expressed high levels of *Baff* (Fig. 3A).

Ccl19^{lo} TRCs were enriched for *Ch25h* expression along with MRCs (Fig. 3A). This enzyme is important for generation of the EBI2 ligand, 7α,25-HC, which helps guide activated B cells to inter- and outer-follicular regions and activated lymphocytes and DCs to the follicle/T-zone interface (Cyster et al., 2014; Li et al., 2016; Lu et al.,

2017). Recent in situ hybridization (ISH) analysis in the spleen showed *Ch25h* was expressed by stromal cells at the outer margins of follicles, in IFRs and at the follicle/T-zone interface (Lu et al., 2017). Using RNAscope ISH on pLNs and mesenteric LNs (mLNs), we observed that *Ch25h* was also highly expressed by cells at the follicle/T-zone interface and in IFRs of these tissues (Fig. 3B, S4). The RNAscope analysis also revealed *Ch25h* expression adjacent to the SCS in accordance with MRC location and in ring-like structures in the T-zone (Fig. 3B, S4) most likely corresponding to HEVs (Lee et al., 2014). Ch25h^{+} Ccl19^{lo} TRCs likely help guide activated B cells, T cells and DCs to the follicle/T-zone interface and IFRs. *Ch25h* expression was only detected in 21.6% of Ccl19^{lo} TRCs (Table S5). This could reflect low expression of the enzyme, thus it failed to be detected in a majority of Ccl19^{lo} TRCs, or reflect actual heterogeneity among the Ccl19^{lo} TRCs. More work is required to distinguish these possibilities and understand the additional functional roles of Ch25h^{+} Ccl19^{lo} TRCs at the follicle/T-zone interface and in IFRs.

Cxcl9^{+} TRCs are located in the T-zone and IFRs

The Cxcl9^{+} TRC cluster did not immediately align to a known stromal subset as these cells expressed low *Ccl21* and *Cxcl13* and no perivascular markers (Fig. 2C). However, their expression of *Ccl19* suggested they could be a subset of TRCs (Table S3). They distinctly expressed *Cxcl9*, *Cxcl10* and several MHCII related genes, such as *H2-Aa* and *H2-DMa* (Fig. 2A, 4A, Table S6). CXCL9 and CXCL10 have been shown to attract CXCR3^{+} myeloid cells in LNs (Janatpour et al., 2001; Yoneyama et al., 2004). While this expression pattern could suggest macrophage or dendritic cell (DC) identity,

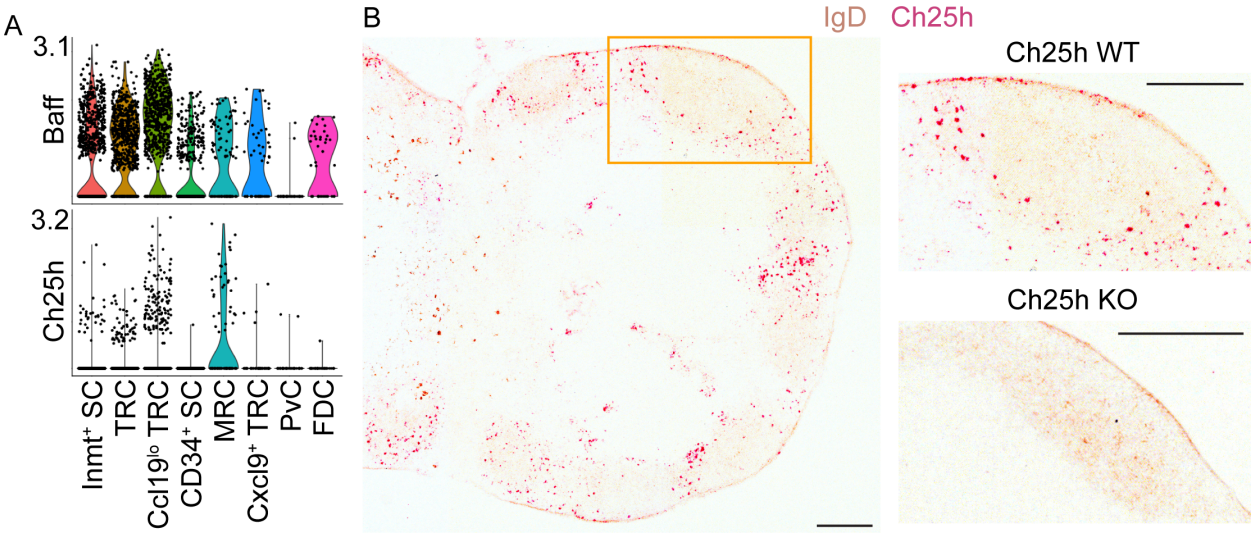

Figure 3. Ch25h-expressing Ccl19^{lo} TRCs are located at the follicle/T-zone interface and IFRs.
(A) Violin plot of *Baff (Tnfsf13b)* and *Ch25h* expression for each cell grouped by cluster. Highest log-normalized expression value is labeled on the y-axis. (B) RNAscope ISH for *Ch25h* (red) on *Ch25h* WT (box indicates enlarged area) and *Ch25h* KO pLN counterstained for IgD (brown). Representative of pLNs from 3 mice of each genotype. Scale bar is 200μm. See also Fig. S4.

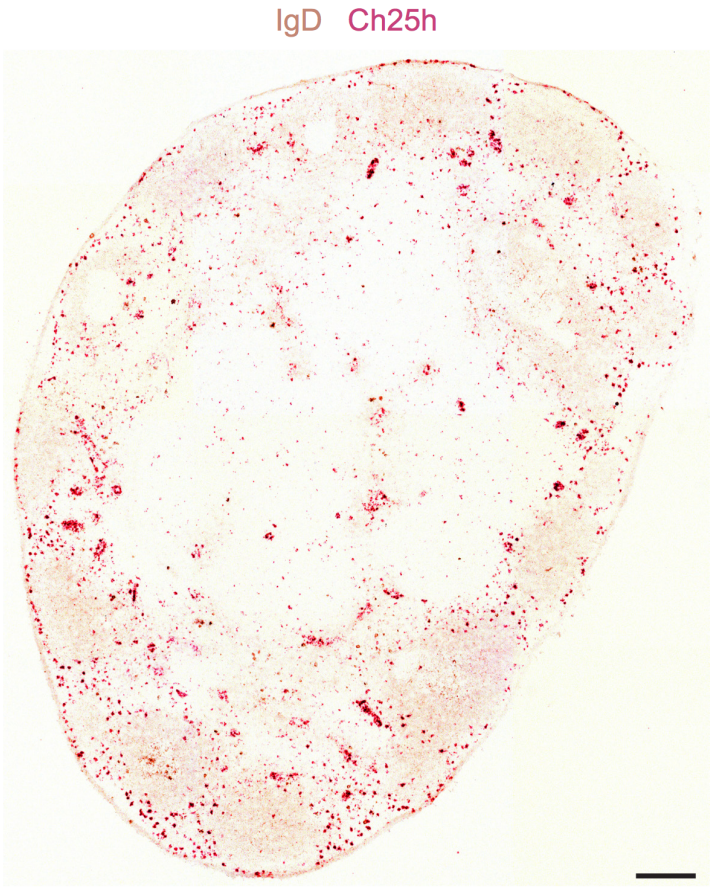

Figure S4. *Ch25h* expression in mLN. Related to Figure 3.
RNAscope ISH for *Ch25h* on C57BL/6 mLN with IgD counterstain (representative of 3 mice). Scale bar is 200μm.

this cluster also expressed the stromal marker *Pdgfr* ✔ (Mueller and Germain, 2009) (Fig. 2C) and expression of the classic macrophage or DC markers *CD11b*, *CD11c*, *F4/80*, *CD169*, *PU.1* or *Zbtb46* was not detected (Gray and Cyster, 2012b; Guilliams et al., 2016) (Table S3). Our finding is in accord with previous reports of *H2-DMa*, *Cxcl9* and *Cxcl10* mRNA and MHCII protein expression by FRCs (Dubrot et al., 2014; Malhotra et al., 2012).

To validate *Cxcl9* and *Cxcl10* expression on pLN stromal cells, we used flow cytometry to analyze classical pLN stromal subsets (FRCs, DNCs, LECs, BECs) from REX3 transgenic mice that express *Cxcl9*-RFP and *Cxcl10*-BFP reporters (Groom et al., 2012). We found portions of each classical subset that expressed both chemokines or CXCL10 alone (Fig. 4B). Looking specifically at the subsets we used for scRNA sequencing, we found 35.5% (SEM = 0.69%) of $CD45^{-}CD31^{-}$ stromal cells (FRC and DNC) expressed both CXCL9 and CXCL10 and 31.8% (SEM = 2.36%) expressed CXCL10 alone (Fig. 4B). These proportions were higher than the 11.8% of *Cxcl9* and *Cxcl10* expressing single cells and 28.1% of *Cxcl10* only expressing single cells in our dataset (Table S6). The $Cxcl9^{+}$ TRCs may be the cells expressing the highest CXCL9 and CXCL10 and the difference between the scRNAseq and reporter data may be a result of the low percent of mRNA capture per cell by the 10X Chromium system.

Consistent with these findings, popliteal LN (popLN) CXCL9 and CXCL10 expression by radio-resistant cells has been reported in sections in the T-zone, IFRs and medulla of REX3 reverse BM chimeras (Groom et al., 2012). Staining pLN sections from REX3 mice with PDGFRβ and CD11c to distinguish stromal cells from macrophages and DCs, we found $CXCL9^{+}$ $CXCL10^{+}$ $PDGFR\beta^{+}$ $CD11c^{-}$ stroma in the T-

zone and IFRs (Fig. 4C). We also found CXCL9$^-$ CXCL10$^+$ reticular stroma in the medullary cords (Fig. 4C). These are likely MedRCs that correspond to the *Cxcl10*-expressing Inmt$^+$ SCs discussed in more detail in a following section.

LN CXCL9 is induced by IFNγ in macrophages following immunization or infection and functions with CXCL10 to position activated Th1 cells, activated CD8 T cells, some types of DCs and memory T cells in IFRs (Groom et al., 2012; Kastenmuller et al., 2013; Kurachi et al., 2011; Sung et al., 2012). The Cxcl9$^+$ TRCs were highly enriched for interferon inducible *Gbp* genes and also expressed *Ifnar2*, *Ifngr1* and *Ifngr2*, though not exclusively (Fig. 2A, Table S6). In addition, while the Cxcl9$^+$ TRC expression profile was enriched for several MHCII genes (*H2-Aa*, *H2-Eb1* and *H2-Ab1*), the invariant chain (CD74) and peptide-loading chaperone (*H2-DMa*) we did not detect expression of co-stimulatory or inhibitory molecules (*CD80*, *Icosl*, *Pd-L1*, *4-1bbl*, *CD40*, *Hvem*, *Gitrl*, *Light*, *Tim3*, *Tl1a*, *CD30L*, *Pd-1h*, *Csf1r*, *CD86*, *Pd-L2, Ctla4, Btla, Ox-40, CD70, CD48, Slamf1* or *Tim1*) suggesting Cxcl9$^+$ TRCs could be tolerogenic. This is in accord with previous work demonstrating that IFNγ and inflammation can induce FRC expression of Cxcl9 and MHCII, that FRC antigen presentation can suppress CD4$^+$ T cell proliferation and survival in vitro and that non-hematopoietic MHCII expression is required for maintenance of Tregs in LN transplants (Baptista et al., 2014; Brown and Turley, 2015; Fletcher et al., 2011).

Since a portion of cells in the TRC cluster also express some *Cxcl9*, *Cxcl10* and MHCII alleles and since CXCL9$^+$ CXCL10$^+$ stromal cells were found interspersed with CXCL9$^-$ CXCL10$^-$ stromal cells in the T-zone and IFRs, we suggest that the Cxcl9$^+$ TRCs are an activated subset of TRCs potentially responding to IFNγ We may not have

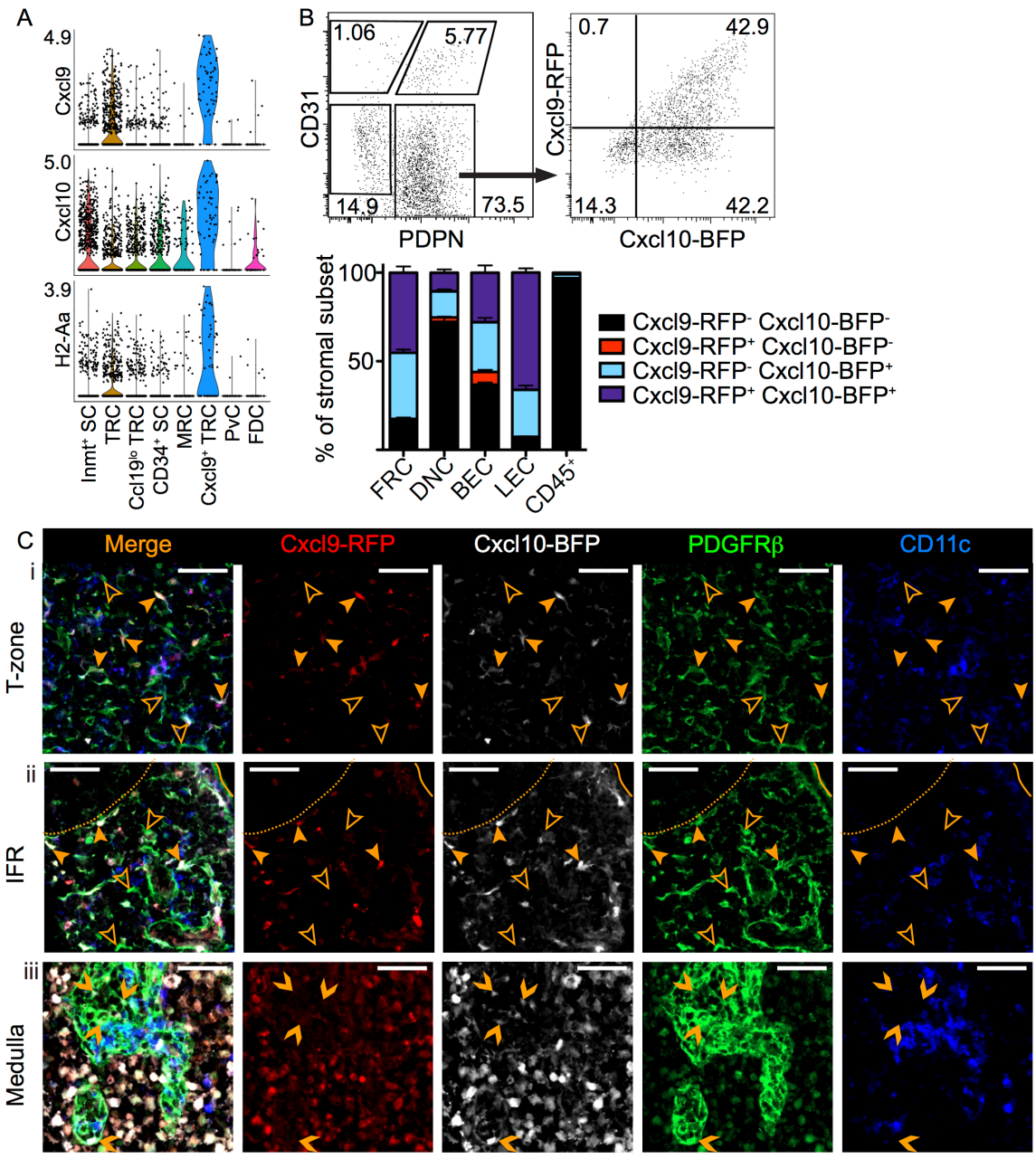

Figure 4. Cxcl9$^+$ TRCs populate the T-zone and IFRs
(A) Violin plots of *Cxcl9*, *Cxcl10* and *H2-Aa* expression for each cell grouped by cluster. (B) Flow cytometry of CD45$^-$ pLN classical stromal subsets from REX3 reporter mice for *Cxcl9*-RFP *Cxcl10*-BFP expression (top). Percentage of FRC, DNC, BEC and LEC stromal cells expressing *Cxcl9*-RFP and/or *Cxcl10*-BFP (bottom) (3 mice). Data represents mean and error bar indicates SEM. (C) IF microscopy of a REX3 pLN stained for PDGFRβ$^+$ CD11c$^-$ stromal cells in the (i) T-zone, (ii) IFR and (iii) medulla shown with the individual channels indicated (representative of 3 mice). Examples of *Cxcl9*-RFP$^+$ *Cxcl10*-BFP$^+$ PDGFRβ$^+$ CD11c$^-$ stromal cells (filled arrowhead), *Cxcl9*-RFP$^-$ *Cxcl10*-BFP$^-$ PDGFRβ$^+$ CD11c$^-$ stromal cells (unfilled arrowhead) and *Cxcl9*-RFP$^-$ *Cxcl10*-BFP$^+$ PDGFRβ$^+$ CD11c$^-$ stromal cells (chevron) indicated. Scale bar is 50μm.

detected a strong TRC signature in the Cxcl9$^+$ TRC expression profile because the limited mRNA capture combined with the small cell number (56 cells) meant the profile was dominated by activation genes. In support of this hypothesis, *Cxcl9*, *Ccl21* and *IL7* expression was detected in the post-infection Cxcl9$^+$ TRCs, which included 8.8 times the number of Cxcl9$^+$ TRCs (496 cells) and thus increased detection of less abundant transcripts (Table S3). Further study is required to determine whether the Cxcl9+ TRC profile describes a stable subset or an IFNγ-induced state of TRC. Either way Cxcl9$^+$ TRCs may play a role in positioning CXCR3$^+$ IFNγ-expressing cells, tolerizing activated T cells and maintaining Tregs.

MRC gene expression suggests involvement in barrier defense

MRCs are situated at the base of the SCS, where lymph drains antigen from peripheral tissues. However, very little is understood about the role of MRCs in this niche. MRCs have been described as Pdpn$^+$ Tnfsf11$^+$ Madcam1$^+$ Vcam1$^+$ Icam1$^+$ Bst1$^+$ Relb$^+$ Cxcl13$^+$ LN stroma (Katakai, 2012; Katakai et al., 2004). We found a cluster that expresses almost all of these markers suggesting the constituent cells are MRCs (Fig. 2A, 2C, 5A, Table S3). This subset was unexpectedly not enriched for *Madcam1* expression. The basis for this discrepancy is unclear as MRCs have not previously been isolated for transcriptional analysis. MRCs may express *Madcam1* mRNA at low levels, which are undetectable by this scRNA method while more efficiently translating or maintaining the stability of the protein than the TRCs which have detectable expression in our dataset. Alternatively, *Tnfsf11* and *Madcam1* may be expressed by closely associated cells rather than both being expressed by MRCs as section staining would

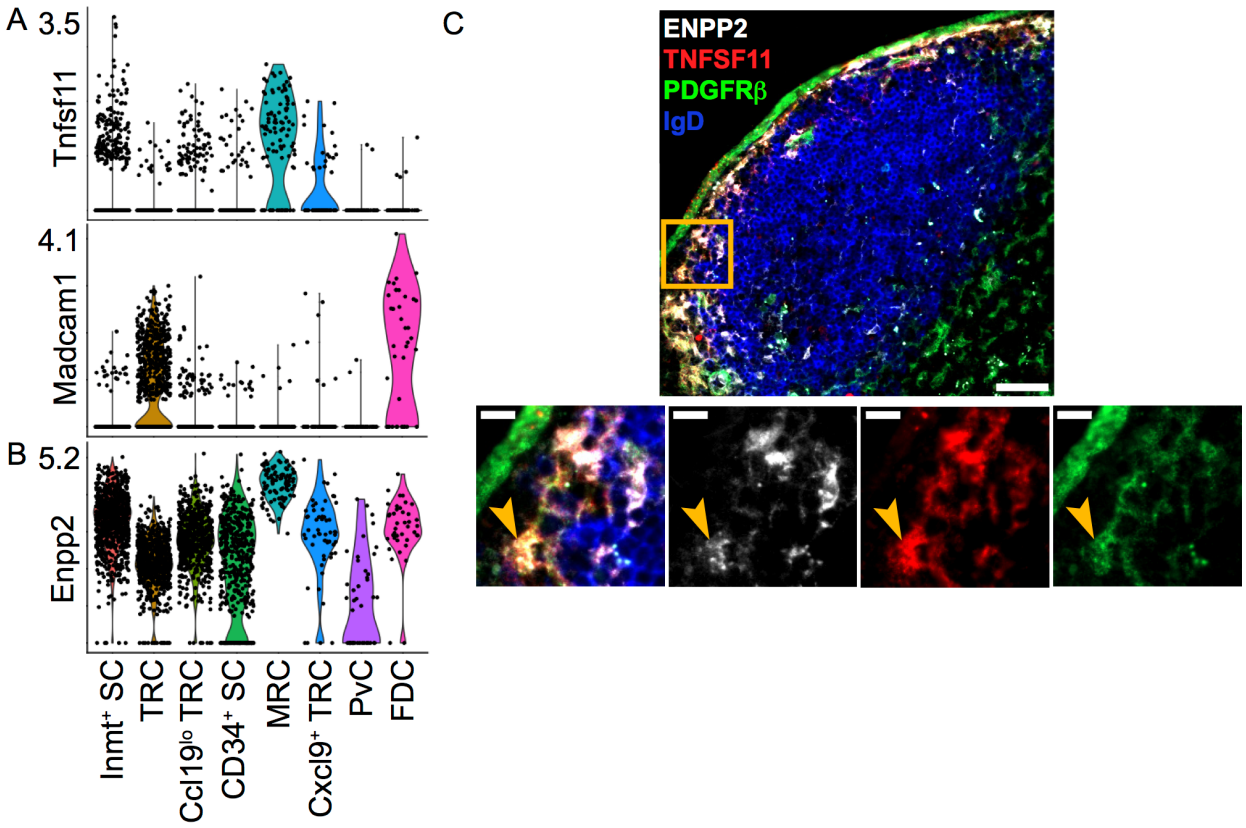

Figure 5. *Enpp2* expression by Tnfsf11^{+} MRCs in the SCS
(A) Violin plots of *Tnfsf11 (Trance)*, *Madcam1* and (B) *Enpp2* expression for each cell grouped by cluster. Highest log-normalized expression value is labeled on the y-axis. (C) Immunofluorescence (IF) microscopy of pLN SCS stained for ENPP2, TNFSF11, PDGFRβ and IgD (representative of pLNs from 3 mice). Scale bar is 50 μm. Box indicates magnified area shown in single channel images beneath. Arrowhead indicates example of ENPP2+ TNFSF11+ PDGFRβ+ MRC. Scale bar is 10μm.

suggest. In this regard it is notable that *Madcam1* expression is LTβR signaling dependent while *Tnfsf11* expression is not (van de Pavert and Mebius, 2010). The possibility that there is stromal cell heterogeneity in the SCS merits further study through high-resolution microscopy.

The SCS is a niche critical for antigen capture and possibly a barrier to pathogen spread. The most differentially expressed gene in MRCs was hepcidin antimicrobial peptide 2 (*Hamp2*) (Fig. 2A). Human hepcidin has been suggested to have anti-microbial activity in human bile (Strnad et al., 2011). In addition, MRCs were enriched for expression of *Enpp2* (autotaxin), a secreted enzyme required for the production of lysophosphatidic acid (LPA) (Katakai et al., 2014) (Fig. 5B). *Enpp2* expression by FRCs has been linked to T cell high-speed motility in the T-zone (Katakai and Kinashi, 2016; Katakai et al., 2014) and we speculate that it may also play a role in lymphocyte motility in the SCS. ENPP2 has been detected in the SCS (Katakai et al., 2014), consistent with MRC expression, and we found colocalization with staining for TNFSF11 on the follicle edge of the SCS (Fig. 5C). In pLN sections we also detected ENPP2 to a lesser extent in the T-zone and in HEVs in accord with the expression of *Enpp2* by several other stromal subsets in our dataset and with previous findings (Kanda et al., 2008; Katakai et al., 2014).

Several of the differentially expressed genes for this subset suggest MRCs could crosstalk with neuronal cells possibly influencing the initiation of the immune response. MRCs were enriched for *Ramp1* (Table S7), which functions together with *Calcrl* (also expressed in MRCs, Table S7) as a receptor for the neurotransmitter calcitonin gene-related peptide (CGRP) produced by both peripheral and central neurons (McLatchie et

al., 1998; Poyner, 1992). Sensory nerves containing CGRP are abundant in lymphoid organs, and nerve fibers have been reported in the LN SCS (Iannacone et al., 2010b). MRCs also expressed embigin (*Emb*) (Table S7), which has roles in nerve terminal sprouting (Lain et al., 2009) and differentially expressed stem cell factor (*Kitl*) (Table S7), a cytokine that is expressed by FAP^+ stromal cells in the BM and is required for hematopoiesis (Roberts et al., 2013). Kitl binds cKIT, which is expressed by DCs, BECs, lymphoid tissue inducers and neuronal precursors (Chappaz et al., 2010; Goldstein et al., 2014). This first transcriptional profile of MRCs suggests possible functions for these cells in the initial immune response and LN defense.

The expression profile of Itga7$^+$ PvCs suggests support of the endothelium and leukocyte entry into the LN

PvCs support the function of vessels as cellular conduits, aid the entry and exit of leukocytes from the LN and may even serve as progenitors for other lymphoid stroma (Chang and Turley, 2015; Krautler et al., 2012). Itga7$^+$ PvCs have been previously described as making up more than 50% of isolated DNCs (Malhotra et al., 2012) and are found around some HEVs and other vessels in the cortex and medulla. We were able to identify a particularly transcriptionally distinct stromal subset expressing the hallmarks of non-adventitial PvCs including *Pdgfr*β, *Cnn1*, *Acta2* (α*SMA*), *Itgb1*, *Esam1*, *Myl9*, *Mcam*, *Notch3* and *Actg2* (Chang and Turley, 2015; Malhotra et al., 2012) (Fig. 2A, S5, Table S8). The canonical PvC gene *NG2* was detected in only a few cells in the whole dataset likely reflecting low expression. Non-adventitial PvCs include

pericytes and vSMCs which have overlapping and dynamic marker expression and can only be

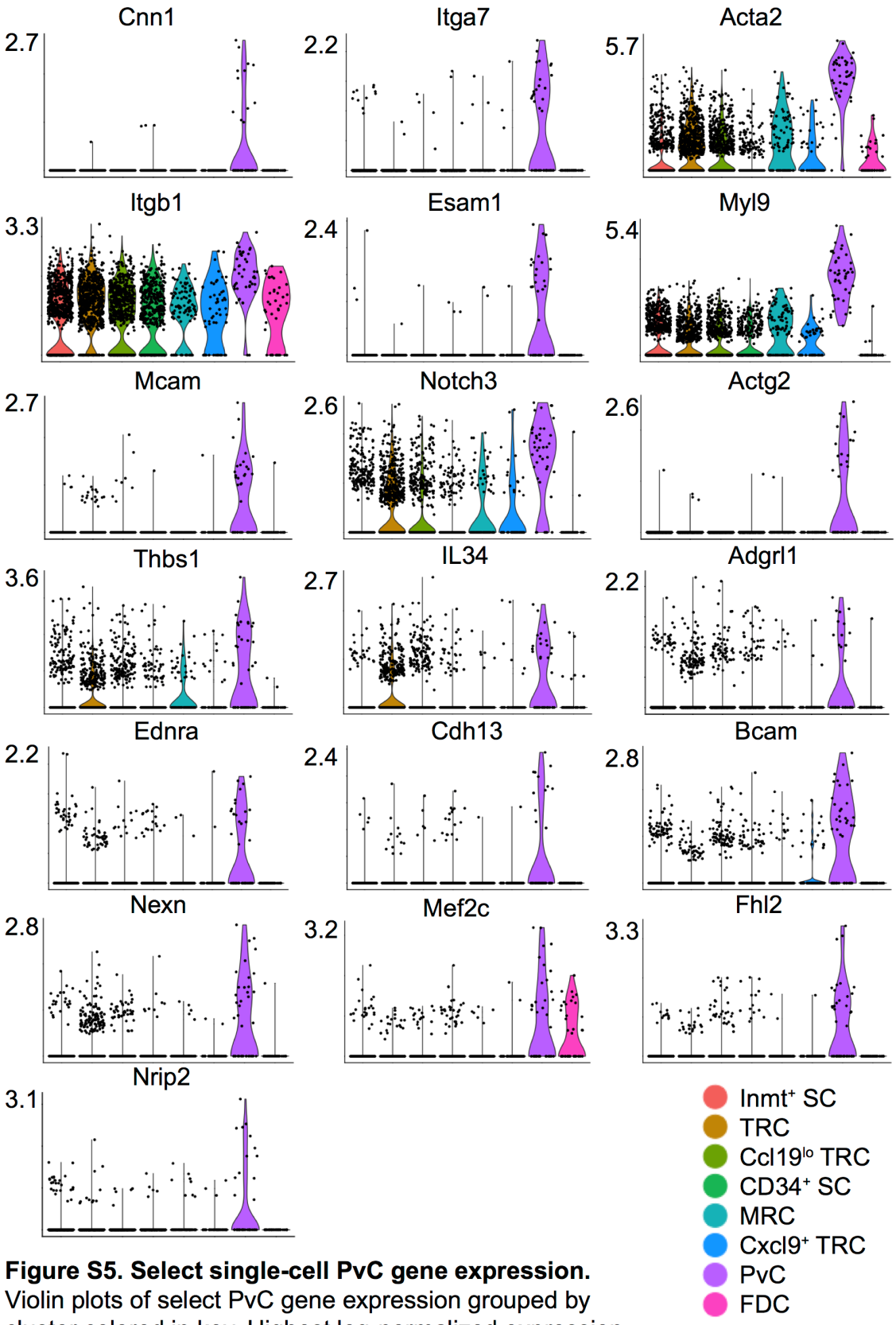

Figure S5. Select single-cell PvC gene expression. Violin plots of select PvC gene expression grouped by cluster colored in key. Highest log-normalized expression value is labeled on the y-axis for each gene.

distinguished in situ by their location surrounding capillaries and large vessels, respectively (Armulik et al., 2011). Our data did not detect a transcriptionally distinct Cnn1^{+} Itga7^{-} Pdpn^{-} subset previously proposed (Malhotra et al., 2012). This could be due to the transcript capture limit.

Since PvCs sit at the sites of lymphocyte entry to the LN, we looked for expression of genes that might facilitate lymphocyte movement or function and found PvCs were the most enriched for expression of thrombospondin (*Thbs1*), *IL34*, latrophilin-1 (*Adgrl1*) and endothelin-A receptor (*Ednra*), a gene involved in crosstalk between tissue cells and PvCs in kidneys (Kitazawa et al., 2011) (Fig. S5). PvCs also expressed cell junction factor cadherin 13 (*Cdh13*) and ECM-adhesion factors *Bcam* and *Nexn* (Fig. S5). PvCs were enriched for several transcription factors including *Mef2c*, *Fhl2* and *Nrip2* (Fig. S5). In summary, PvCs expressed a constellation of genes that may aid interactions at the vascular portals to the LN parenchyma.

CD34^{+} SCs express features of adventitial cells and are found in the pLN capsule and medulla

We identified a cluster of non-endothelial stromal cells distinguished by expression of the sialomucin *CD34* (Fig. 1D, 2A). Recent work characterized PDPN^{+} BST1^{-} Acta2^{-} CD34^{+} stromal cells surrounding large vessels in the LN medullary cords as adventitial cells based on shared gene expression with adventitial cells in other tissues (Corselli et al., 2012; Hindle et al., 2017; Sitnik et al., 2016). CD34 is also expressed by LN CD31^{+} BECs associated with HEVs and can bind L-selectin on passing lymphocytes (Baumhueter et al., 1993). The CD34^{+} SC cluster expressed *Pdpn*

on average, but had no detectable expression of *Bst1*, *Acta2* or *CD31*, in accord with these being adventitial cells (Table S3). Staining pLNs for $CD34^+$ $PDGFR\beta^+$ $BST1^-$cells we found expression in the LN capsule (Fig. 6A) and staining for $CD34^+$ $CD31^-$ cells, we found cells surrounding blood vessels in the medulla near the efferent lymphatics as well as in the pLN capsule (Fig. 6B).

The morphology of $CD34^+$ staining surrounding select medullary blood vessels is reminiscent of adventitial cells in other tissues (Corselli et al., 2012; Hindle et al., 2017; Sitnik et al., 2016). Adventitial cells in the LN have been described to support vessels and secrete vasculogenic and angiogenic factors (Sitnik et al., 2016). In our dataset, $CD34^+$ SCs expressed *Igf1*, *Igfbp3*, *Igfbp4*, *Vegfa*, *Vegfc* and exclusively *Igfbp6* (Fig. 2A, Table S3). In addition, the $CD34^+$ SCs were enriched for expression of growth factors and ECM factors.

Our initial clustering of the uninfected non-endothelial stromal cells suggested an additional subsetting of $CD34^+$ SCs into two clusters distinguished by Desmin (Des) expression. Staining pLNs for CD34 and Desmin, we did not detect Desmin on the $CD34^+$ cells in the pLN capsule or the majority of $CD34^+$ cells around blood vessels (Fig. 6B). However, the outer edge of the adventitial $CD34^+$ cells in the medulla was marked by Desmin so it is possible that some of these cells are producing Desmin and depositing it on the neighboring ECM. Investigating the $CD34^+$ Des^+ SC subcluster further, we found these cells were particularly enriched for *Ptn*, *Postn* and *Tnfsf9* (4-1BBL) expression with respect to all the other stromal clusters as well as in a pairwise comparison to $CD34^+$ Des^- SCs (Fig. 6C, Table S9). However, most of the other distinguishing genes for the $CD34^+$ SCs were just expressed at lower levels in the Des^+

fraction. This similarity in expression profile is reflected in the high correlation of the $CD34^+$ subclusters in PCA space ($r = 0.82$, p-value = 1.1×10^{-6}, Pearson correlation) suggesting the two subclusters should be considered a single stromal subset at this resolution. These $CD34^+$ subclusters were not distinguished in the clustering of the post-infection stromal cells separately from the uninfected cells (unpublished observations).

$CD34^+$ SC positioning in the pLN capsule is in accord with a study of human LNs showing $CD34^+$ cells in the capsule as well as around large vessels (Díaz-Flores et al., 2014). $CD34^+$ SCs were enriched for endosialin (*CD248*) expression, which is reported to be expressed in the resting LN capsule and required for LN expansion after immunization (Lax et al., 2010) (Table S9). While LECs line the subcapsular lymphatics adjacent to the capsule (Ulvmar et al., 2014), LECs do not express *CD34* (Immgen.org) and expression of the LEC markers *Lyve1*, *Prox1* or *Ackr4* (Ulvmar et al., 2014) was not detected in $CD34^+$ SCs suggesting the $CD34^+$ cells we are staining are not LECs. $CD34^+$ cells may communicate with LECs as LECs highly express the secreted protein MMRN2, a ligand for CD248 (Immgen.org) (Khan et al., 2017).

In accordance with a capsular location, the $CD34^+$ SC expression profile was enriched for the ECM components collagen 5 (*Col5a3*), collagen 15 (*Col15a1*) and laminin (*Lama2*) as well as osteoglycin (*Ogn*), vitrin (*Vit*) and *Mmp2* (Table S9). They also expressed *Loxl1*, *Mfap5* and *Fbln1*, which are important for ECM assembly and were previously reported as expressed by FRCs and DNCs (Malhotra et al., 2012) (Table S9). This subset was uniquely enriched for the expression of the transcription factors *Peg3* and *Ar* (Table S9). These data suggest that $CD34^+$ SCs include capsular

fibroblasts and adventitial cells and are well situated, in location and gene expression, to support the pLN capsule and large vessels.

Inmt$^+$ SCs may include MedRCs and activated stroma

Based on the expression profile, the Inmt$^+$ cluster could not be readily assigned to a known stromal subset or specific niche. The cells expressed a wide range of *Cxcl13*, low *Ccl19* and a portion of the cells expressed *IL7* (Fig. 2C, S3). Instead, these cells differentially, but not uniquely, expressed indolethylamine n-methyltransferase (*Inmt*) and stanniocalcin-1 (*Stc1*) (Fig. 2A, 6D). Inmt is an enzyme that can catalyze the N-methylation of tryptamine and structurally related compounds (Mavlyutov et al., 2012). Inmt might, therefore, influence cell-cell communication. Stc1 is a LIM-domain protein that may have a role in heterchromatin stability (He et al., 2013).

To attempt to localize these stromal cells we used RNAscope ISH to detect *Inmt* expression in LNs. The ISH revealed *Inmt* expression in the pLN medullary cords, which are structured by a network of MedRCs and Desmin-containing ECM (Fig. 6E, S6). We found the same *Inmt* expression pattern in mLNs, where the medulla was identified by sequential staining for F4/80$^+$ medullary cord macrophages (Gray and Cyster, 2012b) (Fig. S6). The *Inmt* signal localization, density and pattern is suggestive of medullary reticular cells (MedRCs). In our dataset, *Inmt* was also expressed by a portion of CD34$^+$ cells, MRCs and Cxcl9$^+$ TRCs (Fig. 6D) but none of these cell types are found in the medulla with this frequency. B cells, medullary cord macrophages, memory T cells and plasma cells do populate the medullary cords (Andrian and Mempel, 2003; Gray and Cyster, 2012b). While IgD$^+$ B cells and memory T cells do not express *Inmt*, there is no

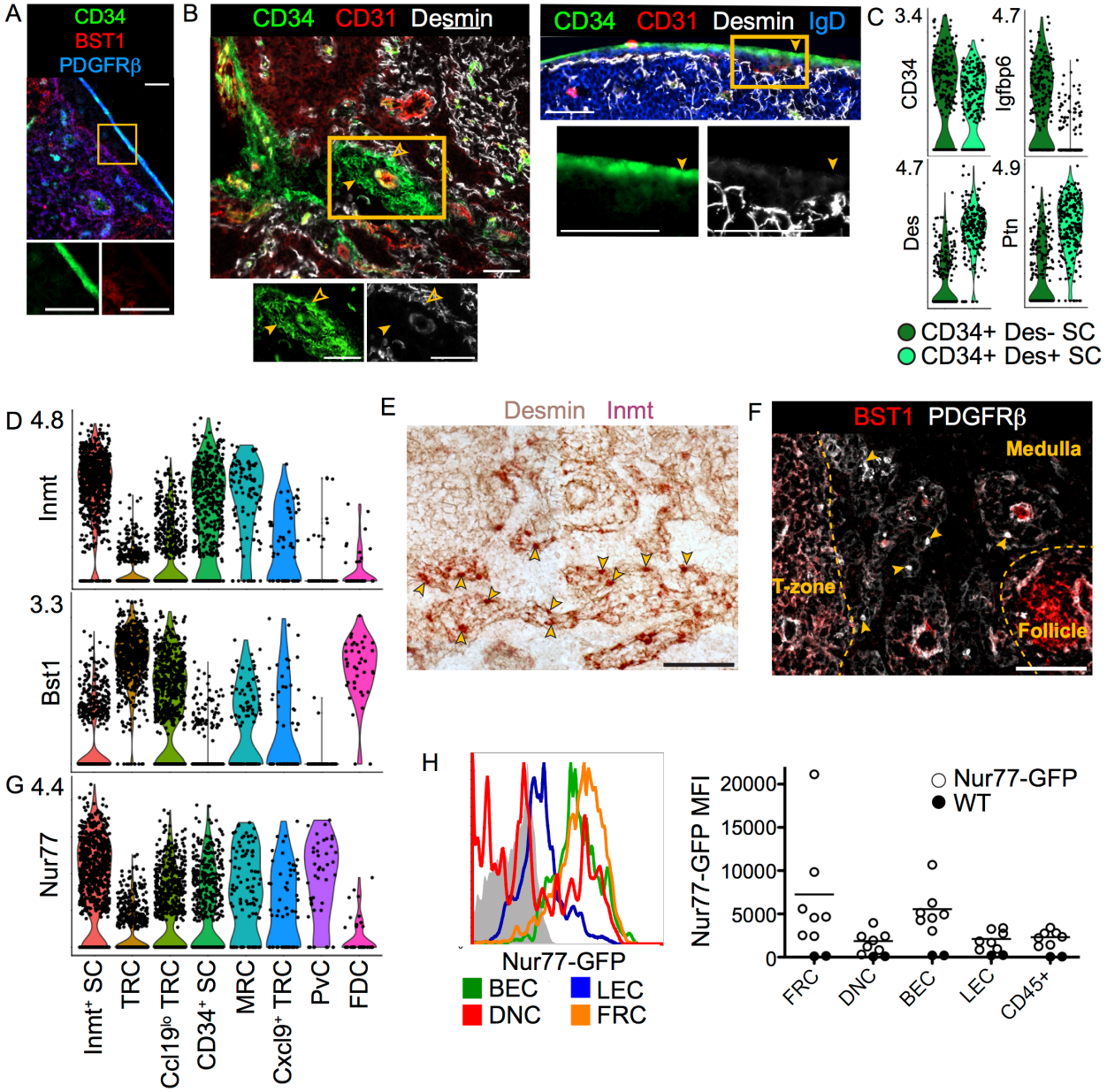
A
CD34
BST1
PDGFRβ
B
CD34 CD31 Desmin
CD34 CD31 Desmin IgD
C
3.4
4.7
CD34
Igfbp6
4.7
4.9
Des
Ptn
CD34+ Des- SC
CD34+ Des+ SC
D 4.8
Inmt
3.3
Bst1
G 4.4
Nur77
Inmt+ SC
TRC
Ccl19lo TRC
CD34+ SC
MRC
Cxcl9+ TRC
PvC
FDC
E
Desmin Inmt
F
BST1 PDGFRβ
Medulla
T-zone
Follicle
H
Nur77-GFP
BEC
LEC
DNC
FRC
Nur77-GFP MFI
20000
15000
10000
5000
0
Nur77-GFP
WT
FRC
DNC
BEC
LEC
CD45+
I
Medulla
IFR
Follicle/T-zone interface
T-zone
SCS
HEV
Nur77-GFP PDGFRβ IgD

Figure 6. Localization and characterization of CD34$^+$ SCs and Inmt+ SCs
(A) IF staining of pLN capsule for CD34$^+$ PDGFRβ$^+$ BST1$^-$ SCs. Box indicates enlarged area shown with individual channels below. Scale bars are 50μm. (B) IF staining of pLN medulla (left) and capsule (right) for CD34, CD31, Desmin and IgD (representative of 3 mice). Box indicates area shown in single channel images beneath. CD34$^+$ Des$^-$ staining (filled arrowhead) and CD34$^+$ Des$^+$ staining (unfilled arrowhead) indicated. (C) Violin plots of single-cell *CD34*, *Desmin* (*Des*), *Igfbp6* and *Ptn* expression grouped by subcluster of CD34$^+$ SCs with highest log-normalized expression value per gene indicated. (D) Violin plots for *Inmt* and *Bst1* expression for each cell grouped by cluster. (E) RNAscope ISH for *Inmt* with Desmin counterstain on pLN medullary cords (representative of 3 mice). Arrowheads indicate examples of Inmt$^+$ cells. See also Fig. S6. (F) IF staining for BST1 and PDGFRβ on pLN medullary cords (representative of 3 mice). Arrowheads indicate examples of BST1$^-$ PDGFRβ$^+$ MedRCs and yellow dotted lines demarcate the boundaries of the labeled niches. (G) Violin plot as in D for *Nr4a1* (*Nur77*) expression. (H) GFP MFI of CD45$^-$ pLN classical stromal subsets, FRCs, DNCs, BECs and LECs, and CD45$^+$ hematopoietic cells (CD45$^+$) from *Nur77*-GFP reporter mice detected by flow cytometry (n = 7, pooled from 3 experiments). (I) IF staining of indicated niches in *Nur77*-GFP pLNs for PDGFRβ$^+$ GFP$^+$ IgD$^-$ stromal cells (filled arrowheads). PDGFRβ$^+$ GFP$^-$ IgD$^-$ stromal cells also indicated (unfilled arrowheads) (representative of 2 mice). Scale bar is 50μm in B, E and F and 25μm in I.

expression data available for medullary macrophages (Immgen.org). Further analysis will be needed to determine whether medullary *Inmt* expression is restricted to stromal cells or also involves macrophages.

An additional distinguishing feature of the Inmt$^+$ stroma was low expression of *Bst1* relative to the FDC, MRC and TRC subsets (Fig. 6D). In sections, we found BST1 staining throughout the cortical stroma (FDCs, MRCs, TRCs, FSCs), but absent from the MedRCs in accord with previous work showing BST1$^-$ PDPN$^+$ cells in the medullary cords (Link et al., 2007)(Fig. 6F).

The Inmt$^+$ SCs differentially expressed many early response genes including *Nur77 (Nr4a1*), *Fosb*, *Fos*, *Junb*, *Egr1*, *Nfkbia* (*Ikba*), *Nfkbiz* and *Zfp36* (Ullman et al., 1990; Zikherman et al., 2012) (Fig. 6G, Table S10). Several of the other stromal subsets also highly expressed early response genes, but they did not reach differential significance for these subsets (Table S3). Early response genes can be activated by TLR, cytokine or growth factor signaling as well as physical stimuli (Ullman et al., 1990). To test whether a portion of the pLN stroma is activated in uninfected pLNs, we isolated pLN stroma from *Nur77*-GFP reporter mice, which express GFP with transcription of *Nur77* (Zikherman et al., 2012). We found that a portion of all the classic CD45$^-$ stromal subsets (BECs, LECs, FRCs and DNCs) expressed *Nur77*-GFP greater than the GFP$^-$ control with FRCs and BECs having the highest *Nur77*-GFP expression (Fig. 6H). Using PDGFRβ to identify stromal cells in sections, we found PDGFRβ$^+$ *Nur77*-GFP$^+$ cells frequently in the medulla and occasionally in IFRs, the follicle/T-zone interface, the T-zone, the SCS, and HEVs (Fig. 6I). These cells likely correspond to Inmt$^+$ SCs, TRC subsets, MRCs and BECs. The fine dendritic processes of FDCs prevented distinction

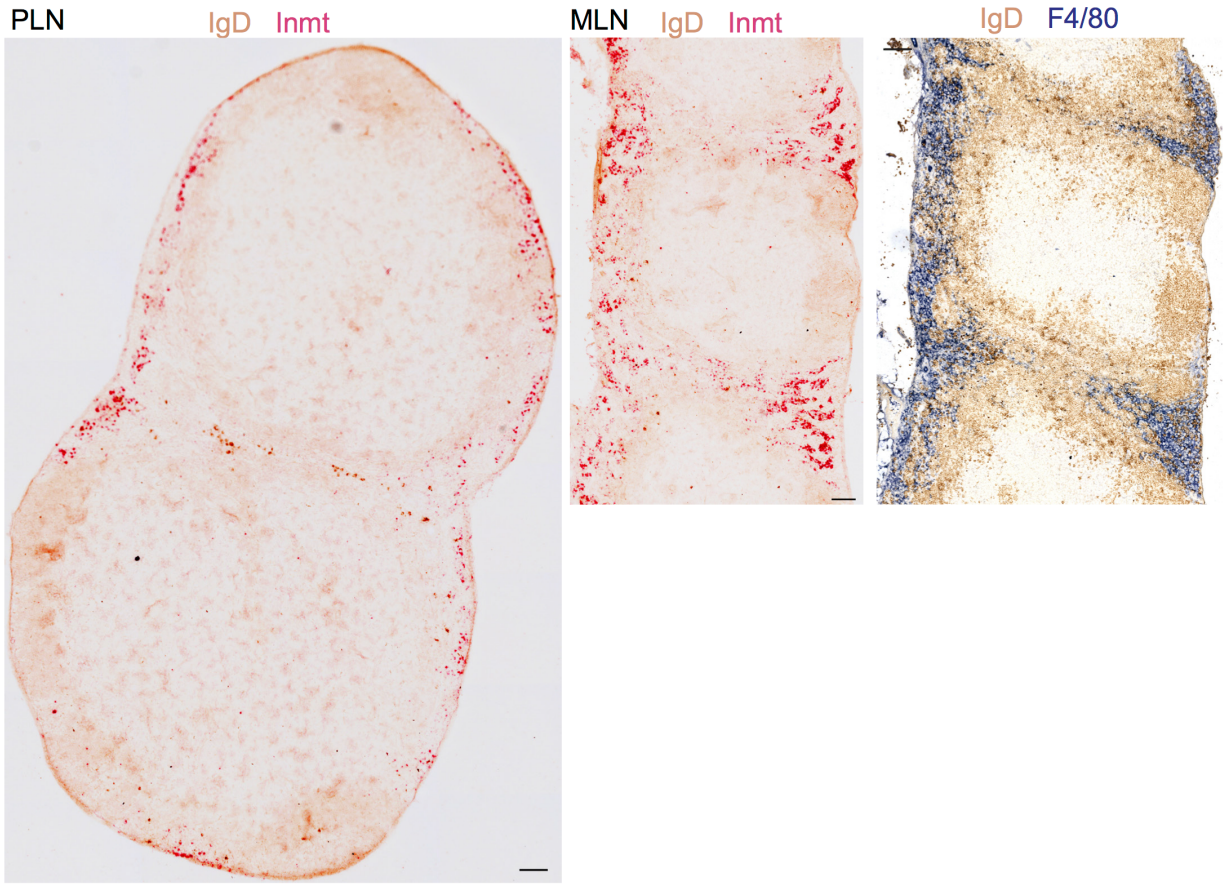

Figure S6. Medullary *Inmt* expression in LNs. Related to Figure 6.
RNAscope ISH for *Inmt* on pLN (left) and mLN (middle) with IgD counterstain. Sequential stain for F4/80 and IgD on mLN (right). Scale bar is 100μm.

of *Nur77*-GFP$^+$ stroma and lymphocytes in the follicle. The Inmt$^+$ SCs likely include MedRCs and represent particularly activated stroma. Whether MedRCs are responding more readily or frequently to environmental stimuli than stroma in other niches will require improved stromal phenotyping for flow cytometry and increased mRNA capture depth for scRNA sequencing.

Novel FDC gene expression of *Pthlh*, *Sox9* and *Tmem119*

LN FDCs are rare and the loss of FDC markers by digestion has previously made it difficult to isolate sufficient numbers of mouse pLN FDCs for transcriptional profiling. Single-cell RNA sequencing provided a unique solution. We identified a small cluster of stromal cells highly enriched for expression of well-defined FDC genes including complement receptor 2 (*Cr2*, *CD21/35*), Fc receptors (*Fcγr2b* and *Fcεr2a*), *Coch* (Py et al., 2013), *Prnp* (McCulloch et al., 2011; Prinz et al., 2002), *Tnfrsf9* (*4-1BB*) (Pauly et al., 2002) and *Vcam1* (Fig 2A, Table S11). The FDC cluster also highly expressed *Cxcl13* and the PS-binding *Mfge8* as has been well established in sections (Allen and Cyster, 2008)(Fig. 2C, Table S11). Matching published estimates for FDCs, the FDC cluster made up 1.5% of the recovered uninfected, pLN non-endothelial stromal cells (Jarjour et al., 2014) (Fig. 1B). FDCs were the most transcriptionally distinct subset, possibly reflecting their unique dendritic morphology and specialized function in antigen presentation (Heesters et al., 2014) (Fig. 2B).

In an effort to identify novel, FDC-specific factors that have a role in FDC-lymphocyte interactions or in FDC development we examined the expression of differentially expressed surface proteins, secreted proteins and transcription factors.

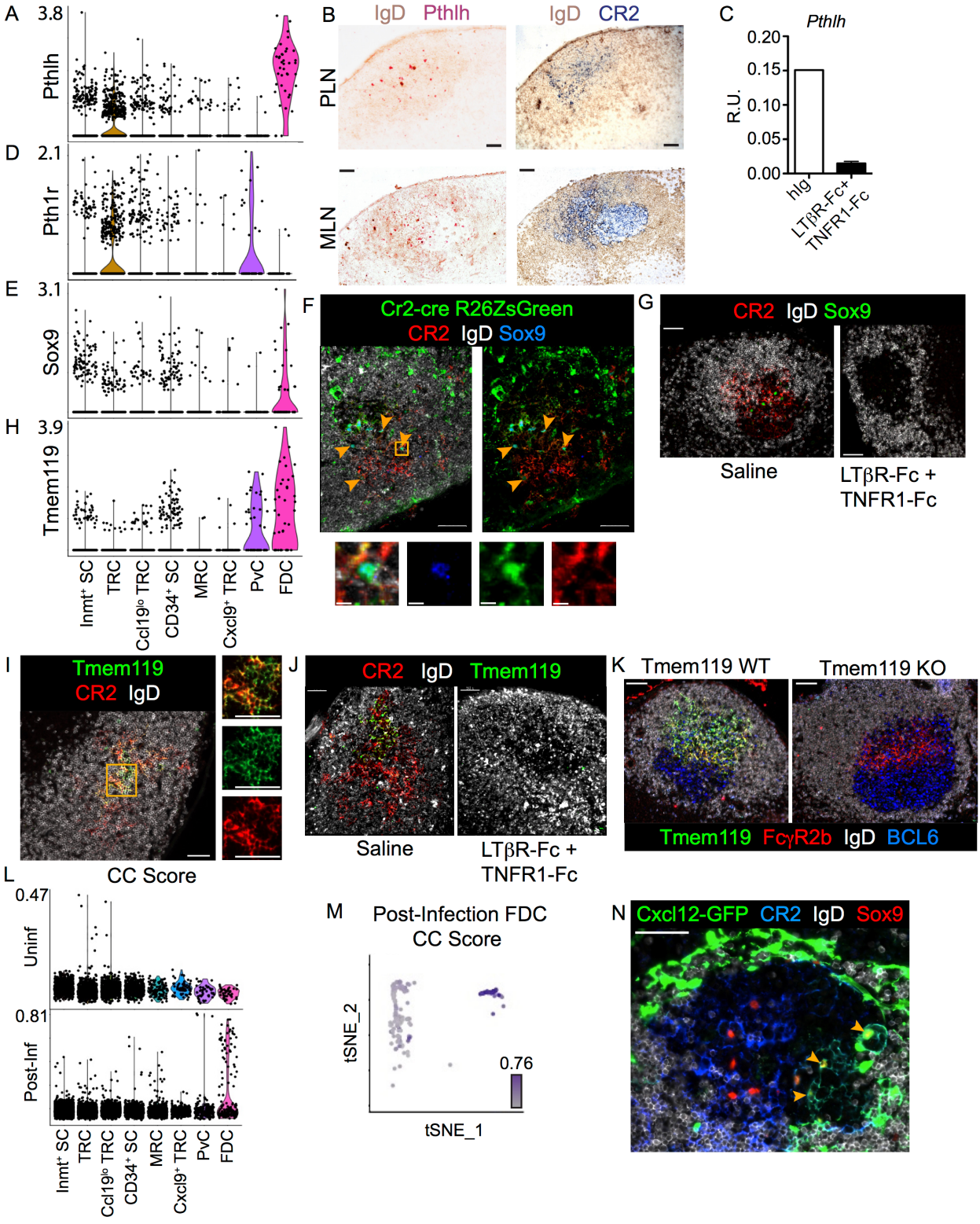
A
3.8
Pthlh
D
2.1
Pth1r
E
3.1
Sox9
H
3.9
Tmem119
Inmt+ SC
TRC
Ccl19lo TRC
CD34+ SC
MRC
Cxcl9+ TRC
PvC
FDC
B
IgD Pthlh
IgD CR2
PLN
MLN
C
Pthlh
R.U.
0.20
0.15
0.10
0.05
0.00
hlg
LTβR-Fc+ TNFR1-Fc
F
Cr2-cre R26ZsGreen
CR2 IgD Sox9
G
CR2 IgD Sox9
Saline
LTβR-Fc + TNFR1-Fc
I
Tmem119
CR2 IgD
CC Score
J
CR2 IgD Tmem119
Saline
LTβR-Fc + TNFR1-Fc
K
Tmem119 WT
Tmem119 KO
Tmem119 FcγR2b IgD BCL6
L
0.47
Uninf
0.81
Post-Inf
Inmt+ SC
TRC
Ccl19lo TRC
CD34+ SC
MRC
Cxcl9+ TRC
PvC
FDC
M
Post-Infection FDC CC Score
tSNE_2
tSNE_1
0.76
N
Cxcl12-GFP CR2 IgD Sox9

Figure 7. Novel FDC expression of *Pthlh*, *Sox9* and *Tmem119* and heterogeneity in post-infection FDCs

(A) Violin plot of *Pthlh* expression grouped by cluster and with highest log-normalized expression value labeled. (B) RNAscope ISH for *Pthlh* with IgD counterstain on pLN primary follicle and mLN secondary follicle and GC. Sequential stains for $CR2^+$ FDCs and IgD (representative of 2 mice). (C) QPCR of *Pthlh* expression in pLNs from mice treated on day 0 with LTβR-Fc and TNFR1-Fc (n = 1) and analyzed on day 3 or treated on day 0 and day 4 with LTβR-Fc and TNFR1-Fc (n = 1) or human IgG (hIg) (n = 1) and analyzed day 7. Data are pooled and plotted in relative units (R.U.). (D, E) Violin plots of *Pth1r* (D) and *Sox9* (E) expression as in A. (F) IF microscopy of pLN follicle from *Cr2*-cre *R26*-ZsGreen reverse BM chimeric mouse (representative of 2 mice). Arrowheads indicate examples of $CR2^+$ $ZsGreen^+$ $Sox9^+$ FDCs. Box indicates enlarged area shown with individual channels below, scale bar is 10μm. (G) IF microscopy of pLN GC from mice immunized with SRBC and on day 10 treated with LTβR-Fc and TNFR1-Fc or saline. PLNs were stained on day 4 post-treatment for $CR2^+$ FDCs and Sox9 (representative of 6 pLNs from 1 mouse per treatment). (H) Violin plot of *Tmem119* expression as in A. (I) IF microscopy of $Tmem119^+$ $CR2^+$ FDCs in a pLN primary follicle (representative of 2 mice). Box indicates enlarged area shown with individual channels on the right. (J) IF microscopy of pLN GC from a UBI-GFP reverse BM chimera immunized and treated as in G and stained for $CR2^+$ FDCs and Tmem119 (representative of 6 pLN from 1 mouse per treatment). (K) IF microscopy of a pLN GC (indicated by IgD^- $BCL6^+$ GCB cells) from Tmem119 WT (n = 4) and KO (n = 5) mice on day 11 post-immunization with NP-CGG stained for $Fc\gamma R2b^+$ FDCs and Tmem119 (representative of 2 mice per genotype). See also Fig. S7A. (L) Violin plot of the Cell Cycle Score (CC Score), a measurement of enrichment for cell cycle gene expression, of uninfected (Uninf) and post-infection (Post-Inf) stromal cells grouped by cluster with highest score labeled. (M) Post-infection FDCs colored by CC Score visualized with tSNE dimensionality reduction showing only the post-infection FDC subset. (N) IF microscopy of pLN GCs from a *Cxcl12*-GFP mouse immunized with SRBC and analyzed on day 10 (representative of 6 pLNs from 1 mouse per treatment). Arrowheads indicate *Cxcl12*-GFP^+ $Sox9^+$ CRCs. Scale bars in IF images are 50μm unless otherwise noted.

Parathyroid hormone like hormone (*Pthlh* or *Pthrp*) was highly differentially expressed by FDCs and is a secreted factor identified as an inducer of hypercalcemia of malignancy (Mundy and Edwards, 2008) (Fig. 7A). *Pthlh* has since been established to regulate bone resorption and to play a role in the differentiation of a number of other cell types (McCauley and Martin, 2012). RNAscope ISH analysis revealed *Pthlh* expression in the center of pLN primary follicles and in the light zones (LZ) of mLN GCs (Fig. 7B). The location and frequency of *Pthlh*-expressing cells suggest expression by FDCs and the presence of $CR2^{+}$ FDCs was confirmed in a sequential stain (Fig. 7B). Since FDCs depend on LT and TNF signaling (Fu and Chaplin, 1999; Lu and Browning, 2014; Ngo et al., 1999), we performed a 4 day blockade with LTβR-Fc and TNFR1-Fc to determine if *Pthlh* expression in pLNs depended on maintenance of FDCs (Lu and Browning, 2014; Rodda et al., 2015). This treatment caused loss of *Pthlh* transcript from pLNs consistent with FDC expression of *Pthlh* (Fig. 7C).

Pthlh is thought to largely act through *Pth1r*, though some receptor independent actions have also been proposed (Vilardaga et al., 2010). *Pth1r* is minimally expressed in hematopoietic cells, but it was detectable in bulk FRCs (Immgen.org). Using our dataset, we found expression specifically in TRCs and PvCs (Fig. 7D). Given the range of functions that have been attributed to *Pthlh* (Kir et al., 2014; McCauley and Martin, 2012), it will be of interest to determine whether FDCs or surrounding stromal cells are dependent on this factor for their development or organization.

FDCs also differentially expressed the transcription factor *Sox9* (Fig. 7E), which has roles in the differentiation of multiple cell types including chondrocytes, neural crest cells, melanocytes, various epithelial cells and endocardial endothelial cells that help

form cardiac valves (Akiyama et al., 2004; Huang et al., 2015). To assess FDC expression of *Sox9* we stained sections from a reverse chimeric *Cr2*-cre *R26*-ZsGreen reporter mouse where only radio-resistant *Cr2*-expressing (FDCs) and *Cr2*-lineage expressing cells express ZsGreen (Mionnet et al., 2013; Rodda et al., 2015). In pLN follicles, we found Sox9 co-stained ZsGreen$^+$ cell bodies of CR2$^+$ FDCs (Fig. 7F). We also observed Sox9 staining amid GC LZ CR2$^+$ FDC networks in pLNs from SRBC-immunized mice (Fig. 7G). Sox9 signal was lost along with CR2$^+$ FDCs after short-term LT and TNF signaling blockade consistent with FDCs expressing Sox9 (Fig. 7G). It will be important in future studies to determine whether Sox9 is necessary for FDC development.

Examination of the FDC subset for differentially expressed transmembrane protein-encoding genes revealed *Tmem119* (Fig. 7H). Tmem119 is an O-linked glycosylated surface protein that is a marker for microglia and osteoblasts and plays a role in osteoblast development (Bennett et al., 2016; Kanamoto et al., 2009; Mizuhashi et al., 2015). Staining with a Tmem119-specific monoclonal antibody (Bennett et al., 2016) revealed selective labeling of CR2$^+$ FDC networks in pLN primary follicles (Fig. 7I). Short-term blockade of LT and TNF signaling led to a loss of CR2$^+$ FDCs and Tmem119 staining in accord with FDC-specific expression of Tmem119 (Fig. 7J). To test for a role of Tmem119 in GC function, *Tmem119* wildtype (WT) and knockout (KO) mice (Bennett et al., 2016) were immunized with NP-CGG and analyzed after 11 days. While *Tmem119* KO pLN sections demonstrated loss of Tmem119 in FcγR2b$^+$ FDC networks in GC LZs, we saw no change in FDC morphology or GC polarization (Fig. 7K). Flow cytometric assessment found GCB cell, NP-specific GCB cell, follicular B

(FOB) cell, plasma cell and memory-phenotype B cell frequencies all within the normal range (Fig. S7A). These data indicate that Tmem119 is not essential for mounting GC responses. However, this transmembrane protein may be important in responses to specific types of antigen or in shaping specialized features of the response. Pthlh, Sox9 and Tmem119 are novel markers of FDCs that may contribute to the function of these distinctive stromal cells.

FDCs from virus-infected mice include cycling cells and a potential CRC subcluster

During an immune response GCs form at the center of follicles accompanied by the transition of primary follicle FDCs into GC LZ FDCs (Allen and Cyster, 2008). To study GC FDCs, we performed scRNA sequencing on pLN stroma on day 15 post-LCMV infection when the GCs are well-developed (Rodda et al., 2015). We first assessed whether any of the stromal subsets were enriched for a signature of cell cycle at this time-point. Calculating the Cell Cycle Score (CC Score) for each cell, which reports enrichment for a list of 96 canonical cell cycle genes (Tirosh et al., 2016), we found very few uninfected stromal cells (0% of uninfected FDCs and 0.334% of the other uninfected stromal subsets) or non-FDC post-infection stromal cells (0.513%) enriched for cell cycle gene expression. In contrast, 27.8% of FDCs from post-infection LNs were enriched for this cell cycle signature (Fig. 7L). FDC turnover has been challenging to study because FDCs are relatively rare (Fig. 1B), but our findings are in accord with increased EdU labeling of FDCs observed after immunization (Jarjour et al., 2014). The cell cycle signature in this subset of post-infection FDCs was so dominant

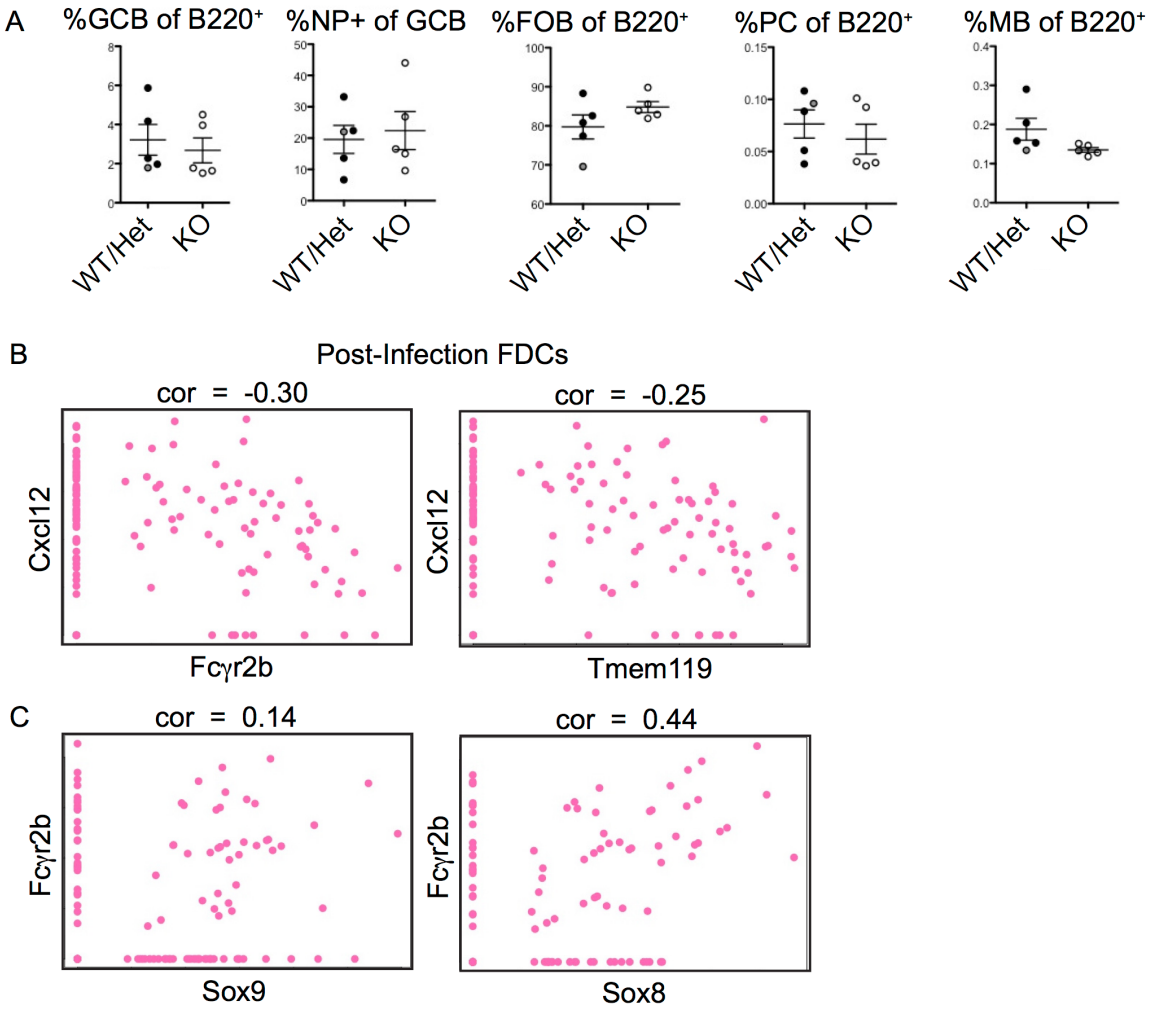

Figure S7. GC FDC requirements and heterogeneity. Related to Figure 7.
(A) Flow cytometric quantification of the percent of IgD- CD95+ GL7+ GC B cells (GCB), IgD- CD95+ GL7+ NP+ GC B cells (NP), IgD+ CD95- follicular B cells (FOB), CD138+ B220int plasma cells (PC) and IgD- CD38+ CD73+ CD95+ memory-phenotype B cells (MB) of B220+ pLN B cells from Tmem119 WT (n = 4, black circle), Het (n = 1, grey circle) and KO (n= 5, white circle) mice on day 11 post-immunization with NP-CGG in Sigma Adjuvant. Data represents mean and error bar indicates SEM. (B) Day 15 post-LCMV infection FDC expression of *Fcγr2b* ($p = 0.00038$) or *Tmem119* ($p = 0.00044$) vs. *Cxcl12* and (C) Sox9 ($p = 0.1029$) or Sox8 ($p = 1.195 \times 10^{-7}$) vs. *Fcγr2b* with Pearson correlation (cor) noted. Cycling FDCs have been removed from the FDC subset presented in Fig. 7M.

that the cells clustered distinctly from the rest of the FDCs (Fig. 7M) and were removed from the conservation analysis between the uninfected and post-infection stromal cells as the cell cycle signature was not conserved in the uninfected dataset (Fig. S1C).

Comparing the remaining aligned uninfected and post-infection FDCs we found 43 DEGs (absolute value of log2-fold change >1, FDR < 0.05, percent in cluster expressing > 10%) that were distinct from DEGs between the non-FDC uninfected and post-infection subsets (Table S12). While in section protein staining for canonical FDC genes, such as *Fcer2a* or *Vcam1*, is higher on GC LZ FDCs compared to primary follicle FDCs (Allen and Cyster, 2008), we did not see differential expression of these genes. This may reflect the technical challenges of isolating these delicate cells or suggest that the upregulation of these proteins on the surface of FDCs is post-transcriptionally regulated.

GCs were recently shown to contain $Cxcl12^{hi}$ $Cr2^{lo}$ DZ CRCs which have a morphology similar to FDCs relative to other LN stroma (Bannard et al., 2013; Rodda et al., 2015). By producing CXCL12, these cells help guide $CXCR4^{+}$ GCB cells to the DZ. However, the lack of specific markers for DZ CRCs has precluded their isolation and functional analysis. In addition, based on whole-mount imaging, DZ CRCs are expected to be even more rare than LZ FDCs (Rodda et al., 2015).

Since CRCs might be grouped with FDCs in our expression analysis based on their similar morphology, we investigated possible transcriptional heterogeneity among post-infection FDCs. Attempting to use unbiased subclustering of the non-cycling, post-infection FDCs, we did not find subclusters passing our significance threshold (greater than 20 DEGs compared to the other subclusters and compared to all other cells in the

dataset) possibly due to only having 133 cells in the analysis. However, we did see negatively correlated expression of canonical FDCs genes *Fcγr2b* and *Tmem119*, with *Cxcl12* (Fig. S7B). In contrast, there was no correlation of *Fcγr2b* with expression of *Sox9* (Fig. S7C). We examined Sox9 expression in sections of pLNs from immunized *Cxcl12*-GFP reporter mice to see if we could identify Cxcl12^{hi} Sox9^{+} stromal cells distinct from LZ FDCs. Indeed, we found Sox9 expression in CR2^{lo} *Cxcl12*-GFP^{hi} DZ CRCs as well as the expected expression in CR2^{hi} *Cxcl12*-GFP^{lo} LZ FDCs (Fig. 7N). We also observed some CR2^{lo} *Cxcl12*-GFP^{hi} Sox9^{+} cells in the follicle on the sides of the GC, but did not detect Cxcl12-GFP expression between the SCS and GC where the proposed MRC-derived CR2^{lo} pre-FDCs are positioned (Jarjour et al., 2014).

We found expression of the transcription factor *Sox8*, a binding partner of Sox9 (Huang et al., 2015), was positively correlated with expression of the LZ FDC marker, *Fcγr2b* (Fig. S7C). Since LZ FDCs and DZ CRCs occupy distinct niches and have unique functions suggesting different transcriptional programs, the combination of transcription factors may contribute to the unique expression program of LZ FDCs relative to DZ CRCs. While analysis of this heterogeneity revealed novel DZ CRC expression of *Sox9*, more cells or increased depth of mRNA capture would be required to determine if the heterogeneity in the post-infection FDCs reflects the inclusion of transcriptionally similar DZ CRCs or mRNA sampling variability.

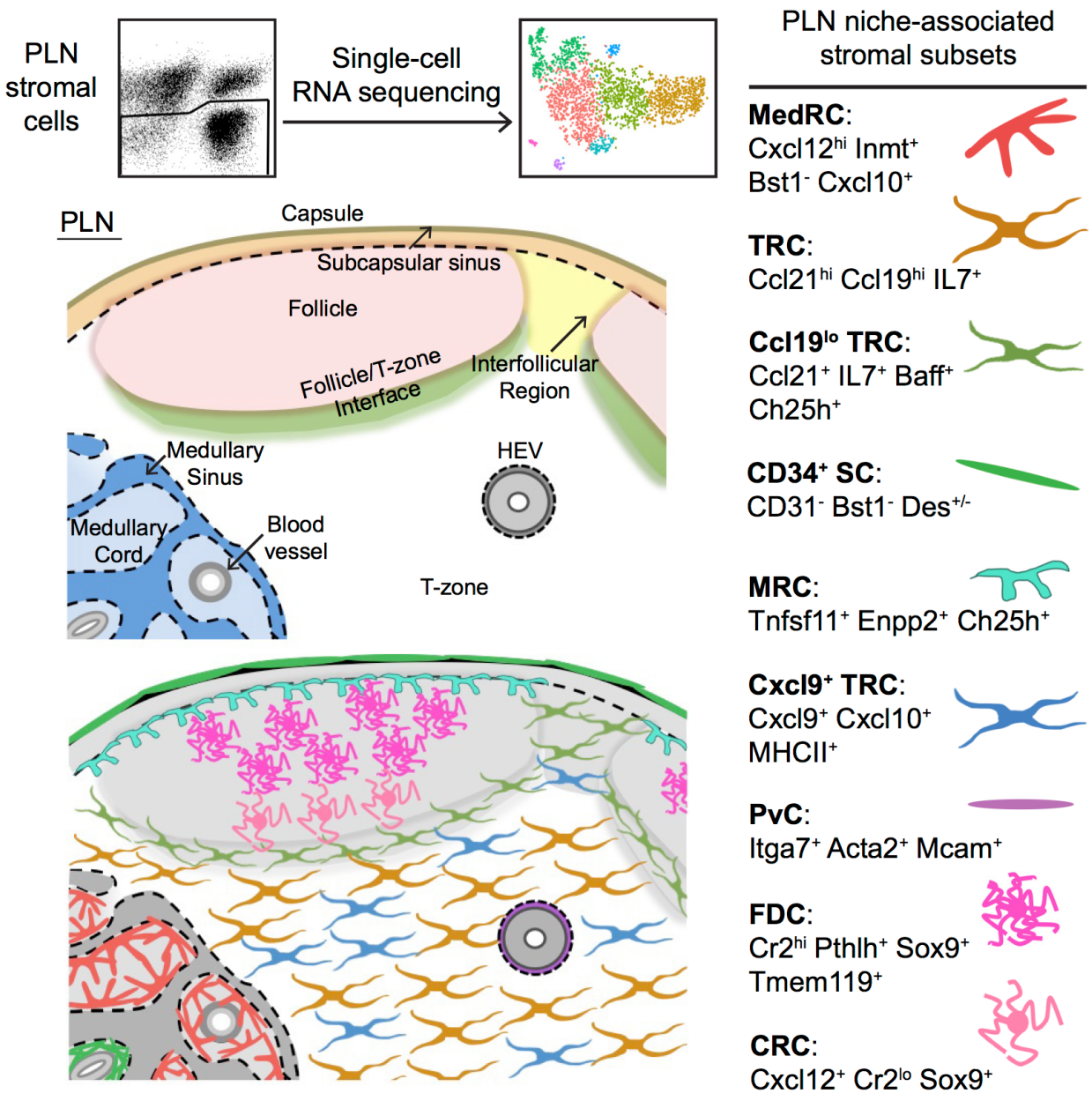

Figure S8. Summary of pLN, non-endothelial stromal subsets and their niche locations.

Discussion

Here we used scRNA sequencing to identify 8 pLN, non-endothelial stromal cell subsets. While we expect proportional composition will vary somewhat with different digestion protocols, we found these subsets conserved between two datasets. We established expression profiles for 4 subsets with known niche-localization: Ccl19^{hi} TRCs (T-zone), MRCs (SCS), FDCs (follicle center) and PvCs (perivascular). We identified novel expression of surface proteins, secreted factors and transcription factors for these subsets and validated several of these markers in situ. We used the expression profiles of the remaining subsets to associate them with pLN niches; Ch25h^{+} Ccl19^{lo} TRCs were found in the follicle/T-zone interface and IFRs, Cxcl9^{+} TRCs were found in the T-zone and IFRs, CD34^{+} SCs were found in the capsule and adventitial to select medullary vessels and Inmt^{+} SCs were found in the medullary cords. While the stromal subsets are not equally transcriptionally distinct, 7 of the 8 subsets were associated with a distinct anatomical location making this resolution of non-endothelial stromal heterogeneity useful for studying niche-specific functions. The Cxcl9^{+} TRCs are likely distinguished by a transient activation program, but nonetheless provide novel resolution of a potential function of TRCs and their characterization is likely to enrich our understanding of the LN T zone.

The introduction of additional subsets of pLN stroma allows more precise study of proposed niche-specific functions. FRCs have been suggested to induce CD8^{+} T cell and CD4^{+} T cell tolerance through presentation of peptide in MHCI or MHCII (Baptista et al., 2014; Brown and Turley, 2015; Fletcher et al., 2011). We found the expression of MHCII genes to be enriched in Cxcl9^{+} TRCs. It will be of interest in future studies to

determine whether the Cxcl9^{+} TRC subset which had no detectable expression of known co-stimulatory molecules or inhibitory molecules may be a subset particularly poised to promote T cell tolerance and how stably this transcriptional program is maintained. The Inmt^{+} SC subset highlighted the early response gene activation signature of stroma and one of these genes, *Nur77*, was expressed in stroma across niches including MedRCs. Many potential inputs could induce an early response gene signature and stromal cells likely need to be constantly probing and reacting to their environment to support the lymphocyte search for antigen and lymphocyte activation. The medulla is a site of high lymph flow and macrophage-mediated clearance of antigens and it seems likely that MedRCs are particularly exposed to lymph-borne materials. Whether the Inmt^{+} SCs have a role in sensing early signals and initiating LN activation will require future study.

Single-cell RNA sequencing of pLN, non-endothelial stromal cells has provided a unique opportunity to study rare stromal cell types that have been challenging to isolate. While there have been several published FDC transcriptome efforts in the past they have suffered from either B cell, myeloid cell or FRC contamination or required additional manipulation, such as irradiation of the mice or *in vitro* culture (Heesters et al., 2013; Suzuki et al., 2010; Wilke et al., 2010). Our expression profile of freshly isolated FDCs from uninfected mice revealed expression of *Pthlh*, *Sox9* and *Tmem119* as novel markers of FDCs. The human tissue atlas (Uhlén et al., 2015) (proteinatlas.org) showed staining for Sox9 and Tmem119 on tonsil and LN GCs LZs, supporting conserved expression of these genes by human FDCs. Further transcriptional heterogeneity of post-infection FDCs yielded a novel marker of the even

more rare DZ CRCs. Finally, analysis of the post-LCMV infection FDCs adds further evidence that FDCs undergo proliferation during GC responses (Jarjour et al., 2014) and suggest the importance of understanding how FDC turnover impacts on antigen persistence and the duration of GC responses.

Studying LN stromal contributions to individual niches has been challenged by the lack of distinguishing positive markers for stroma in each niche. MedRCs have no validated positive markers other than high expression of *Cxcl12*, a chemokine that has a critical role in attracting plasma cells into the medullary region, but is also expressed by other LN stroma (Allen et al., 2004; Bannard et al., 2013; Fooksman et al., 2010; Hargreaves et al., 2001). In situ analysis of *Inmt* transcript expression enabled us to identify MedRCs as Inmt^{+} and in situ analysis of REX3 mice distinguished MedRCs as CXCL10^{+} CXCL9-. While, we have not been able to find a specific marker for FSCs, CXCL13-expressing cells that surround FDCs in the follicle (Allen and Cyster, 2008), we speculate that FSCs are included in the portion of the Inmt^{+} SC cluster that is enriched for *Cxcl13* expression as this is not a reported feature of the medulla. Versatile stromal cells, non-FDC *Cr2*-lineage marked cells found in the follicle and T-zone (Mionnet et al., 2013) and lacking additional identifying markers, were also not resolved as a discrete cluster in our dataset. Improvements in percent of mRNA captured with scRNA sequencing technology and isolation efforts will likely aid in the ability to distinguish additional heterogeneity.

The lack of niche-specific stromal cell transcriptomes has impeded study of the lineage relationships between LN stromal cells. While the clustering of transcriptional profiles does not establish the same type of distinguishing feature for each cluster and

is insufficient to determine where clusters lie on the continuum from cell state to cell type, the clustering can direct new fate-mapping efforts to address the relationships between stromal subsets. These signatures can also be used as a source of markers to track the appearance of these stromal populations during embryogenesis and to follow changes in their distribution and number during immune responses. Moreover, they can be used to guide generation of new Cre recombinase and reporter mouse lines, perhaps involving combinatorial strategies that mark cells based on the intersection of two co-expressed genes.

Almost all of the stromal expression profiles we identified included unique transcription factors, which may help elucidate the developmental relationships between these stromal subsets. For example, *Sox9* is the first described transcription factor expressed specifically by FDCs and CRCs. *Sox9* is not detected in MRCs, a proposed LN FDC progenitor (Jarjour et al., 2014), in PvCs, a proposed splenic FDC progenitor (Aguzzi and Krautler, 2010) nor in $CD34^+$ SCs which have been shown to have progenitor potential (Sitnik et al., 2016). Whether *Sox9* expression is integral to FDC differentiation from any of the proposed progenitors requires further study. Since stromal cells cultured *in vitro* tend to lose their specific features, it may be that all stromal cells have a degree of plasticity. Studying these population-specific transcription factors could help explore fibroblast differentiation and improve *in vitro* efforts to investigate the functions of distinct stromal cell types.

These transcriptional profiles of pLN, non-endothelial stromal subsets can also provide a homeostatic template for comparison to stroma from other healthy and diseased tissues. Since similar niches exist in pLN and mucosal lymphoid tissues, such

as Peyer's patches, comparing the proportion of the non-endothelial stromal subsets and the transcriptional profiles between these tissues could help reveal how these tissues support distinct immune responses. Cancer-associated fibroblasts (CAFs) in tumors or non-endothelial stromal cells in inflamed tissues and tertiary lymphoid organs (TLOs) play significant roles in the pathology of these tissues (Barone et al., 2016; Mizoguchi et al., 2017; Stephenson et al., 2017; Turley et al., 2015). For example, TLOs have TRCs and FDC-like stroma creating B and T-zones, but how these might be distinguished from healthy pLN stroma and clinically targeted is unclear. Our high-resolution transcriptomic analysis of pLN, non-endothelial stroma is a resource for understanding the complex roles of heterogeneous stromal cells in the compartmentalized steps of the immune response.

Materials and Methods

Mice and chimeras

C57BL/6 (B6) and B6-CD45.1 mice were purchased from the National Cancer Institute at Charles River. *B6.Cg-Cxcl12*^{tm2Tng} (*Cxcl12*-GFP) gene-targeted mice were provided by T. Nagasawa (Ara et al., 2003b) and were backcrossed to the B6 background more than seven generations. *B6.Tg(Cr2-Cre)3Cgn* (*Cr2*-Cre) BAC-transgenic mice were fully backcrossed to B6 and provided by K. Rajewsky (Immune Disease Institute, Boston, MA) (Kraus et al., 2004). *B6.Cg-Gt(ROSA) 26Sor*$^{tm6(CAG-Zsgreen1)Hze/J}$ (*R26*-ZsGreen) mice have a CAG promoter, a floxed stop sequence, and ZsGreen1 knocked into the Gt(ROSA)26Sor locus and were purchased from The Jackson Laboratory. 129S5-Tmem119$^{<tm1Lex>/Mmcd}$ *(Tmem119* KO) mice were fully backcrossed to B6 and provided by B. Barres (Bennett et al., 2016). *Nr4a1*-EGFP BAC-transgenic (*Nur77*-GFP) mice (Zikherman et al., 2012) were backcrossed to B6 at least 6 generations and provided by J. Roose. *Ch25h* KO mice were fully backcrossed to C57BL/6 (Bauman et al., 2009). REX3-Tg, *Cxcl9*-RFP *Cxcl10*-BFP (REX3), transgenic mice were made on a B6 background (Groom et al., 2012). *Tg(UBC-GFP)30Scha/J* (UBI-GFP) transgenic mice were backcrossed to C57BL/6 for more than 8 generations and were from The Jackson Laboratory

Bone marrow (BM) chimeras were made as described previously and analyzed after at least 8 weeks (Bannard et al., 2013). UBI-GFP mice were treated intraperitoneally (ip) with 500μg anti-Thy1.2 (clone 30H12) to ablate radio-resistant T cells before being irradiated and reconstituted with wild-type CD45.1 BM. *Cr2*-Cre *R26*-ZsGreen mice were irradiated and reconstituted with WT CD45.1 BM.

Animals were housed in a specific pathogen–free environment in the Laboratory Animal Research Center at the University of California, San Francisco, and all experiments conformed to ethical principles and guidelines approved by the University of California, San Francisco, Institutional Animal Care and Use Committee.

Stromal Cell Preparation and Flow Cytometry

PLN stromal cells were prepared for scRNA sequencing from the inguinal, brachial and axillary LNs of 12 uninfected, adult, female C57BL/6 mice and 9 post-LCMV infected adult, female C57BL/6 mice. PLNs were harvested into DMEM (Fisher Scientific) with 2% FCS (HyClone), 10mM HEPES (Fisher Scientific) and Pen/Strep (P/S) (Fisher Scientific) on ice and minced with 25G needles (Fisher Scientific). Tissue was transferred to room temperature digestion buffer (DMEM + 2%FCS + HEPES + P/S + 3mg/ml Collagenase IV (Worthington Biochemical) and 40µg/ml DNase I (Sigma-Aldrich) and incubated at 37^{o}C in a beaker with water and a stirbar gently spinning for 15 min. Tissue was pipetted 50x with a Pasteur pipet and incubated another 15min before being pipetted 100x and filtered through a 100µm filter into MACS Buffer (PBS with 2% FCS and 2mM EDTA) on ice. The cell suspension was spun down and resuspended to 1x10^{7} cells/ml in MACS buffer with 10µl/4x10^{7}cells anti-CD45 MACS microbeads (Miltenyi) to rotate for 40min at 4^{o}C. After MACS depletion of CD45^{+} cells, the remaining suspension was stained with anti-CD45 PerCpCy5.5 (30-F11, Biolegend), anti-CD31 PE (MEC 13.3, BD Biosciences), anti-gp38 APC (8.1.1, Biolegend) and DAPI (Invitrogen) for flow cytometry assisted cell sorting for viable CD45^{-} CD31^{-} cells on a FACSAria Fusion into PBS + 0.04% BSA. Cells with the lowest DAPI staining were excluded as SSC-A^{lo} CD45^{-} CD31^{-} PDPN^{-} insufficiently stained CD45^{+} cells. Data was

analyzed using FlowJo (Treestar). PLN stromal cells from individual *Nur77*-GFP mice were processed using the same protocol and additionally stained with anti-CD45 Pacific Blue (104, Biolegend), anti-BP3 (BD Biosciences) conjugated to biotin and streptavidin PECy7 (Biolegend).

For the analysis of REX3 pLN stroma, whole LNs were placed on 70µm sterile filters and mechanically disrupted and subjected to digestion in DNase I (100µg/ml), Collagenase P (200µg/ml), Dispase II (800µg/ml), 1% FCS in RPMI. LNs were placed in the pre-warmed enzyme mixture and incubated at 37^{o}C. At 8 minute intervals, any supernatant was removed, added to RPMI/2mM EDTA/1% FCS, and replaced with fresh enzyme media. This was repeated at 8min intervals until no large tissue fragments remained. For flow cytometry on Rex3 pLN stroma, single-cell suspensions of 2x10^{6} cells underwent staining in PBS/0.5% FCS with anti-gp38 Alexa488 (Biolegend), anti-CD31 PECy7 (Biolegend), anti-CD45 BUV395 (BD Biosciences), anti-CD16/32 (Biolegend), and Fixable Viability Dye eFluor780 (eBioscience). Samples were run on BD Fortessa X20 and data was analyzed using FlowJo (TreeStar) and Prism (GraphPad).

Single-cell suspensions of B cells were generated and stained as previously described (Allen et al., 2007b). The following antibodies were used for cell staining: anti-B220 BV785 (RA3-6B2, Biolegend), anti-IgD BV650 and Pacific Blue (11-26c.2a, Biolegend), anti-Fas PE-Cy7 (Jo2, BD Biosciences/Fisher), anti-T- and B-Cell Activation Antigen Pacific Blue and APC (GL7, Biolegend), anti-NP PE (Biosearch Technologies), Fixable Viability Dye ef780 (eBioscience), anti-CD138 BV421 (281-2, Biolegend), anti-CD73 PerCpCy5.5 (TY/11.8, Biolegend) and anti-CD38 Alexa647 (90, Biolegend).

Samples were acquired and analyzed with a BD LSRII, Flowjo (Treestar) and Prism (GraphPad).

Droplet-based single-cell RNA sequencing

Immediately post-sorting, $DAPI^-$ $CD45^-$ $CD31^-$ pLN stromal cells were run on the 10X Chromium (10X Genomics) (Zheng et al., 2017) and then through library preparation by the Institute for Human Genetics at UCSF following the recommended protocol for the Chromium Single Cell 3' Reagent Kit (v2 Chemistry). Libraries were run on the HiSeq4000 for Illumina sequencing. Post-processing and quality control were performed by the Genomics Core Facility at the Institute for Human Genetics at UCSF using the 10X Cell Ranger package (10X Genomics). Primary assessment with this software for the uninfected sample reported 2,915 cell-barcodes with 5,542 median unique molecular identifiers (UMIs, transcripts) per cell and 2,148 median genes per cell sequenced to 87.8% sequencing saturation with 116,135 mean reads per cell. Primary assessment with this software for the LCMV-infected sample reported 12,713 cell-barcodes with 4,477 median unique transcripts per cell and 1,937 median genes per cell sequenced to 59.9% sequencing saturation with 26,050 mean reads per cell.

Infections, Immunizations and Treatments

Mice were infected with LCMV-Armstrong intravenously (iv) at $2.5x10^5$ pfu and analyzed on day 15 for scRNA sequencing and immunocytochemistry (Clingan and Matloubian, 2013).

Mice were immunized with 0.5mg/ml NP(25)-CGG (Biosearch Technologies) in

Sigma Adjuvant System (Sigma-Aldrich) and a total of 185µl/mouse subcutaneously (sc) at the shoulders, flanks and above the tail and analyzed on day 10 for flow cytometry and immunofluorescence.

For LTβR and TNFR1 signaling blockade, *Cxcl12*-GFP or UBI-GFP reverse chimeric mice were immunized sc at the shoulders, flanks and above the tail with SRBCs on day 0 and day 5 and on day 10 treated iv with 100µl each of 1mg/ml mLTβR-huIgG1 (LTβR-Fc, provided by J. Browning) and 1mg/ml TNFR55-huIgG1 (TNFR1-Fc, provided by J. Browning) or saline or human IgG1 (hIg). Draining pLNs (axillary, brachial and inguinal) were analyzed 4 days later. C57BL/6 mice were treated in the same way without immunization.

Immunocytochemistry

Tissues expressing GFP or ZsGreen were fixed in 4% PFA for 2 hours at 4^{o}C, washed and sunk in 30% sucrose before freezing in OCT. REX3 tissues were fixed in PLP and processed as previously described (Groom et al., 2012). All other tissues were directly frozen in OCT and slides were fixed in acetone. 7µm cryosections and 30µm sections were stained as described (Rodda et al., 2015) with primary antibodies: Rabbit anti-Tmem119 (produced and gifted by B. Barres) (Bennett et al., 2016), anti-ENPP2 (polyclonal, R&D Systems), anti-TNFSF11 (polyclonal, R&D Systems), anti-CD34 FITC (RAM34, BD Pharmingen), anti-CD31 biotin (MEC13.3, Biolegend), goat anti-IgD (polyclonal GAM/IGD(FC)/7S, Cedarlane Labs), goat anti-desmin (polyclonal, R&D Systems), anti-IgD Alexa647 (11-26c.2a, Biolegend), anti-BST1 (BP3, BD Biosciences) conjugated to Alexa647, rabbit anti-PDGFRβ (28E1, Cell Signaling), anti-CD11c

Alexa647 (Biolegend), Rabbit anti-Sox9 (Millipore), anti-CD35 biotin (8C12, BD Pharmingen), anti-CD16/32 biotin (FcεRII/III; UCSF Hybridoma Core), Alexa647-conjugated anti-Bcl6 (K112-91, BD Pharmingen), anti-GFP Alexa488 (Life Technologies) and anti-F4/80 biotin (Cedarlane Laboratories).

Sections were stained with the following secondary antibodies as previously described (Lu et al., 2017; Rodda et al., 2015): anti-FITC Alexa488, streptavidin Cy3, anti-goat AMCA, anti-Rabbit Alexa488 (Life Technologies), anti-Rabbit Alexa647, streptavidin Alexa555 (Life Technologies), anti-goat horseradish peroxidase, and streptavidin alkaline phosphatase. All secondary antibodies are from Jackson Immunoresearch unless otherwise noted.

Confocal microscopy on 30μm sections was performed as described previously (Bannard et al., 2013). All other images were captured with a Zeiss AxioObserver Z1 microscope.

RNAscope in situ hybridization

Performed as previously described (Lu et al., 2017) on 14μm sections using the RNAscope RED 2.5HD manual assay kit (Advanced Cell Diagnostics) (Wang et al., 2012). The RNAscope probes used targeted: *Ch25h* (NM_009890.1, targeting bp 115-1240), *Inmt* (NM_009349.3, targeting bp 3-1017) and *Pthlh* (NM_008970.4, targeting bp 173-1231).

Quantitative RT-PCR

Total RNA from pLNs was extracted using an RNeasy kit (Qiagen) and reverse-transcribed. Quantitative PCR was performed as described (Yi et al., 2012) with the following primers: *Inmt*-F CCTTCTCTACAGGAGGTGTAGG; *Inmt*-R GTTCTGCGGGGTGTAGTCAG; *Siglec1*-F GGTCAGCCAACAGTTCACTC; *Siglec1*-R GAGACTCCTGTGGGCACC; *Pdgfrβ*-F GCAGAAGAAGCCACGCTATG; *Pdgfrβ*-R CAGGTGGAGTCGTAAGGCAA; *Pthlh*-F GGAGTGTCCTGGTATTCCTGC; *Pthlh*-R CCCTTGTCATGCAGTAGCTGA; *Hprt*-F AGGTTGCAAGCTTGCTGGT; *Hprt*-R TGAAGTACTCATTATAGTCAAGGGCA. Data were analyzed using the comparative CT (2-ΔΔCt) method with *Hprt* as the reference. Data plotted and unpaired t-test p-value calculated with Prism (GraphPad).

Data Analysis

Semi-supervised clustering of scRNA sequencing data

For analysis of the transcriptional heterogeneity of uninfected pLN stromal cells, we analyzed only cells (unique barcodes) that passed quality control processing (above) and expressed at least 200 genes and only genes that were expressed in at least 3 cells, leaving us with 2,870 cells and 15,633 genes for further analysis. We analyzed the gene-cell expression matrix using the Seurat version 1.0 R package (Butler and Satija, 2017) for graph-based clustering and visualizations, all functions mentioned are from this package or the standard R version 3.4.2 package unless otherwise noted and were used with the default parameters unless otherwise noted. Normalized expression for gene i in cell j was calculated by taking the natural log of the UMI counts for gene i in cell j divided by the total UMI counts in cell j multiplied by 10,000 and added to 1. To

reduce the influence of variability in the number of UMIs, percentage of mitochondrial genes (only retaining cells with < 5% mitochondrial genes) and percentage of ribosomal genes (only retaining cells with < 30% ribosomal protein genes) on the clustering, we used the RegressOut function before scaling and centering the data for dimensionality reduction. Principle component analysis was run using PCA on the 1015 variable genes calculated with MeanVarPlot (x = (0.1,6), y = (0.5, 15)) and then extended to the full dataset with ProjectPCA. Based on the PCElbowPlot result we decided to use 24 principle components (PCs) for the clustering. We ran FindClusters for graph-based clustering over an array of resolutions and chose the resolution, 0.6, where there was the maximum number of clusters where each cluster had at least 20 differentially and significantly expressed genes (log2FoldChange > 1, FDR < 0.05). Any clusters with average pairwise Pearson correlations (cor.test) of significant PC scores of r > 0.80 were merged (this pertained to only the two clusters distinguished by CD34 expression). We ran RunTSNE (perplexity = 30 and iterations = 1000) and TSNEPlot to visualize the data with dimensionality reduction. Using FindAllMarkers with a likelihood-ratio test for zero-inflated data, 2,732 Pdgfrβ$^+$ and/or Pdgfrα$^+$ non-endothelial stromal cells were distinguished from neutrophils, mast cells, BECs, LECs, Schwann cells and keratinocytes (Table S1) and exclusively used for further analysis.

Next, we employed semi-supervised, K-nearest neighbor graph based clustering using least absolute shrinkage and selection operator (LASSO) regression (Satija et al., 2015) to resolve the well-described MRCs not distinguished in the unsupervised clustering. We combined known niche-associated stromal genes curated from the literature (Table S2) with the identified variable genes in the dataset and ran

AddImputedScore followed by the PCA, graph-based clustering and TSNE analysis as above (24 PCs, resolution 0.6). We used BuildClusterTree to report the hierarchical distance matrix relating an ‘average’ cell for each cluster.

For the analysis of the transcriptional heterogeneity of stromal cells from post-LCMV infected pLNs, we analyzed only cells that passed quality control processing (above), leaving us with 12,064 cells and 17,257 genes for further analysis. The post-infection non-endothelial stromal cells were identified and analyzed as above except using 24 PCs and a clustering resolution of 0.4.

Dataset aggregation and Canonical Correlation Analysis

To compare global gene expression between the uninfected and post-infection non-endothelial stromal cells, we merged the datasets using cellranger aggr (version 2.1, 10X Genomics, support.10xgenomics.com) to equalize read depth. We then imported the merged dataset, with the sample source of each cell tracked, to Seurat for analysis of log-normalized expression data. Data plotted and Mann-Whitney U test p-value calculated with Prism (GraphPad).

For analysis of cluster conservation across datasets we used the Seurat version 2.1.0 R package. After processing the uninfected and post-LCMV infection cells separately as above, the top 2000 variable genes from each dataset were used for canonical correlation analysis with RunCCA to identify a conserved gene correlation structure. Using CalcVarExpRatio to calculate the percentage of variance explained by the CCA vectors for each cell, we retained cells with 50% or more variance explained. Discarded cells were analyzed for cluster bias by obtaining the cluster assignments

from analysis of the datasets separately and calculating the percent of discarded cells from each cluster. The retained cells were then aligned with AlignSubspace with 12 PCs determined by inspection of DimHeatmap results. Alignment quality was assessed by Pearson correlation of averaged log-normalized gene expression (of genes found in both datasets) between datasets with cor.test and compared to the alignment of dissimilar cell types, FDCs and PvCs ($r = 0.78$, p-value $< 2.2 \times 10^{-16}$) to determine if the high alignment was reflecting similar heterogeneity in the datasets beyond housekeeping genes shared among all the cells. Subsequent integrated analysis for clustering and visualization was performed with RunTSNE and FindClusters. Overlap of differential gene list for each cluster between the uninfected and post-infection datasets was assessed by calculating the hypergeometric probability (phyper).

Cell cycle signature scoring

Enrichment for canonical cell cycle genes was assessed with CellCycleScoring (Tirosh et al., 2016)(www.satijalab.org/seurat/cell_cycle_vignette.html). Cells with an S.Score greater than 0.15 or G2M.Score greater than 0.2 were removed from post-infection FDCs with FilterCells before subclustering or comparison of uninfected and post-infection FDCs.

Differential gene expression

Since single-cell technologies currently capture only a portion of the transcripts in any cell, cells of the same type will not all report expression of exactly the same genes. This creates zero-inflated data making it challenging to determine differential expression

of lowly expressed genes. To address this issue, we summed the raw UMI counts for each gene in each cluster over groups of twenty cells and then treated the summed, or 'sudobulk' (Lun et al., 2016), samples as technical replicates for differential gene analysis between each cluster's sudobulk samples and all other sudobulk samples using DESeq2 version 1.14.1 (Love et al., 2014).

Subclustering analysis

Two CD34 subclusters were identified in the original graph based clustering of the uninfected dataset with 24 PCs and resolution 0.6, but had high PC correlation. DEGs between CD34 SC subclusters and between the $CD34^{+}$ Des^{+} SCs and all other cells in the dataset were calculated with DESeq2 as above and the intersection reported as DEGs for $CD34^{+}$ Des^{+} SCs. The post-infection FDCs were analyzed for further subclustering by removing cells enriched for cell cycle, normalizing and performing unbiased clustering as above. However, we found no unique marker genes for the $Cxcl12^{hi}$ subcluster calculating subcluster DEGs as above. DEGs for aligned uninfected and aligned post-infection FDCs from CCA were calculated with DESeq2 as above and DEGs distinct from those found in the comparison of non-FDC uninfected and post-infection stromal cells were reported.

Visualization

Log-normalized gene expression data (see above) was used for visualizations with violin plots (VlnPlot), tSNE plots (FeaturePlot) and expression comparison plots (GenePlot). Scaled log-normalized gene expression data was used for visualizations

with dot plots (DotPlot) and heatmaps (DoHeatmap). We reported DEG lists with write.xlsx (R package xlsx version 0.5.7). Additional packages used: dplyr (0.7.4), Matrix (1.2-11), lars (1.2), rJava (0.9-9), Hmisc (4.0-3) and cowplot (0.8.0).

Acknowledgements:

We thank Y. Xu and J. An for technical assistance, H.-Y. Huang for the stromal cell isolation protocol, E. Wan, S. Wong and the Genomics Core Facility for mRNA library processing, sequencing and alignment, R. Camire for preparation of REX3 LNs, M. Subramaniam for coding advice, T. Nagasawa for the *Cxcl12*-GFP mice, K. Rajewsky for the *Cr2*-Cre mice, D. Myers and J. Roose for the *Nur77*-GFP mice and J. Browning for LTβR-Fc and TNFR1-Fc. This work and L.B.R were supported by National Institutes of Health Grant AI040098 and AI45073. E.L. was supported by NSF grant 1144247. C.L.S. was supported by National Institutes of Health Grant K08AI121421 and A.D.L. by National Institutes of Health Grant R01CA204028. S.A.L. was supported by Swiss National Science Foundation Grant 31003-146944/1. J.G.C. is an investigator of the Howard Hughes Medical Institute. The authors declare no conflict of interest.

Table S1. DEGs for each Pdgfrβ$^-$ Pdgfrα$^-$ pLN stromal cell cluster. Related to Figure 1.

DEGs for the minor populations of BECs, LECs, keratinocytes, mast cells, neutrophils and Schwann cells removed from the subsequent analysis. The statistics reported are the p-value (p_val), natural log fold change (avg_diff), percent of cells within the cluster expressing the gene (pct.1) and percent of cells not in the cluster expressing the gene (pct.2). Only the top 20 genes for each cell type are reproduced here because of space constraints.

BECs	p_val	avg_diff	pct.1	pct.2
Fabp4	6.40577E-85	5.252179497	0.791	0.056
Gpihbp1	2.03289E-77	3.471561414	0.86	0.005
Cldn5	1.85708E-55	3.406304876	0.744	0.012
Cd36	1.76036E-62	3.328127875	0.744	0.012
Rgcc	4.81387E-72	3.099413528	0.884	0.022
Ly6c1	2.62779E-66	2.978429283	0.93	0.125
Car4	9.39528E-57	2.803395784	0.698	0.007
Timp4	3.60965E-47	2.793461793	0.558	0.008
Esam	2.23452E-82	2.709298167	0.977	0.011
Sdpr	1.37273E-89	2.61927262	0.86	0.164
Cdh5	9.15924E-74	2.61255146	0.884	0.008
Egfl7	3.73722E-71	2.612076811	0.837	0.017
Cd300lg	1.23556E-84	2.589567974	0.86	0.035
Tspan13	9.97427E-67	2.555346336	0.907	0.018
Cav1	3.47899E-83	2.549921588	0.791	0.129
Mgll	2.87821E-59	2.523267242	0.698	0.018
Cav2	1.16688E-90	2.455835639	0.86	0.079
Aqp7	6.02291E-52	2.289128498	0.605	0.002
Tm4sf1	5.62332E-49	2.273285741	0.698	0.123
Fabp5	1.64693E-37	2.264368673	0.535	0.075
LECs	p_val	avg_diff	pct.1	pct.2
Glycam1	3.51417E-07	3.843531156	0.75	0.081
Cd55	3.69519E-21	3.090628935	1	0.2
Cpe	3.91785E-05	2.59652139	0.75	0.119
Cldn5	4.59682E-07	2.450759729	1	0.021
Jam3	4.4067E-25	2.424479917	1	0.361
Cyp4b1	0.000131543	2.29664283	0.75	0.028
Dusp2	1.84956E-05	2.131807884	0.5	0.025
Lyve1	1.34188E-17	2.129740349	1	0.01
Gimap5	3.43591E-13	2.105914389	1	0.011
Gimap6	7.91083E-07	2.100369119	1	0.044
Cmah	7.31879E-10	2.089038955	1	0.024

Itga2b	1.30859E-09	1.984727284	1	0.059
Ccl20	3.76926E-06	1.955818221	0.5	0.002
Lrg1	5.49058E-06	1.933193496	1	0.264
Rasip1	0.000193736	1.918933222	0.75	0.019
Msr1	6.6049E-09	1.884800829	0.75	0.001
Timp3	2.40217E-05	1.84796994	1	0.362
Cldn11	8.48873E-09	1.846400077	0.75	0.002
Cpne2	1.28638E-09	1.799353446	0.75	0.109
Pvrl2	1.39398E-10	1.753677657	0.75	0.213
Keratinocytes	p_val	avg_diff	pct.1	pct.2
Krt19	2.20485E-34	4.392986508	1	0.013
Krt18	2.78206E-33	3.763982311	1	0.008
Ly6d	1.26972E-16	3.401284904	0.875	0.01
Areg	4.82556E-17	3.278697712	0.625	0.002
Prlr	7.93102E-33	3.227337716	0.75	0.017
Fgg	1.8505E-12	3.17026905	0.5	0.001
Krt8	4.45505E-27	3.157348783	1	0.001
Epcam	3.08585E-25	3.099870554	1	0.01
Wfdc2	8.31622E-17	2.937108683	0.75	0.002
Slc12a2	1.87932E-34	2.771409822	0.875	0.039
Gata3	6.24673E-22	2.729835424	1	0.004
Ptn	2.03472E-10	2.631519281	0.875	0.529
Cldn3	1.08711E-21	2.483636539	1	0.002
Fgb	4.04219E-11	2.365084983	0.5	0.001
Cldn4	1.04597E-21	2.341221397	1	0.001
Krt7	1.78694E-39	2.298624682	1	0.045
Hp	2.36471E-08	2.276606788	0.625	0.012
Cited1	3.84985E-14	2.201700234	0.75	0.009
Plk2	1.3729E-12	2.191311457	0.875	0.117
Fam25c	6.06967E-13	2.181225826	0.625	0.001
Mast Cells	p_val	avg_diff	pct.1	pct.2
Ccl4	1.3569E-99	5.23903461	0.972	0.035
Ccl3	2.5408E-120	5.101414056	1	0.031
Ccl6	2.58002E-91	4.406078581	0.917	0.014
Hdc	7.37063E-92	3.745342577	1	0.011
Rgs1	4.50214E-72	3.669880634	0.917	0.006
Tyrobp	3.24354E-83	3.577463255	1	0.027
Fxyd5	3.775E-113	3.27115347	1	0.085
Ccl9	1.286E-105	3.252442386	1	0.271
Mcpt8	1.36744E-52	3.17144705	0.639	0.012
Alox5ap	3.92371E-83	3.0939289	1	0.017

Fcer1g	7.96438E-73	3.086811215	0.972	0.025
Osm	1.09132E-60	3.041365322	0.806	0.008
Lilr4b	8.84446E-79	2.986936011	0.944	0.001
Rgs2	2.39774E-79	2.956394036	0.917	0.068
Cd69	4.62917E-66	2.909819434	0.806	0.03
Cd7	2.06326E-72	2.879305218	0.917	0.003
Il6	2.42003E-43	2.877479496	0.806	0.136
Cyp4f18	4.37508E-71	2.749974579	0.917	0.006
Cd200r3	6.91016E-69	2.740579893	0.889	0.002
Cyp11a1	4.2022E-77	2.726243504	0.917	0.004
Neutrophils	p_val	avg_diff	pct.1	pct.2
Hba-a1	5.35677E-38	4.487183268	0.237	0.059
Hbb-bs	9.0504E-52	4.426413744	0.237	0.1
Hbb-bt	6.79918E-20	3.897630116	0.211	0.022
Elane	8.48267E-44	3.113112501	0.211	0.026
Mpo	2.00381E-35	2.747870801	0.211	0.023
Ly6c2	4.20952E-46	2.746990954	0.368	0.022
Lyz2	1.12306E-27	2.467657099	0.421	0.035
Stmn1	1.12504E-79	2.348637309	0.789	0.142
Hmgb2	6.3377E-103	2.347595235	0.868	0.339
Prtn3	8.42266E-60	2.304755415	0.263	0.082
Top2a	1.00168E-55	2.230214445	0.737	0.01
Ube2c	4.24187E-45	2.053077894	0.605	0.007
Car2	6.88099E-19	2.003332257	0.237	0.007
Ctsg	1.91747E-15	1.907218936	0.211	0.007
2810417H13Rik	4.24251E-48	1.89450549	0.711	0.007
Vpreb3	5.55257E-18	1.863296267	0.263	0.004
H2afx	6.06775E-83	1.858251789	0.816	0.173
Rac2	4.42764E-28	1.853262786	0.632	0.024
Tyrobp	1.81944E-14	1.810953117	0.447	0.034
Cd24a	3.9941E-31	1.793532187	0.632	0.123
Schwann Cells	p_val	avg_diff	pct.1	pct.2
Mpz	4.25453E-30	5.034845664	0.778	0.013
Mbp	2.55251E-59	4.571109144	1	0.028
Plp1	2.92864E-35	3.809767284	1	0.012
Pmp22	9.4872E-71	3.777127374	1	0.574
Gatm	6.71141E-27	3.571155911	1	0.003
Cnp	5.30525E-63	3.459225728	1	0.112
Kcna1	3.65247E-25	3.451003611	1	0.002
Ncmap	6.00478E-15	2.891445356	0.556	0.001
Art3	3.46267E-27	2.679174335	1	0.045

Cryab	5.81633E-51	2.670171497	1	0.482
Mal	6.58212E-22	2.659277231	0.889	0.001
Fxyd6	2.91027E-24	2.559897155	0.556	0.053
Plekhb1	1.44321E-21	2.453659464	0.889	0.003
Cldn19	3.42976E-13	2.426843391	0.556	0
Prx	5.90723E-22	2.407294434	0.556	0.01
Dbi	1.66729E-30	2.369359194	1	0.696
Cd9	2.86852E-29	2.369044835	1	0.85
S100b	2.31012E-17	2.319899277	0.778	0.023
Cd59a	1.73866E-26	2.315407625	1	0.03
Pllp	6.56113E-14	2.294070053	0.556	0.001

Table S2. Canonical stromal genes used for LASSO-supervised clustering. Related to Figure 1.

Curated list of canonical LN stromal genes used for LASSO-supervised graph-based clustering of pLN non-endothelial stromal cells.

Canonical Stromal Genes used for LASSO semi-supervised clustering	
Pdpn	Icam1
Pdgfrb	Icam2
Pdgfra	Madcam1
Cxcl13	Il6
Cxcl12	Il7
Ccl21a	Acta2
Ccl19	Col4a1
Cxcl16	Col1a1
Ch25h	Col3a1
Bst1	Vtn
Tnfsf11	Des
Cr2	Fn1
Fcgr2b	Cnn1
Mfge8	Itga7
Tnfsf13b	Cd34
Ltbr	Cxcl9
Vcam1	Cxcl10

Table S3. Average gene expression for eight pLN stromal clusters from the uninfected and post-infection datasets. Related to Figure 1.
Uninfected clusters are from the dataset independent analysis and post-LCMV infection clusters are from the CCA conserved analysis. The values reported are averaged log-transformed gene expression across cells in each cluster for both datasets for each gene detected (cluster_mean) and percent of cells within the cluster expressing the gene (pct_in). Only a portion of the table is reproduced here because of space constraints.

	Uninf TRC cluster_mean	Uninf TRC pct_in	Uninf Ccl19^{lo} TRC cluster_mean	Uninf Ccl19^{lo} TRC pct_in	Uninf Inmt^{+} SC cluster_mean	Uninf Inmt^{+} SC pct_in
Serping1	3.732934507	1	3.55618281	1	3.313937919	0.997439181
B2m	4.577333976	1	4.164833542	0.996742671	4.058459503	1
Igfbp7	4.344737159	1	4.274274242	1	4.145474764	1
C1s1	2.586851643	1	2.631344111	0.988599349	2.729492506	0.989756722
Apoe	5.921475298	1	6.258054509	1	6.057622891	1
Mfge8	4.446448421	1	3.654145362	0.998371336	2.151659481	0.939820743
Clu	5.448121373	1	4.414297271	1	3.14233677	0.991037132
H2-K1	3.06600569	1	2.818349978	0.995114007	2.588569276	0.976952625
H2-D1	3.844874362	1	3.681030552	1	3.632209266	0.994878361
C3	3.805912626	1	4.351280377	1	4.230129189	1
Malat1	6.007412283	1	6.384985991	0.998371336	6.437556873	1
Fth1	4.241245748	1	4.308191797	1	4.310925897	0.99871959
Cpxm1	2.815708938	0.998454405	2.23885873	0.95276873	2.437607273	0.947503201
Cxcl12	3.301118283	0.998454405	4.586714678	1	4.765370819	1
Dcn	3.857567021	0.998454405	4.512409814	1	5.315660066	1
Rpl13	3.746719427	0.998454405	3.601535897	0.988599349	3.611441795	0.996158771
Itm2b	3.34497754	0.998454405	3.227186659	0.996742671	3.283504857	1
Ubb	3.563098772	0.998454405	3.68710286	0.995114007	3.850320962	0.99871959
Vtn	2.925975906	0.998454405	2.726025574	0.98534202	1.877255514	0.861715749
Ftl1	3.523762232	0.99690881	3.657916575	0.995114007	3.925115636	0.99871959

Tables S4-S11. DEGs for each pLN non-endothelial stromal cell cluster. Related to Figure 2-6.

DEGs for TRCs (Table S4), Ccl19^{lo} TRCs (Table S5), Cxcl9^{+} TRCs (Table S6), MRCs (Table S7), PvCs (Table S8), CD34^{+} SCs (Table S9), Inmt^{+} SCs (Table S10) and FDCs (Table S11) as determined by difference between the average expression of sudobulk samples in the cluster and the average expression of sudobulk samples not in the cluster (log2 fold change). Presented are only genes with log2 fold change >1, FDR < 0.05 and the percent of cells expressing the gene within the cluster > 10%. Also reported are the average log-normalized expression within the cluster (cluster_mean), p-value (pvalue), Benjamini and Hochberg adjusted p-value (padj), pct_in (percentage of cells in the cluster of interest) and pct_out (percentage of cells not in the cluster of interest). Table S9 also includes the Top DEG by CD34^{+} Des^{+} SCs compared to all other clusters and pairwise to CD34^{+} Des^{-} SCs. Only the top 20 DEGs for each subset are reproduced here because of space constraints.

Table S4 TRCs	cluster_mean	log2 Fold Change	pvalue	padj	pct_in	pct_out
Il13ra2	0.749049	4.989556	2.8187E-156	1.7118E-152	0.488408	0.02685851
Thbs4	0.4167931	4.705989	7.80029E-63	1.6058E-60	0.3214838	0.01103118
Slc7a11	1.65877	4.624657	9.9006E-130	2.405E-126	0.8748068	0.07625899
Fabp7	0.496731	4.530699	2.01687E-95	1.16652E-92	0.4404946	0.01822542
Stc2	1.54148	4.41246	2.3153E-118	3.5152E-115	0.8887172	0.08920863
Ddah1	0.5240977	4.161922	5.66119E-97	3.82005E-94	0.488408	0.02446043
Cntn1	0.2897056	4.096307	1.54793E-71	4.273E-69	0.2905719	0.00911271
Krt20	0.401711	4.049311	5.44645E-75	1.74086E-72	0.3972179	0.01870504
Ly6i	1.132105	3.944533	1.1126E-127	2.2522E-124	0.7217929	0.101199
Dbx2	0.2371595	3.909334	1.96417E-63	4.18539E-61	0.2426584	0.00911271
Il4i1	0.5438377	3.881893	1.23743E-75	4.17493E-73	0.431221	0.05371703
Qprt	0.2228753	3.872429	2.85524E-54	4.12855E-52	0.2302937	0.009592326
Adamts8	0.2747515	3.839975	4.48008E-63	9.3819E-61	0.2998454	0.01390887
Glycam1	0.338409	3.800047	6.90822E-29	3.16631E-27	0.2720247	0.02494005
Clca3a1	0.1918978	3.72498	3.59319E-44	3.23281E-42	0.2040185	0.005755396
Wisp1	0.274453	3.550455	3.15062E-50	3.5764E-48	0.2874807	0.01630695
Ubd	0.9876859	3.536443	3.04293E-25	1.13026E-23	0.6228748	0.0853717
Cfi	0.1836673	3.487316	5.80244E-45	5.50597E-43	0.2132921	0.00911271
Tnfrsf11b	0.1355047	3.485961	3.5234E-39	2.43155E-37	0.1483771	0.002877698
Pianp	0.4827042	3.434208	2.82274E-87	1.3714E-84	0.4358578	0.04268585

Table S5 Ccl19lo TRCs	cluster_mean	log2Fold Change	pvalue	padj	pct_in	pct_out
Vsnl1	0.2233391	1.80865	1.09393E-20	2.00153E-17	0.1938111	0.05146364
Cxadr	0.5467424	1.699125	6.58541E-26	1.80737E-22	0.4120521	0.1430595
Sfrp2	0.6269986	1.682118	9.79805E-19	1.34454E-15	0.4071661	0.1482531
Ch25h	0.3102118	1.544159	4.55509E-10	1.21965E-07	0.2166124	0.05996223
Spns3	0.1243502	1.535433	6.83518E-12	3.26246E-09	0.1042345	0.03305005
Foxq1	0.2501351	1.438894	1.79021E-11	7.0189E-09	0.2052117	0.07459868
Cilp	0.1600573	1.434421	3.59176E-10	9.85758E-08	0.1254072	0.06137866
Fam180a	0.6762524	1.426977	5.21954E-28	2.86501E-24	0.5	0.2157696
Adamts5	0.8141388	1.35799	2.22978E-19	3.49692E-16	0.519544	0.2766761
Syt13	0.4778299	1.326675	8.49453E-12	3.73012E-09	0.3990228	0.1458924
Sox11	0.1605881	1.245446	1.02083E-08	1.86778E-06	0.1384365	0.05571294
Foxp2	0.2074194	1.236643	4.26567E-11	1.46339E-08	0.1889251	0.07884797
Bmp3	0.1978444	1.184537	1.67625E-08	2.83106E-06	0.1693811	0.07365439
Gas6	2.714113	1.176947	9.09695E-24	1.99733E-20	0.97557	0.8356941
Bmp4	0.3785546	1.154329	1.99716E-08	3.32195E-06	0.2980456	0.1491974
Nos1ap	0.4896618	1.141772	2.05055E-14	1.73161E-11	0.4055375	0.1983003
Tnfsf13b	1.496202	1.138991	5.38222E-26	1.80737E-22	0.8550489	0.5783758
Fam214a	0.1721672	1.132128	8.32886E-10	2.03187E-07	0.1612378	0.07223796
Sostdc1	0.7891273	1.119994	1.16052E-08	2.05488E-06	0.5032573	0.2219075
Lrg1	0.6404856	1.110749	2.37905E-07	2.71561E-05	0.4201954	0.227101

Table S6 Cxcl9^{+} TRCs	cluster_mean	log2Fold Change	pvalue	padj	pct_in	pct_out
Bmp2	0.5444374	2.944047	5.47971E-08	4.16309E-05	0.3392857	0.08594918
Gbp2	1.817656	2.914624	2.7507E-08	2.38816E-05	0.8035714	0.245142
Gimap6	0.3387597	2.839134	5.57898E-07	0.000242184	0.1428571	0.0284006
Gbp4	0.7289751	2.748814	2.09033E-06	0.000800658	0.5178571	0.04633782
H2-Aa	1.277584	2.678755	2.83403E-07	0.000147631	0.5535714	0.1756353
Cxcl9	2.536635	2.627817	7.05548E-06	0.002355989	0.8571429	0.2017937
H2-DMa	0.7888824	2.625052	4.05352E-07	0.000188532	0.4821429	0.09005979
Igtp	1.445113	2.618975	1.69265E-07	0.000110217	0.6785714	0.2286996
Fam26f	0.8322635	2.501053	4.15034E-09	4.91362E-06	0.5357143	0.156577
Iigp1	2.808195	2.366408	5.7541E-08	4.16309E-05	0.9464286	0.4809417
Glycam1	0.4539042	2.313761	4.77877E-06	0.001681998	0.1071429	0.08295964
Mpeg1	0.2670033	2.267977	5.02535E-05	0.01211946	0.2142857	0.01831091
Gbp9	0.497066	2.25746	1.22716E-05	0.003716575	0.4464286	0.08333333
Gbp3	0.8000479	2.239069	8.13364E-06	0.002648109	0.5892857	0.1150972
Egfl7	0.2185299	2.198822	0.000151514	0.0285967	0.1071429	0.01345291
Cd274	0.1899986	2.18028	0.000148975	0.02853096	0.1607143	0.02242152
Cxcl10	2.360371	2.126212	7.00058E-05	0.01519475	0.8214286	0.3897608
Mmp9	0.2956636	2.07083	0.000251003	0.04137742	0.1964286	0.06427504
H2-Eb1	1.065006	2.065233	7.68612E-05	0.01640924	0.5357143	0.2126308
Coch	0.2684996	2.058134	4.82313E-05	0.01185126	0.1428571	0.02503737

Table S7 MRCs	cluster_mean	log2FoldChange	pvalue	padj	pct_in	pct_out
Hamp2	1.543754	6.372527	8.05702E-84	6.02101E-80	0.8265306	0.01936219
Sdpr	0.9474575	2.283594	3.48705E-08	2.00452E-05	0.622449	0.1492027
Tnfsf11	1.278593	2.240442	8.56357E-06	0.001684094	0.7653061	0.1249051
Mrps6	1.068757	2.074569	6.10205E-10	6.51438E-07	0.6836735	0.2418375
Slc5a3	1.122506	2.05705	1.98802E-07	7.07451E-05	0.7346939	0.2034928
Clec14a	0.840863	2.006911	4.56057E-16	1.70406E-12	0.5510204	0.2471526
Ahr	0.7308572	2.003337	2.83613E-07	9.21495E-05	0.5102041	0.1655277
Id1	1.274594	1.914378	1.92635E-05	0.002665851	0.6734694	0.2312073
Rnpep	0.5253872	1.891976	9.59519E-10	8.96311E-07	0.3673469	0.1955201
Cxcl13	4.172715	1.872876	5.58471E-05	0.005318473	1	0.7957479
Cdk8	0.542793	1.861075	2.54429E-09	1.7285E-06	0.4183673	0.1427487
Nkd2	0.3679148	1.841323	9.08956E-05	0.007991326	0.2959184	0.07137434
Prkg2	0.642101	1.815987	0.00039592	0.02143991	0.4897959	0.08580106
Emb	0.7644737	1.800005	0.000186059	0.01363158	0.5204082	0.1370539
1500015O10Rik	0.3598939	1.79229	2.53619E-05	0.003384454	0.2857143	0.0770691
Ramp1	0.6615926	1.787305	0.000256501	0.01666807	0.4897959	0.1116173
Fam161a	0.3407331	1.707049	2.98174E-05	0.003815446	0.3163265	0.09225513
Smad6	0.3752084	1.689574	9.55749E-05	0.008209555	0.3367347	0.0808656
Prdm11	0.2619	1.655821	9.13263E-06	0.0017182	0.2346939	0.07668945
Slc22a4	0.4424263	1.649921	0.000487284	0.02495697	0.377551	0.1074412

Table S8 PvCs	cluster_mean	log2Fold Change	pvalue	padj	pct_in	pct_out
Tinagl1	2.555428	6.739065	1.18376E-16	1.07646E-13	0.9545455	0.02008929
Sdc1	1.368182	4.7471	4.6858E-17	4.58884E-14	0.6363636	0.07254464
Nrip2	0.5371942	4.73933	2.35314E-09	4.91112E-07	0.2954545	0.02157738
Lmod1	1.249923	4.736628	1.45798E-08	2.50832E-06	0.6818182	0.03125
Itga7	0.6693867	4.67754	2.05847E-07	2.51984E-05	0.4545455	0.009672619
Serpine2	2.076787	4.574896	2.47077E-07	2.91254E-05	0.9318182	0.04315476
Fabp4	1.322839	4.559726	5.04993E-07	5.22688E-05	0.4318182	0.05022321
Mcam	0.6720522	4.519759	5.48724E-07	5.50064E-05	0.4772727	0.01227679
Myl9	3.230688	4.389395	8.48274E-33	5.39969E-29	1	0.4579613
Dmd	0.7213596	4.342565	1.89113E-18	2.4076E-15	0.4772727	0.03869048
Rbpms2	0.4257377	4.254027	3.70502E-07	4.06626E-05	0.25	0.01488095
Fhl2	0.780881	4.21382	2.42585E-07	2.88631E-05	0.4772727	0.03125
Cystm1	0.6033929	4.128028	2.14965E-06	0.000172116	0.4090909	0.006696429
Acta2	3.867445	4.076574	1.61138E-11	5.54446E-09	0.9545455	0.4706101
Mef2c	0.8151811	3.964453	1.2531E-06	0.000106355	0.4545455	0.0453869
Ppp1r14a	1.503291	3.85587	2.51582E-07	2.93843E-05	0.75	0.125372
Lims2	0.7914984	3.832052	2.41742E-05	0.001367829	0.5227273	0.01934524
Cyp4b1	0.6418967	3.819295	2.68556E-05	0.001468196	0.3181818	0.01674107
Hrct1	0.5070298	3.786524	3.88225E-07	4.22435E-05	0.2954545	0.04575893
Ndufa4l2	0.9087331	3.786277	7.31106E-06	0.000487315	0.4772727	0.05096726

Table S9 CD34+ SCs	cluster_mean	log2Fold Change	pvalue	padj	pct_in	pct_out
Pi16	0.3160119	5.916527	1.55952E-80	3.6973E-77	0.1261062	0.01184211
Igfbp6	0.9866069	5.896211	1.1234E-174	1.3316E-170	0.4557522	0.03903509
Col15a1	0.2649829	4.787936	1.27207E-47	7.18051E-45	0.1570796	0.005263158
Nov	0.209843	4.755972	2.89797E-32	7.98895E-30	0.1216814	0.009210526
Ly6c1	0.858004	4.278262	2.3111E-47	1.24526E-44	0.4845133	0.05263158
Cd248	0.58313	4.174525	5.3258E-141	3.1566E-137	0.409292	0.04824561
Cd34	1.337254	4.162066	4.52704E-49	2.8244E-46	0.7433628	0.08333333
Ace	0.1636142	4.041771	2.9765E-31	7.20069E-29	0.1106195	0.004385965
Lama2	0.2168381	3.961615	3.22387E-34	9.79893E-32	0.1570796	0.007894737
Fndc1	0.1670379	3.899525	8.25966E-31	1.9198E-28	0.1061947	0.00745614
Spon2	0.49682	3.833183	2.51684E-76	4.97243E-73	0.3495575	0.04780702
Pla2g2e	0.1481636	3.748596	9.05986E-22	1.01317E-19	0.119469	0.006140351
Nppc	0.1908396	3.738197	1.01656E-16	7.82484E-15	0.1216814	0.008333333
Pcolce2	0.8338366	3.7274	2.2889E-22	2.6864E-20	0.4800885	0.05131579
Thy1	0.1616478	3.688045	3.33774E-22	3.87898E-20	0.1150442	0.01008772
Apod	0.6683912	3.672984	7.74253E-49	4.589E-46	0.3495575	0.1184211
Scd1	0.2110343	3.579053	1.89698E-37	6.61375E-35	0.1747788	0.01359649
Creb5	0.1530996	3.529113	3.04411E-30	6.44372E-28	0.1061947	0.007894737
Mfap5	0.8905082	3.512469	1.9504E-19	1.8496E-17	0.449115	0.06052632
Lsp1	0.2887488	3.393917	9.5489E-54	6.65839E-51	0.2190265	0.03245614

CD34+ Des+ SCs	cluster_ mean	log2FoldCha nge vs All	padj vs All	pct_in CD34+ Des+ SC	pct all not CD34+ Des+ SC	log2FoldChan ge vs Des-	padj vs Des-	pct_in CD34+ Des- SC
S100a4	0.7260 512	3.062509	3.2734 9E-30	0.4716157	0.1038753	3.019978	5.0451 2E-20	0.08520179
Gdf15	0.1963 633	1.47383	0.0028 38927	0.139738	0.0679185	2.781844	1.2001 6E-06	0.02242152
Nppc	0.3314 625	3.203204	1.2935 2E-10	0.2052402	0.01078706	2.760252	5.9501 7E-06	0.03587444
Pla2g2e	0.2672 514	3.589559	4.0189 1E-15	0.2139738	0.007590891	2.588694	9.8290 7E-07	0.02242152
Ccl7	1.4992 62	1.086594	0.0031 68424	0.628821	0.6084698	2.313296	3.3742 6E-07	0.3587444
Ptn	2.7086 36	1.579462	0.0016 15722	0.9650655	0.5045945	2.230303	4.8519 6E-53	0.5112108
Sqle	0.2412 918	1.709846	0.0002 3758	0.1834061	0.05553336	2.183026	2.6393 5E-05	0.03139013
Ankrd33b	0.1250 517	1.619647	0.0001 291	0.1310044	0.03156213	2.143984	0.0022 04222	0.00896861
Nov	0.3568 566	3.677048	5.4113 2E-14	0.2008734	0.01198562	2.042205	0.0082 22406	0.04035874
Has1	0.3786 212	2.25825	2.4120 7E-05	0.2401747	0.02077507	2.021424	0.0006 34351	0.05829596
Ccdc3	0.5726 689	2.452151	3.6175 4E-08	0.4017467	0.07510987	2.01048	4.3916 6E-07	0.0896861
Msmo1	0.3849 675	1.499357	0.0006 6734	0.2576419	0.1130643	1.981287	2.7105 8E-07	0.07174888
Mapkapk3	0.1756 626	1.138621	0.0185 3334	0.1790393	0.06871754	1.95177	0.0031 3328	0.02242152
Fgf1	0.2891 864	1.914158	1.9702 9E-13	0.2532751	0.08230124	1.90856	9.2271 2E-05	0.04035874

Hmgcs1	0.4270549	1.952582	7.2840 7E-13	0.2925764	0.1534159	1.84369	3.8862 8E-06	0.1300448
Cyp51	0.2255598	1.733461	2.5835 4E-05	0.1659389	0.06751898	1.826402	0.0024 0372	0.04035874
Fdft1	0.2159451	1.837043	2.2345 1E-09	0.1703057	0.06831802	1.777514	0.0004 72313	0.04932735
Pmvk	0.2615267	1.300831	1.1546 5E-08	0.2139738	0.1410308	1.773373	0.0001 72787	0.06278027
Dusp8	0.1204281	1.570702	0.0001 07825	0.1222707	0.0311626	1.757469	0.0160 6875	0.01345291
Fdps	0.4289139	1.995006	7.5570 6E-09	0.2620087	0.1414303	1.712046	5.2411 6E-05	0.1121076

Table S10 Inmt+ SCs	cluster_mean	log2Fold Change	pvalue	padj	pct_in	pct_out
Cyp2e1	0.4639256	2.860625	1.04836E-21	2.47371E-19	0.2676056	0.04613019
6530403H02 Rik	0.1254314	2.583327	1.44753E-24	5.97728E-22	0.1024328	0.02306509
Cyp2f2	1.001535	2.550769	1.05775E-20	2.07283E-18	0.5326504	0.1342901
Kcnk3	0.2792603	2.481562	1.57999E-17	1.77358E-15	0.2048656	0.03946694
Stc1	1.54005	2.281236	2.31486E-17	2.549E-15	0.7477593	0.2362891
Nap1l5	0.1925476	2.153221	1.91026E-20	3.68108E-18	0.1510883	0.05125577
Cadm1	0.2770494	2.116825	3.19543E-16	3.05335E-14	0.2189501	0.06355715
Clec1b	0.1736487	2.075141	5.0814E-18	6.25013E-16	0.1382843	0.0471553
Ddit4l	0.7924591	2.074117	3.71167E-22	9.53653E-20	0.5108835	0.1870835
Inmt	2.805723	2.025912	4.97509E-16	4.60176E-14	0.943662	0.506407
Fam150b	0.1704569	1.867333	3.53957E-09	9.40793E-08	0.1293214	0.04100461
Hlf	0.1521991	1.823973	2.70095E-12	1.32324E-10	0.1229193	0.04510507
Cxcl5	0.224041	1.811948	1.24536E-08	3.03773E-07	0.1459667	0.04869298
Gli1	0.1567431	1.81126	4.84483E-14	3.37445E-12	0.1306018	0.04766786
Atp1b1	0.5989289	1.80351	3.13609E-17	3.38873E-15	0.390525	0.1752947
Ptgs2	0.3566094	1.767223	4.18733E-14	2.95207E-12	0.2087068	0.1076371
Fzd10	0.2218944	1.76584	4.30165E-13	2.56369E-11	0.184379	0.07432086
Ralgps2	0.2230438	1.717325	6.46687E-13	3.64732E-11	0.177977	0.07175807
Mt1	1.198209	1.717111	1.4114E-12	7.25269E-11	0.5544174	0.3792927
Fbn2	0.2051434	1.715856	2.81442E-10	9.29882E-09	0.1587708	0.06355715

Table 11 FDCs	cluster_ mean	log2Fold Change	pvalue	padj	pct_in	pct_out
Cr2	2.897865	8.744426	4.73721E-35	5.23075E-32	0.975	0.01374443
A230065H16Rik	1.574297	8.134377	1.0714E-113	1.3013E-109	0.825	0.01225854
Serpina1e	1.453062	6.553883	3.38731E-14	6.23367E-12	0.625	0.03566122
Fcgr2b	1.698352	5.841533	1.67939E-07	8.32565E-06	0.85	0.01263001
Fcer2a	1.16355	5.678386	8.80568E-08	4.69096E-06	0.6	0.004086181
Stra6	1.207371	5.522019	5.37235E-07	2.28956E-05	0.75	0.004829123
Fabp5	1.613137	5.434106	7.68534E-11	8.18825E-09	0.775	0.0564636
Aplp1	0.9717693	5.417557	2.46074E-07	1.1767E-05	0.675	0.01114413
Fyb	0.9047565	5.331599	1.1368E-12	1.79318E-10	0.65	0.02600297
Mlc1	0.9806185	5.272432	2.26393E-11	2.74977E-09	0.725	0.02488856
Hamp	0.648974	5.137037	4.16746E-06	0.000143801	0.325	0.009658247
Slc1a2	0.9894346	5.072933	2.77555E-06	9.85388E-05	0.75	0.01448737
Tbc1d8	0.6902075	5.064666	6.921E-11	7.50558E-09	0.575	0.01300149
Nceh1	0.6434465	5.034716	9.96214E-10	8.28879E-08	0.575	0.01708767
Nostrin	0.7605382	4.979163	1.38544E-05	0.000394087	0.525	0.007800892
Itgb4	0.8536383	4.907982	2.23256E-07	1.07606E-05	0.675	0.01634473
Cilp	2.102386	4.906567	6.52599E-08	3.61939E-06	0.975	0.06240713
Ctsh	3.216215	4.902506	3.45962E-16	8.75429E-14	1	0.2968053
Igfals	0.8838751	4.76485	2.4176E-05	0.000636967	0.65	0.005943536
Tmem37	0.7381677	4.727844	3.67264E-05	0.000919441	0.575	0.01002972

Table S12. DEGs between uninfected and post-infection FDCs. Related to Figure 7.

DEGs (absolute value log2 fold change >1, FDR < 0.05, percent of cells expressing the gene within the cluster > 10%) between aligned uninfected FDCs and aligned post-LCMV infection FDCs that were not found in the comparison of all other clusters of uninfected stromal cells to all other clusters of post-infection stromal cells. Calculated as for Tables S3-S11 with statistics as in Table S3-S11.

	cluster_mean_in Post-Inf FDCs	log2Fold Change	padj	pct_in Post-Inf FDCs	pct_in Uninf FDCs	cluster_mean_in Uninf FDCs
Fn1	0.9490418	2.365297	2.5931E-08	0.6100629	0.2325581	0.2299212
Ramp2	0.42954	1.775996	0.003261599	0.3459119	0.1162791	0.07283303
Cdkn1a	0.8618666	1.696227	0.001407639	0.509434	0.1860465	0.2072278
H1f0	0.4962667	1.649173	0.001859252	0.3836478	0.2325581	0.1929719
Col1a1	1.080098	1.646524	2.25682E-06	0.5786164	0.3023256	0.4157179
Ccl2	0.8451077	1.562202	0.02314587	0.5031447	0.2325581	0.2181577
Ppic	0.7696146	1.458461	0.002250426	0.572327	0.372093	0.330875
Col6a1	0.6502849	1.451784	0.003410173	0.4465409	0.2790698	0.2677593
Crym	0.7783992	1.432634	0.001419974	0.4716981	0.2325581	0.2514353
S100a10	0.7880668	1.428468	0.003311741	0.5220126	0.3255814	0.2992189
Igfbp3	1.222159	1.409342	0.000197282	0.6226415	0.4186047	0.5047261
Col1a2	1.420635	1.408958	1.19253E-05	0.6855346	0.5116279	0.6331883
Sparc	2.499695	1.330814	1.07073E-12	0.8993711	0.8604651	1.706497
Gas6	0.5412308	1.265353	0.0267946	0.3710692	0.2093023	0.2511232
Col3a1	0.9106448	1.225388	0.002329407	0.6100629	0.372093	0.4839729
Lhfp	0.4733418	1.2152	0.04135299	0.408805	0.2790698	0.2258725
Ly6e	1.32031	1.179097	0.000645048	0.7169811	0.6744186	0.8449078
Serpina3g	1.046903	1.106815	0.01705791	0.6415094	0.3488372	0.4399035
Sepp1	0.7991337	1.092565	0.04074512	0.5786164	0.4418605	0.5003937
Fscn1	0.7618184	1.088417	0.02757917	0.5786164	0.372093	0.3883811
Tpm2	0.5949423	1.083853	0.04774839	0.4465409	0.2790698	0.2788681
Bgn	1.676536	1.064994	0.000806805	0.7232704	0.6744186	1.046251
Dcn	3.065334	1.034623	7.8469E-05	0.9685535	0.9534884	2.175958
S100a6	1.451588	1.009571	0.001701332	0.7798742	0.7209302	1.080797
Cxcl13	4.955516	-1.00755	1.60466E-06	0.9748428	1	5.639964
Rassf2	0.3719221	-1.071137	0.04788748	0.3333333	0.6976744	0.7843431
Trf	1.511323	-1.081351	0.000518583	0.672956	0.8604651	2.288026
Nceh1	0.3459453	-1.085837	0.04686387	0.3333333	0.5581395	0.6112083
Fabp5	0.9066762	-1.092136	0.000332853	0.572327	0.7209302	1.500307
Cr2	1.806294	-1.103121	5.4313E-07	0.8050314	0.9069767	2.695282
Ephx2	0.5052991	-1.105021	0.01712381	0.3962264	0.7906977	1.109503
Lrrc58	0.3321424	-1.134034	0.02468203	0.3333333	0.6976744	0.7241073

Pebp1	0.3768399	-1.203821	0.0114067	0.3584906	0.6744186	0.8197654
Cilp	1.129343	-1.239961	8.16561E-06	0.6918239	0.9302326	1.991601
Mt1	0.6782329	-1.240202	0.000148171	0.490566	0.8372093	1.451294
Igfals	0.339787	-1.321779	0.006877946	0.3144654	0.6046512	0.8220004
Aif1	0.5530387	-1.330434	8.1486E-05	0.4025157	0.7674419	1.284455
Ager	0.7217922	-1.330944	7.31364E-05	0.5471698	0.7906977	1.327676
Nostrin	0.3027367	-1.40162	0.005678507	0.2201258	0.4883721	0.7072818
Madcam1	1.031099	-1.407797	3.28004E-06	0.5849057	0.6744186	1.604561
Stra6	0.4826252	-1.419547	0.000518583	0.3459119	0.6976744	1.122852
A230065H16Rik	0.6113779	-1.597831	2.21478E-05	0.3962264	0.7674419	1.464176
Serpina1e	0.7277172	-1.643327	2.18741E-06	0.408805	0.627907	1.388879

CHAPTER 4

Conclusion

Through this work we have investigated the diversity of LN stromal cells at niche-level resolution. We have described CRCs as a new player in the GC DZ distinct from LZ FDCs in morphology, phenotype and maintenance requirements. We identified transcriptional profiles for well-described stromal subsets and new niche-associated subsets of steady-state LN stroma. These profiles suggest mechanisms for known stromal functions and propose new roles for stromal cells in their respective niches.

In situ, we found CRCs did not express FDC markers and were morphologically distinct from FDCs. Our scRNA sequencing analysis of LN stroma from LCMV infected mice, however, did not reveal a distinct CRC subset. While validating expression of the transcription factor Sox9, we did find it expressed by both FDCs and CRCs suggesting these cells might be clustered together. This would indicate that CRCs are more transcriptionally similar to FDCs than their distinct morphology and chemokine expression would suggest. Alternatively, CRCs may not have been captured sufficiently in our dataset and the variability we see in the FDC cluster is due to shallow transcript capture. Future efforts that enrich for GC stromal cells, possibly using a Sox9 directed reporter, are necessary to resolve a transcriptional profile of CRCs.

The role of the DZ and CRCs in the regulation of effective affinity maturation is still unclear. The GC must support the development of broadly reactive and high affinity antibodies without allowing autoantibody development for an effective humoral response (Bannard and Cyster, 2017). A large body of recent work has suggested a model where when GC B present antigen-derived peptides to T follicular helper cells they may receive a signal, with strength correlated to their antibody affinity, to recycle to the DZ. This signal triggers a FOXO1, AP4 and c-myc regulated, timed DZ program

where the signal strength affects the number of divisions and dwell time of the GC B cell in the DZ. There they undergo SHM and upregulate their new, mutated BCR (Bannard et al., 2013; 2016; Chou et al., 2016; Dominguez-Sola et al., 2015; 2012; Gitlin et al., 2015; 2014; Sander et al., 2015). Analysis of CXCR4-deficient GC B cells that could not access the DZ revealed these cells could still proliferate, mutate and differentiate into memory and plasma cells, but failed to compete with DZ-experienced GC B cells over time along with producing antibodies with fewer mutations (Bannard et al., 2013). Selected GC B cells may need to access the DZ to escape the stringent competition in the LZ while the selected GC B cells increase the proportional contribution of their relatively high affinity BCR to the clonal pool through proliferation and mutation (Bannard and Cyster, 2017). CRCs may play a more active supporting role, contributing trophic signals and other inputs to DZ GC B cells that influence clonal bursting or protect lower affinity clones to improve the breadth of the response (Kuraoka et al., 2016; Tas et al., 2016).

Stromal-lymphocyte crosstalk is a common principle in the formation of lymphoid niches, but how each of the newly described stromal subsets develop is not fully understood. Follicle formation depends on FDCs secreting CXCL13 to attract B cells, which make the LT required for FDC maintenance (Ansel et al., 2000). CRCs are also present in primary follicles, always on the T-zone proximal side, but what signals induce their development distinct from their neighboring FDCs and Ccl19^{lo} TRCs is still unclear. Lymphatic endothelial cells help initiate LN development through a feed-forward crosstalk with lymphoid tissue inducers cells (Onder et al., 2017), but how the developing lymphoid stroma differentiate and reproducibly organize the LN niches is

unknown. We have validated several new markers for the stromal subsets we identified in the adult LN that could be useful in tracking LN stroma subset development embryonically as well as after pathogen disruption in the adult.

The mechanisms of stromal development in LNs may translate to the development of tertiary lymphoid tissues and suggest methods of intervention (Barone et al., 2016). Similarly, we found a specific subset of TRCs that have the potential to induce T-cell tolerance and may share a mechanism of action with tumor-promoting stromal cells that suppress infiltrating T cells (Turley et al., 2015). Chronic inflammation in many contexts can activate stromal cells to cause pathogenic fibrosis, but whether there is a particular subset of susceptible stroma is unclear because most peripheral tissue stroma is described only by expression of PDPN or PDGFR (Gieseck et al., 2017). We expect further use of scRNA sequencing to investigate LN endothelial stromal subsets, mucosal tissue stroma and peripheral tissue stroma will reveal unappreciated stromal diversity and functions.

REFERENCES

References

Acton, S.E., Farrugia, A.J., Astarita, J.L., Mourão-Sá, D., Jenkins, R.P., Nye, E., Hooper, S., van Blijswijk, J., Rogers, N.C., Snelgrove, K.J., et al. (2014). Dendritic cells control fibroblastic reticular network tension and lymph node expansion. Nature *514*, 498–502.

Aguzzi, A., and Krautler, N.J. (2010). Characterizing follicular dendritic cells: A progress report. Eur. J. Immunol. *40*, 2134–2138.

Akiyama, H., Chaboissier, M.-C., Behringer, R.R., Rowitch, D.H., Schedl, A., Epstein, J.A., and de Crombrugghe, B. (2004). Essential role of Sox9 in the pathway that controls formation of cardiac valves and septa. Proc. Natl. Acad. Sci. U.S.a. *101*, 6502–6507.

Allen, C.D.C., and Cyster, J.G. (2008). Follicular dendritic cell networks of primary follicles and germinal centers: phenotype and function. Seminars in Immunology *20*, 14–25.

Allen, C.D.C., Ansel, K.M., Low, C., Lesley, R., Tamamura, H., Fujii, N., and Cyster, J.G. (2004). Germinal center dark and light zone organization is mediated by CXCR4 and CXCR5. Nat Immunol *5*, 943–952.

Allen, C.D.C., Okada, T., and Cyster, J.G. (2007a). Germinal-center organization and cellular dynamics. Immunity *27*, 190–202.

Allen, C.D.C., Okada, T., Tang, H.L., and Cyster, J.G. (2007b). Imaging of germinal center selection events during affinity maturation. Science *315*, 528–531.

Andrian, von, U.H., and Mempel, T.R. (2003). Homing and cellular traffic in lymph nodes. Nat Rev Immunol *3*, 867–878.

Ansel, K.M., McHeyzer-Williams, L.J., Ngo, V.N., McHeyzer-Williams, M.G., and Cyster, J.G. (1999). In vivo-activated CD4 T cells upregulate CXC chemokine receptor 5 and reprogram their response to lymphoid chemokines. J. Exp. Med. *190*, 1123–1134.

Ansel, K.M., Ngo, V.N., Hyman, P.L., Luther, S.A., Förster, R., Sedgwick, J.D., Browning, J.L., Lipp, M., and Cyster, J.G. (2000). A chemokine-driven positive feedback loop organizes lymphoid follicles

. Nature *406*, 309–314.

Ara, T., Itoi, M., Kawabata, K., Egawa, T., Tokoyoda, K., Sugiyama, T., Fujii, N., Amagai, T., and Nagasawa, T. (2003a). A role of CXC chemokine ligand 12/stromal cell-derived factor-1/pre-B cell growth stimulating factor and its receptor CXCR4 in fetal and adult T cell development in vivo. J. Immunol. *170*, 4649–4655.

Ara, T., Tokoyoda, K., Sugiyama, T., Egawa, T., Kawabata, K., and Nagasawa, T.

(2003b). Long-term hematopoietic stem cells require stromal cell-derived factor-1 for colonizing bone marrow during ontogeny. Immunity *19*, 257–267.

Armulik, A., Genové, G., and Betsholtz, C. (2011). Pericytes: developmental, physiological, and pathological perspectives, problems, and promises. Developmental Cell *21*, 193–215.

Astarita, J.L., Cremasco, V., Fu, J., Darnell, M.C., Peck, J.R., Nieves-Bonilla, J.M., Song, K., Kondo, Y., Woodruff, M.C., Gogineni, A., et al. (2015). The CLEC-2-podoplanin axis controls the contractility of fibroblastic reticular cells and lymph node microarchitecture. Nat Immunol *16*, 75–84.

Bajénoff, M., Egen, J.G., Koo, L.Y., Laugier, J.P., Brau, F., Glaichenhaus, N., and Germain, R.N. (2006). Stromal Cell Networks Regulate Lymphocyte Entry, Migration, and Territoriality in Lymph Nodes. Immunity *25*, 989–1001.

Bannard, O., and Cyster, J.G. (2017). Germinal centers: programmed for affinity maturation and antibody diversification. Current Opinion in Immunology *45*, 21–30.

Bannard, O., Horton, R.M., Allen, C.D.C., An, J., Nagasawa, T., and Cyster, J.G. (2013). Germinal center centroblasts transition to a centrocyte phenotype according to a timed program and depend on the dark zone for effective selection. Immunity *39*, 912–924.

Bannard, O., McGowan, S.J., Ersching, J., Ishido, S., Victora, G.D., Shin, J.-S., and Cyster, J.G. (2016). Ubiquitin-mediated fluctuations in MHC class II facilitate efficient germinal center B cell responses. Journal of Experimental Medicine *213*, 993–1009.

Baptista, A.P., Roozendaal, R., Reijmers, R.M., Koning, J.J., Unger, W.W., Greuter, M., Keuning, E.D., Molenaar, R., Goverse, G., Sneeboer, M.M.S., et al. (2014). Lymph node stromal cells constrain immunity via MHC class II self-antigen presentation. Elife *3*, e24226.

Baratin, M., Simon, L., Jorquera, A., Ghigo, C., Dembele, D., Nowak, J., Gentek, R., Wienert, S., Klauschen, F., Malissen, B., et al. (2017). T Cell Zone Resident Macrophages Silently Dispose of Apoptotic Cells in the Lymph Node. Immunity *47*, 349–362.e5.

Barone, F., Gardner, D.H., Nayar, S., Steinthal, N., Buckley, C.D., and Luther, S.A. (2016). Stromal Fibroblasts in Tertiary Lymphoid Structures: A Novel Target in Chronic Inflammation. Front. Immun. *7*, 477.

Barral, P., Polzella, P., Bruckbauer, A., van Rooijen, N., Besra, G.S., Cerundolo, V., and Batista, F.D. (2010). CD169(+) macrophages present lipid antigens to mediate early activation of iNKT cells in lymph nodes. Nat Immunol *11*, 303–312.

Bauman, D.R., Bitmansour, A.D., McDonald, J.G., Thompson, B.M., Liang, G., and Russell, D.W. (2009). 25-Hydroxycholesterol secreted by macrophages in response to

Toll-like receptor activation suppresses immunoglobulin A production. Proc. Natl. Acad. Sci. U.S.a. *106*, 16764–16769.

Baumhueter, S., Singer, M.S., Henzel, W., Hemmerich, S., Renz, M., Rosen, S.D., and Lasky, L.A. (1993). Binding of L-selectin to the vascular sialomucin CD34. Science *262*, 436–438.

Beltman, J.B., Allen, C.D.C., Cyster, J.G., and de Boer, R.J. (2011). B cells within germinal centers migrate preferentially from dark to light zone. Proc. Natl. Acad. Sci. U.S.a. *108*, 8755–8760.

Bennett, M.L., Bennett, F.C., Liddelow, S.A., Ajami, B., Zamanian, J.L., Fernhoff, N.B., Mulinyawe, S.B., Bohlen, C.J., Adil, A., Tucker, A., et al. (2016). New tools for studying microglia in the mouse and human CNS. Proc. Natl. Acad. Sci. U.S.a. *113*, E1738–E1746.

Brown, F.D., and Turley, S.J. (2015). Fibroblastic reticular cells: organization and regulation of the T lymphocyte life cycle. The Journal of Immunology *194*, 1389–1394.

Butler, A., and Satija, R. (2017). Integrated analysis of single cell transcriptomic data across conditions, technologies, and species. bioRxiv 164889.

Chai, Q., Onder, L., Scandella, E., Gil-Cruz, C., Perez-Shibayama, C., Cupovic, J., Danuser, R., Sparwasser, T., Luther, S.A., Thiel, V., et al. (2013). Maturation of lymph node fibroblastic reticular cells from myofibroblastic precursors is critical for antiviral immunity. Immunity *38*, 1013–1024.

Chang, J.E., and Turley, S.J. (2015). Stromal infrastructure of the lymph node and coordination of immunity. Trends in Immunology *36*, 30–39.

Chappaz, S., Gärtner, C., Rodewald, H.-R., and Finke, D. (2010). Kit ligand and Il7 differentially regulate Peyer's patch and lymph node development. The Journal of Immunology *185*, 3514–3519.

Chou, C., Verbaro, D.J., Tonc, E., Holmgren, M., Cella, M., Colonna, M., Bhattacharya, D., and Egawa, T. (2016). The Transcription Factor AP4 Mediates Resolution of Chronic Viral Infection through Amplification of Germinal Center B Cell Responses. Immunity *45*, 570–582.

Chu, C.C., and Paul, W.E. (1997). Fig1, an interleukin 4-induced mouse B cell gene isolated by cDNA representational difference analysis. Proc. Natl. Acad. Sci. U.S.a. *94*, 2507–2512.

Clingan, J.M., and Matloubian, M. (2013). B Cell-intrinsic TLR7 signaling is required for optimal B cell responses during chronic viral infection. The Journal of Immunology *191*, 810–818.

Coombes, J.L., Han, S.-J., van Rooijen, N., Raulet, D.H., and Robey, E.A. (2012).

Infection-induced regulation of natural killer cells by macrophages and collagen at the lymph node subcapsular sinus. Cell Reports *2*, 124–135.

Corish, P., and Tyler-Smith, C. (1999). Attenuation of green fluorescent protein half-life in mammalian cells. Protein Eng. *12*, 1035–1040.

Corselli, M., Chen, C.-W., Sun, B., Yap, S., Rubin, J.P., and Péault, B. (2012). The Tunica Adventitia of Human Arteries and Veins As a Source of Mesenchymal Stem Cells. Stem Cells and Development *21*, 1299–1308.

Cremasco, V., Woodruff, M.C., Onder, L., Cupovic, J., Nieves-Bonilla, J.M., Schildberg, F.A., Chang, J., Cremasco, F., Harvey, C.J., Wucherpfennig, K., et al. (2014). B cell homeostasis and follicle confines are governed by fibroblastic reticular cells. Nat Immunol *15*, 973–981.

Cyster, J.G., Ansel, K.M., Reif, K., Ekland, E.H., Hyman, P.L., Tang, H.L., Luther, S.A., and Ngo, V.N. (2000). Follicular stromal cells and lymphocyte homing to follicles. Immunological Reviews *176*, 181–193.

Cyster, J.G. (2005). Chemokines, sphingosine-1-phosphate, and cell migration in secondary lymphoid organs. Annu. Rev. Immunol. *23*, 127–159.

Cyster, J.G. (2010). B cell follicles and antigen encounters of the third kind. Nat Immunol *11*, 989–996.

Cyster, J.G., Dang, E.V., Reboldi, A., and Yi, T. (2014). 25-Hydroxycholesterols in innate and adaptive immunity. Nat Rev Immunol *14*, 731–743.

Ding, L., and Morrison, S.J. (2013). Haematopoietic stem cells and early lymphoid progenitors occupy distinct bone marrow niches. Nature *495*, 231–235.

Díaz-Flores, L., Gutiérrez, R., García, M.P., Sáez, F.J., Valladares, F., and Madrid, J.F. (2014). CD34+ stromal cells/fibroblasts/fibrocytes/telocytes as a tissue reserve and a principal source of mesenchymal cells. Location, morphology, function and role in pathology. Histol. Histopathol. *29*, 831–870.

Dominguez-Sola, D., Kung, J., Holmes, A.B., Wells, V.A., Mo, T., Basso, K., and Dalla-Favera, R. (2015). The FOXO1 Transcription Factor Instructs the Germinal Center Dark Zone Program. Immunity *43*, 1064–1074.

Dominguez-Sola, D., Victora, G.D., Ying, C.Y., Phan, R.T., Saito, M., Nussenzweig, M.C., and Dalla-Favera, R. (2012). The proto-oncogene MYC is required for selection in the germinal center and cyclic reentry. Nat Immunol *13*, 1083–1091.

Dubrot, J., Duraes, F.V., Potin, L., Capotosti, F., Brighouse, D., Suter, T., LeibundGut-Landmann, S., Garbi, N., Reith, W., Swartz, M.A., et al. (2014). Lymph node stromal cells acquire peptide–MHCII complexes from dendritic cells and induce antigen-specific CD4+ T cell tolerance. Journal of Experimental Medicine *211*, 1153–1166.

Farr, A.G., Berry, M.L., Kim, A., Nelson, A.J., Welch, M.P., and Aruffo, A. (1992). Characterization and cloning of a novel glycoprotein expressed by stromal cells in T-dependent areas of peripheral lymphoid tissues. J. Exp. Med. *176*, 1477–1482.

Fasnacht, N., Huang, H.-Y., Koch, U., Favre, S., Auderset, F., Chai, Q., Onder, L., Kallert, S., Pinschewer, D.D., MacDonald, H.R., et al. (2014). Specific fibroblastic niches in secondary lymphoid organs orchestrate distinct Notch-regulated immune responses. Journal of Experimental Medicine *211*, 2265–2279.

Fichtner-Feigl, S., Strober, W., Kawakami, K., Puri, R.K., and Kitani, A. (2006). IL-13 signaling through the IL-13alpha2 receptor is involved in induction of TGF-beta1 production and fibrosis. Nat Med *12*, 99–106.

Fletcher, A.L., Acton, S.E., and Knoblich, K. (2015). Lymph node fibroblastic reticular cells in health and disease. Nat Rev Immunol *15*, 350–361.

Fletcher, A.L., Malhotra, D., and Turley, S.J. (2011). Lymph node stroma broaden the peripheral tolerance paradigm. Trends in Immunology *32*, 12–18.

Fooksman, D.R., Schwickert, T.A., Victora, G.D., Dustin, M.L., Nussenzweig, M.C., and Skokos, D. (2010). Development and migration of plasma cells in the mouse lymph node. Immunity *33*, 118–127.

Fu, Y.X., and Chaplin, D.D. (1999). Development and maturation of secondary lymphoid tissues. Annu. Rev. Immunol. *17*, 399–433.

Gieseck, R.L., Wilson, M.S., and Wynn, T.A. (2017). Type 2 immunity in tissue repair and fibrosis. Nat Rev Immunol.

Girard, J.-P., Moussion, C., and Förster, R. (2012). HEVs, lymphatics and homeostatic immune cell trafficking in lymph nodes. Nat Rev Immunol *12*, 762–773.

Gitlin, A.D., Mayer, C.T., Oliveira, T.Y., Shulman, Z., Jones, M.J.K., Koren, A., and Nussenzweig, M.C. (2015). T cell help controls the speed of the cell cycle in germinal center B cells. Science *349*, 643–646.

Gitlin, A.D., Shulman, Z., and Nussenzweig, M.C. (2014). Clonal selection in the germinal centre by regulated proliferation and hypermutation. Nature *509*, 637–640.

Goldstein, B.J., Goss, G.M., Hatzistergos, K.E., Rangel, E.B., Seidler, B., Saur, D., and Hare, J.M. (2014). Adult c-Kit(+) progenitor cells are necessary for maintenance and regeneration of olfactory neurons. J. Comp. Neurol. *523*, 15–31.

Gray, E.E., and Cyster, J.G. (2012a). Lymph node macrophages. J Innate Immun *4*, 424–436.

Gray, E.E., and Cyster, J.G. (2012b). Lymph Node Macrophages - FullText - Journal of Innate Immunity 2012, Vol. 4, No. 5-6 - Karger Publishers. J Innate Immun *4*, 424–436.

Gray, E.E., Friend, S., Suzuki, K., Phan, T.G., and Cyster, J.G. (2012). Subcapsular sinus macrophage fragmentation and CD169+ bleb acquisition by closely associated IL-17-committed innate-like lymphocytes. PLoS ONE *7*, e38258.

Gretz, J.E., Kaldjian, E.P., Anderson, A.O., and Shaw, S. (1996). Sophisticated strategies for information encounter in the lymph node: the reticular network as a conduit of soluble information and a highway for cell traffic. J. Immunol. *157*, 495–499.

Griffith, J.W., Sokol, C.L., and Luster, A.D. (2014). Chemokines and chemokine receptors: positioning cells for host defense and immunity. Annu. Rev. Immunol. *32*, 659–702.

Groom, J.R., Richmond, J., Murooka, T.T., Sorensen, E.W., Sung, J.H., Bankert, K., Andrian, von, U.H., Moon, J.J., Mempel, T.R., and Luster, A.D. (2012). CXCR3 chemokine receptor-ligand interactions in the lymph node optimize CD4+ T helper 1 cell differentiation. Immunity *37*, 1091–1103.

Guilliams, M., Dutertre, C.-A., Scott, C.L., McGovern, N., Sichien, D., Chakarov, S., Van Gassen, S., Chen, J., Poidinger, M., De Prijck, S., et al. (2016). Unsupervised High-Dimensional Analysis Aligns Dendritic Cells across Tissues and Species. Immunity *45*, 669–684.

Gunn, M.D., Tangemann, K., Tam, C., Cyster, J.G., Rosen, S.D., and Williams, L.T. (1998). A chemokine expressed in lymphoid high endothelial venules promotes the adhesion and chemotaxis of naive T lymphocytes. Proc. Natl. Acad. Sci. U.S.a. *95*, 258–263.

Hargreaves, D.C., Hyman, P.L., Lu, T.T., Ngo, V.N., Bidgol, A., Suzuki, G., Zou, Y.R., Littman, D.R., and Cyster, J.G. (2001). A coordinated change in chemokine responsiveness guides plasma cell movements. J. Exp. Med. *194*, 45–56.

He, C., Pillai, S.S., Taglini, F., Li, F., Ruan, K., Zhang, J., Wu, J., Shi, Y., and Bayne, E.H. (2013). Structural analysis of Stc1 provides insights into the coupling of RNAi and chromatin modification. Proc. Natl. Acad. Sci. U.S.a. *110*, E1879–E1888.

Heesters, B.A., Chatterjee, P., Kim, Y.-A., Gonzalez, S.F., Kuligowski, M.P., Kirchhausen, T., and Carroll, M.C. (2013). Endocytosis and Recycling of Immune Complexes by Follicular Dendritic Cells Enhances B Cell Antigen Binding and Activation. Immunity *38*, 1164–1175.

Heesters, B.A., Myers, R.C., and Carroll, M.C. (2014). Follicular dendritic cells: dynamic antigen libraries. Nat Rev Immunol *14*, 495–504.

Hindle, P., Khan, N., Biant, L., and Péault, B. (2017). The Infrapatellar Fat Pad as a Source of Perivascular Stem Cells with Increased Chondrogenic Potential for Regenerative Medicine. Stem Cells Transl Med *6*, 77–87.

Huang, Y.-H., Jankowski, A., Cheah, K.S.E., Prabhakar, S., and Jauch, R. (2015).

SOXE transcription factors form selective dimers on non-compact DNA motifs through multifaceted interactions between dimerization and high-mobility group domains. Sci Rep *5*, 378.

Iannacone, M., Moseman, E.A., Tonti, E., Bosurgi, L., Junt, T., Henrickson, S.E., Whelan, S.P., Guidotti, L.G., and Andrian, von, U.H. (2010a). Subcapsular sinus macrophages prevent CNS invasion on peripheral infection with a neurotropic virus. Nature *465*, 1079–1083.

Iannacone, M., Moseman, E.A., Tonti, E., Bosurgi, L., Junt, T., Henrickson, S.E., Whelan, S.P., Guidotti, L.G., and Andrian, von, U.H. (2010b). Subcapsular sinus macrophages prevent CNS invasion on peripheral infection with a neurotropic virus. Nature *465*, 1079–1083.

Imai, Y., and Yamakawa, M. (1996). Morphology, function and pathology of follicular dendritic cells. Pathology International *46*, 807–833.

Janatpour, M.J., Hudak, S., Sathe, M., Sedgwick, J.D., and McEvoy, L.M. (2001). Tumor Necrosis Factor–dependent Segmental Control of MIG Expression by High Endothelial Venules in Inflamed Lymph Nodes Regulates Monocyte Recruitment. Journal of Experimental Medicine *194*, 1375–1384.

Jarjour, M., Jorquera, A., Mondor, I., Wienert, S., Narang, P., Coles, M.C., Klauschen, F., and Bajénoff, M. (2014). Fate mapping reveals origin and dynamics of lymph node follicular dendritic cells. Journal of Experimental Medicine *211*, 1109–1122.

Johnson, L.A., and Jackson, D.G. (2013). The chemokine CX3CL1 promotes trafficking of dendritic cells through inflamed lymphatics. J Cell Sci *126*, 5259–5270.

Kanamoto, T., Mizuhashi, K., Terada, K., Minami, T., Yoshikawa, H., and Furukawa, T. (2009). Isolation and characterization of a novel plasma membrane protein, osteoblast induction factor (obif), associated with osteoblast differentiation. BMC Dev. Biol. *9*, 70.

Kanazawa, N., Nakamura, T., Tashiro, K., Muramatsu, M., Morita, K., Yoneda, K., Inaba, K., Imamura, S., and Honjo, T. (1999). Fractalkine and macrophage-derived chemokine: T cell-attracting chemokines expressed in T cell area dendritic cells. Eur. J. Immunol. *29*, 1925–1932.

Kanda, H., Newton, R., Klein, R., Morita, Y., Gunn, M.D., and Rosen, S.D. (2008). Autotaxin, an ectoenzyme that produces lysophosphatidic acid, promotes the entry of lymphocytes into secondary lymphoid organs. Nat Immunol *9*, 415–423.

Kasajima-Akatsuka, N., and Maeda, K. (2006). Development, maturation and subsequent activation of follicular dendritic cells (FDC): immunohistochemical observation of human fetal and adult lymph nodes. Histochem. Cell Biol. *126*, 261–273.

Kastenmuller, W., Brandes, M., Wang, Z., Herz, J., Egen, J.G., and Germain, R.N. (2013). Peripheral prepositioning and local CXCL9 chemokine-mediated guidance

orchestrate rapid memory CD8+ T cell responses in the lymph node. Immunity *38*, 502–513.

Kastenmuller, W., Torabi-Parizi, P., Subramanian, N., Lämmermann, T., and Germain, R.N. (2012). A spatially-organized multicellular innate immune response in lymph nodes limits systemic pathogen spread. Cell *150*, 1235–1248.

Katakai, T. (2012). Marginal reticular cells: a stromal subset directly descended from the lymphoid tissue organizer. Front. Immun. *3*, 200.

Katakai, T., and Kinashi, T. (2016). Microenvironmental Control of High-Speed Interstitial T Cell Migration in the Lymph Node. Front. Immun. *7*, 194.

Katakai, T., Hara, T., Lee, J.-H., Gonda, H., Sugai, M., and Shimizu, A. (2004). A novel reticular stromal structure in lymph node cortex: an immuno-platform for interactions among dendritic cells, T cells and B cells. Int. Immunol. *16*, 1133–1142.

Katakai, T., Kondo, N., Ueda, Y., and Kinashi, T. (2014). Autotaxin Produced by Stromal Cells Promotes LFA-1–Independent and Rho-Dependent Interstitial T Cell Motility in the Lymph Node Paracortex. The Journal of Immunology *193*, 617–626.

Khan, K.A., Naylor, A.J., Khan, A., Noy, P.J., Mambretti, M., Lodhia, P., Athwal, J., Korzystka, A., Buckley, C.D., Willcox, B.E., et al. (2017). Multimerin-2 is a ligand for group 14 family C-type lectins CLEC14A, CD93 and CD248 spanning the endothelial pericyte interface. Oncogene *63*, 183.

Kir, S., White, J.P., Kleiner, S., Kazak, L., Cohen, P., Baracos, V.E., and Spiegelman, B.M. (2014). Tumour-derived PTH-related protein triggers adipose tissue browning and cancer cachexia. Nature *513*, 100–104.

Kitazawa, T., Sato, T., Nishiyama, K., Asai, R., Arima, Y., Uchijima, Y., Kurihara, Y., and Kurihara, H. (2011). Identification and developmental analysis of endothelin receptor type-A expressing cells in the mouse kidney. Gene Expr. Patterns *11*, 371–377.

Kraus, M., Alimzhanov, M.B., Rajewsky, N., and Rajewsky, K. (2004). Survival of resting mature B lymphocytes depends on BCR signaling via the Igalpha/beta heterodimer. Cell *117*, 787–800.

Krautler, N.J., Kana, V., Kranich, J., Tian, Y., Perera, D., Lemm, D., Schwarz, P., Armulik, A., Browning, J.L., Tallquist, M., et al. (2012). Follicular dendritic cells emerge from ubiquitous perivascular precursors. Cell *150*, 194–206.

Kurachi, M., Kurachi, J., Suenaga, F., Tsukui, T., Abe, J., Ueha, S., Tomura, M., Sugihara, K., Takamura, S., Kakimi, K., et al. (2011). Chemokine receptor CXCR3 facilitates CD8+ T cell differentiation into short-lived effector cells leading to memory degeneration. Journal of Experimental Medicine *208*, 1605–1620.

Kuraoka, M., Schmidt, A.G., Nojima, T., Feng, F., Watanabe, A., Kitamura, D., Harrison,

S.C., Kepler, T.B., and Kelsoe, G. (2016). Complex Antigens Drive Permissive Clonal Selection in Germinal Centers. Immunity *44*, 542–552.

Lain, E., Carnejac, S., Escher, P., Wilson, M.C., Lømo, T., Gajendran, N., and Brenner, H.R. (2009). A Novel Role for Embigin to Promote Sprouting of Motor Nerve Terminals at the Neuromuscular Junction. Journal of Biological Chemistry *284*, 8930–8939.

Lasoudris, F., Cousin, C., Prevost-Blondel, A., Martin-Garcia, N., Abd-Alsamad, I., Ortonne, N., Farcet, J.-P., Castellano, F., and Molinier-Frenkel, V. (2011). IL4I1: an inhibitor of the CD8+ antitumor T-cell response in vivo. Eur. J. Immunol. *41*, 1629–1638.

Lax, S., Hardie, D.L., Wilson, A., Douglas, M.R., Anderson, G., Huso, D., Isacke, C.M., and Buckley, C.D. (2010). The pericyte and stromal cell marker CD248 (endosialin) is required for efficient lymph node expansion. Eur. J. Immunol. *40*, 1884–1889.

Lee, M., Kiefel, H., LaJevic, M.D., Macauley, M.S., O'Hara, E., Pan, J., Paulson, J.C., and Butcher, E.C. (2014). Transcriptional programs of lymphoid tissue capillary and high endothelium reveal control mechanisms for lymphocyte homing. Nat Immunol *15*, 982–995.

Lefevre, E.A., Hein, W.R., Stamataki, Z., Brackenbury, L.S., Supple, E.A., Hunt, L.G., Monaghan, P., Borhis, G., Richard, Y., and Charleston, B. (2007). Fibrinogen is localized on dark zone follicular dendritic cells in vivo and enhances the proliferation and survival of a centroblastic cell line in vitro. Journal of Leukocyte Biology *82*, 666–677.

Lelouard, H., Fallet, M., de Bovis, B., Méresse, S., and Gorvel, J.-P. (2012). Peyer's patch dendritic cells sample antigens by extending dendrites through M cell-specific transcellular pores. Gastroenterology *142*, 592–601.

Li, J., Lu, E., Yi, T., and Cyster, J.G. (2016). EBI2 augments Tfh cell fate by promoting interaction with IL-2-quenching dendritic cells. Nature *533*, 110–114.

Link, A., Vogt, T.K., Favre, S., Britschgi, M.R., Acha-Orbea, H., Hinz, B., Cyster, J.G., and Luther, S.A. (2007). Fibroblastic reticular cells in lymph nodes regulate the homeostasis of naive T cells. Nat Immunol *8*, 1255–1265.

Love, M.I., Huber, W., and Anders, S. (2014). Moderated estimation of fold change and dispersion for RNA-seq data with DESeq2. Genome Biology 2014 15:12 *15*, 550.

Lu, E., Dang, E.V., McDonald, J.G., and Cyster, J.G. (2017). Distinct oxysterol requirements for positioning naïve and activated dendritic cells in the spleen. Sci Immunol *2*, eaal5237.

Lu, T.T., and Browning, J.L. (2014). Role of the Lymphotoxin/LIGHT System in the Development and Maintenance of Reticular Networks and Vasculature in Lymphoid Tissues. Front. Immun. *5*, 47.

Lun, A.T.L., Bach, K., and Marioni, J.C. (2016). Pooling across cells to normalize single-cell RNA sequencing data with many zero counts. Genome Biology 2014 15:12 *17*, 75.

Luther, S.A., Tang, H.L., Hyman, P.L., Farr, A.G., and Cyster, J.G. (2000). Coexpression of the chemokines ELC and SLC by T zone stromal cells and deletion of the ELC gene in the plt/plt mouse. Proc. Natl. Acad. Sci. U.S.a. *97*, 12694–12699.

Maeda, K., Matsuda, M., Suzuki, H., and Saitoh, H.-A. (2002). Immunohistochemical recognition of human follicular dendritic cells (FDCs) in routinely processed paraffin sections. J. Histochem. Cytochem. *50*, 1475–1486.

Malhotra, D., Fletcher, A.L., and Turley, S.J. (2013). Stromal and hematopoietic cells in secondary lymphoid organs: partners in immunity. Immunological Reviews *251*, 160–176.

Malhotra, D., Fletcher, A.L., Astarita, J., Lukacs-Kornek, V., Tayalia, P., Gonzalez, S.F., Elpek, K.G., Chang, S.K., Knoblich, K., Hemler, M.E., et al. (2012). Transcriptional profiling of stroma from inflamed and resting lymph nodes defines immunological hallmarks. Nat Immunol *13*, 499–510.

Mavlyutov, T.A., Epstein, M.L., Liu, P., Verbny, Y.I., Ziskind-Conhaim, L., and Ruoho, A.E. (2012). Development of the sigma-1 receptor in C-terminals of motoneurons and colocalization with the N,N'-dimethyltryptamine forming enzyme, indole-N-methyl transferase. Neuroscience *206*, 60–68.

McCauley, L.K., and Martin, T.J. (2012). Twenty-five years of PTHrP progress: From cancer hormone to multifunctional cytokine. Journal of Bone and Mineral Research *27*, 1231–1239.

McCulloch, L., Brown, K.L., Bradford, B.M., Hopkins, J., Bailey, M., Rajewsky, K., Manson, J.C., and Mabbott, N.A. (2011). Follicular Dendritic Cell-Specific Prion Protein (PrPc) Expression Alone Is Sufficient to Sustain Prion Infection in the Spleen. PLoS Pathog *7*, e1002402.

McLatchie, L.M., Fraser, N.J., Main, M.J., Wise, A., Brown, J., Thompson, N., Solari, R., Lee, M.G., and Foord, S.M. (1998). RAMPs regulate the transport and ligand specificity of the calcitonin-receptor-like receptor. Nature *393*, 333–339.

Mionnet, C., Mondor, I., Jorquera, A., Loosveld, M., Maurizio, J., Arcangeli, M.-L., Ruddle, N.H., Nowak, J., Aurrand-Lions, M., Luche, H., et al. (2013). Identification of a new stromal cell type involved in the regulation of inflamed B cell follicles. PLoS Biol *11*, e1001672.

Mizoguchi, F., Slowikowski, K., Marshall, J.L., and Wei, K. (2017). Single Cell Transcriptomics And Flow Cytometry Reveal Disease-Associated Fibroblast Subsets In Rheumatoid Arthritis. bioRxiv.

Mizuhashi, K., Chaya, T., Kanamoto, T., Omori, Y., and Furukawa, T. (2015). Obif, a

Transmembrane Protein, Is Required for Bone Mineralization and Spermatogenesis in Mice. PLoS ONE *10*, e0133704.

Mueller, S.N., and Germain, R.N. (2009). Stromal cell contributions to the homeostasis and functionality of the immune system. Nat Rev Immunol *9*, 618–629.

Mueller, S.N., Hosiawa-Meagher, K.A., Konieczny, B.T., Sullivan, B.M., Bachmann, M.F., Locksley, R.M., Ahmed, R., and Matloubian, M. (2007). Regulation of homeostatic chemokine expression and cell trafficking during immune responses. Science *317*, 670–674.

Mundy, G.R., and Edwards, J.R. (2008). PTH-Related Peptide (PTHrP) in Hypercalcemia. Journal of the American Society of Nephrology *19*, 672–675.

Nakai, A., Hayano, Y., Furuta, F., Noda, M., and Suzuki, K. (2014). Control of lymphocyte egress from lymph nodes through β2-adrenergic receptors. Journal of Experimental Medicine *211*, 2583–2598.

Ngo, V.N., Korner, H., Gunn, M.D., Schmidt, K.N., Riminton, D.S., Cooper, M.D., Browning, J.L., Sedgwick, J.D., and Cyster, J.G. (1999). Lymphotoxin alpha/beta and tumor necrosis factor are required for stromal cell expression of homing chemokines in B and T cell areas of the spleen. J. Exp. Med. *189*, 403–412.

O'Sullivan, M.L., de Wit, J., Savas, J.N., Comoletti, D., Otto-Hitt, S., Yates, J.R., and Ghosh, A. (2012). FLRT proteins are endogenous latrophilin ligands and regulate excitatory synapse development. Neuron *73*, 903–910.

Okada, T., Ngo, V.N., Ekland, E.H., Förster, R., Lipp, M., Littman, D.R., and Cyster, J.G. (2002). Chemokine requirements for B cell entry to lymph nodes and Peyer's patches. J. Exp. Med. *196*, 65–75.

Onder, L., Mörbe, U., Pikor, N., Novkovic, M., Cheng, H.-W., Hehlgans, T., Pfeffer, K., Becher, B., Waisman, A., Rülicke, T., et al. (2017). Lymphatic Endothelial Cells Control Initiation of Lymph Node Organogenesis. Immunity *47*, 80–92.e84.

Onder, L., Scandella, E., Chai, Q., Firner, S., Mayer, C.T., Sparwasser, T., Thiel, V., Rülicke, T., and Ludewig, B. (2011). A novel bacterial artificial chromosome-transgenic podoplanin-cre mouse targets lymphoid organ stromal cells in vivo. Front. Immun. *2*, 50.

Pauly, S., Broll, K., Wittmann, M., Giegerich, G., and Schwarz, H. (2002). CD137 is expressed by follicular dendritic cells and costimulates B lymphocyte activation in germinal centers. Journal of Leukocyte Biology *72*, 35–42.

Phan, T.G., Grigorova, I., Okada, T., and Cyster, J.G. (2007). Subcapsular encounter and complement-dependent transport of immune complexes by lymph node B cells. Nat Immunol *8*, 992–1000.

Poyner, D.R. (1992). Calcitonin gene-related peptide: multiple actions, multiple

receptors. Pharmacol. Ther. *56*, 23–51.

Prinz, M., Montrasio, F., Klein, M.A., Schwarz, P., Priller, J., Odermatt, B., Pfeffer, K., and Aguzzi, A. (2002). Lymph nodal prion replication and neuroinvasion in mice devoid of follicular dendritic cells. Proc. Natl. Acad. Sci. U.S.a. *99*, 919–924.

Puiffe, M.-L., Lachaise, I., Molinier-Frenkel, V., and Castellano, F. (2013). Antibacterial properties of the mammalian L-amino acid oxidase IL4I1. PLoS ONE *8*, e54589.

Py, B.F., Gonzalez, S.F., Long, K., Kim, M.-S., Kim, Y.-A., Zhu, H., Yao, J., Degauque, N., Villet, R., Ymele-Leki, P., et al. (2013). Cochlin produced by follicular dendritic cells promotes antibacterial innate immunity. Immunity *38*, 1063–1072.

Rademakers, L.H. (1992). Dark and light zones of germinal centres of the human tonsil: an ultrastructural study with emphasis on heterogeneity of follicular dendritic cells. Cell Tissue Res. *269*, 359–368.

Roberts, E.W., Deonarine, A., Jones, J.O., Denton, A.E., Feig, C., Lyons, S.K., Espeli, M., Kraman, M., McKenna, B., Wells, R.J.B., et al. (2013). Depletion of stromal cells expressing fibroblast activation protein-α from skeletal muscle and bone marrow results in cachexia and anemia. Journal of Experimental Medicine *210*, 1137–1151.

Rodda, L.B., Bannard, O., Ludewig, B., Nagasawa, T., and Cyster, J.G. (2015). Phenotypic and Morphological Properties of Germinal Center Dark Zone Cxcl12-Expressing Reticular Cells. The Journal of Immunology *195*, 4781–4791.

Rohlich, K. (1930). Beitrag zur Cytologie der Keimzentren der Lymphknoten. Z. Mikrosk. Anat. Forsch. *20*, 287–297.

Roozendaal, R., and Mebius, R.E. (2011). Stromal Cell–Immune Cell Interactions. Annu. Rev. Immunol. *29*, 23–43.

Sander, S., Chu, V.T., Yasuda, T., Franklin, A., Graf, R., Calado, D.P., Li, S., Imami, K., Selbach, M., Di Virgilio, M., et al. (2015). PI3 Kinase and FOXO1 Transcription Factor Activity Differentially Control B Cells in the Germinal Center Light and Dark Zones. Immunity *43*, 1075–1086.

Satija, R., Farrell, J.A., Gennert, D., Schier, A.F., and Regev, A. (2015). Spatial reconstruction of single-cell gene expression data. Nat. Biotechnol. *33*, 495–502.

Scandella, E., Bolinger, B., Lattmann, E., Miller, S., Favre, S., Littman, D.R., Finke, D., Luther, S.A., Junt, T., and Ludewig, B. (2008). Restoration of lymphoid organ integrity through the interaction of lymphoid tissue-inducer cells with stroma of the T cell zone. Nat Immunol *9*, 667–675.

Schaefer, B.C., Schaefer, M.L., Kappler, J.W., Marrack, P., and Kedl, R.M. (2001). Observation of Antigen-Dependent CD8+ T-Cell/ Dendritic Cell Interactions in Vivo. Cellular Immunology 110–122.

Schmidt, T.H., Bannard, O., Gray, E.E., and Cyster, J.G. (2013). CXCR4 promotes B cell egress from Peyer's patches. Journal of Experimental Medicine *210*, 1099–1107.

Schulz, O., Hammerschmidt, S.I., Moschovakis, G.L., and Förster, R. (2016). Chemokines and Chemokine Receptors in Lymphoid Tissue Dynamics. Annu. Rev. Immunol. *34*, 203–242.

Shikh, El, M.E.M., and Pitzalis, C. (2012). Follicular dendritic cells in health and disease. Front. Immun. *3*, 292.

Sierro, F., Biben, C., Martínez-Muñoz, L., Mellado, M., Ransohoff, R.M., Li, M., Woehl, B., Leung, H., Groom, J., Batten, M., et al. (2007). Disrupted cardiac development but normal hematopoiesis in mice deficient in the second CXCL12/SDF-1 receptor, CXCR7. Proc. Natl. Acad. Sci. U.S.a. *104*, 14759–14764.

Sitnik, K.M., Wendland, K., Weishaupt, H., Uronen-Hansson, H., White, A.J., Anderson, G., Kotarsky, K., and Agace, W.W. (2016). Context-Dependent Development of Lymphoid Stroma from Adult CD34(+) Adventitial Progenitors. Cell Reports *14*, 2375–2388.

Sixt, M., Kanazawa, N., Selg, M., Samson, T., Roos, G., Reinhardt, D.P., Pabst, R., Lutz, M.B., and Sorokin, L. (2005). The conduit system transports soluble antigens from the afferent lymph to resident dendritic cells in the T cell area of the lymph node. Immunity *22*, 19–29.

Srinivas, S., Watanabe, T., Lin, C.S., William, C.M., Tanabe, Y., Jessell, T.M., and Costantini, F. (2001). Cre reporter strains produced by targeted insertion of EYFP and ECFP into the ROSA26 locus. BMC Dev. Biol. *1*, 4.

Stephenson, W., Donlin, L.T., Butler, A., Rozo, C., Rashidfarrokhi, A., Goodman, S.M., Ivashkiv, L.B., Bykerk, V.P., Orange, D.E., Darnell, R.B., et al. (2017). Single-Cell RNA-Seq Of Rheumatoid Arthritis Synovial Tissue Using Low Cost Microfluidic Instrumentation. bioRxiv 140848.

Strnad, P., Schwarz, P., Rasenack, M.C.D., Kucukoglu, O., Habib, R.I., Heuberger, D., Ehehalt, R., Müller, M.W., Stiehl, A., Adler, G., et al. (2011). Hepcidin Is an Antibacterial, Stress-Inducible Peptide of the Biliary System. PLoS ONE *6*, e16454.

Sung, J.H., Zhang, H., Moseman, E.A., Alvarez, D., Iannacone, M., Henrickson, S.E., la Torre, de, J.C., Groom, J.R., Luster, A.D., and Andrian, von, U.H. (2012). Chemokine guidance of central memory T cells is critical for antiviral recall responses in lymph nodes. Cell *150*, 1249–1263.

Suzuki, K., Grigorova, I., Phan, T.G., Kelly, L.M., and Cyster, J.G. (2009). Visualizing B cell capture of cognate antigen from follicular dendritic cells. Journal of Experimental Medicine *206*, 1485–1493.

Suzuki, K., Maruya, M., Kawamoto, S., Sitnik, K., Kitamura, H., Agace, W.W., and

Fagarasan, S. (2010). The sensing of environmental stimuli by follicular dendritic cells promotes immunoglobulin A generation in the gut. Immunity *33*, 71–83.

Tamamura, H., Hiramatsu, K., Mizumoto, M., Ueda, S., Kusano, S., Terakubo, S., Akamatsu, M., Yamamoto, N., Trent, J.O., Wang, Z., et al. (2003). Enhancement of the T140-based pharmacophores leads to the development of more potent and bio-stable CXCR4 antagonists. Org. Biomol. Chem. *1*, 3663–3669.

Tas, J.M.J., Mesin, L., Pasqual, G., Targ, S., Jacobsen, J.T., Mano, Y.M., Chen, C.S., Weill, J.-C., Reynaud, C.-A., Browne, E.P., et al. (2016). Visualizing antibody affinity maturation in germinal centers. Science *351*, 1048–1054.

Tirosh, I., Izar, B., Prakadan, S.M., Wadsworth, M.H., Treacy, D., Trombetta, J.J., Rotem, A., Rodman, C., Lian, C., Murphy, G., et al. (2016). Dissecting the multicellular ecosystem of metastatic melanoma by single-cell RNA-seq. Science *352*, 189–196.

Tokuda, N., Adachi, T., Adachi, Y., Higashi, M., Sharifi, K., Tuerxun, T., Sawada, T., Kondo, H., and Owada, Y. (2010). Identification of FABP7 in fibroblastic reticular cells of mouse lymph nodes. Histochem. Cell Biol. *134*, 445–452.

Tsunoda, T., Yamakawa, M., and Takahashi, T. (1999). Differential expression of Ca(2+)-binding proteins on follicular dendritic cells in non-neoplastic and neoplastic lymphoid follicles. The American Journal of Pathology *155*, 805–814.

Turley, S.J., Cremasco, V., and Astarita, J.L. (2015). Immunological hallmarks of stromal cells in the tumour microenvironment. Nat Rev Immunol *15*, 669–682.

Uhlén, M., Fagerberg, L., Hallström, B.M., Lindskog, C., Oksvold, P., Mardinoglu, A., Sivertsson, A., Kampf, C., Sjöstedt, E., Asplund, A., et al. (2015). Proteomics. Tissue-based map of the human proteome. Science *347*, 1260419.

Ullman, K.S., Northrop, J.P., Verweij, C.L., and Crabtree, G.R. (1990). Transmission of signals from the T lymphocyte antigen receptor to the genes responsible for cell proliferation and immune function: the missing link. Annu. Rev. Immunol. *8*, 421–452.

Ulvmar, M.H., Werth, K., Braun, A., Kelay, P., Hub, E., Eller, K., Chan, L., Lucas, B., Novitzky-Basso, I., Nakamura, K., et al. (2014). The atypical chemokine receptor CCRL1 shapes functional CCL21 gradients in lymph nodes. Nat Immunol *15*, 623–630.

Umemoto, E., Otani, K., Ikeno, T., Verjan Garcia, N., Hayasaka, H., Bai, Z., Jang, M.H., Tanaka, T., Nagasawa, T., Ueda, K., et al. (2012). Constitutive plasmacytoid dendritic cell migration to the splenic white pulp is cooperatively regulated by CCR7- and CXCR4-mediated signaling. The Journal of Immunology *189*, 191–199.

van de Pavert, S.A., and Mebius, R.E. (2010). New insights into the development of lymphoid tissues. Nat Rev Immunol *10*, 664–674.

Victora, G.D., and Nussenzweig, M.C. (2012). Germinal centers. Annu. Rev. Immunol.

30, 429–457.

Victora, G.D., Schwickert, T.A., Fooksman, D.R., Kamphorst, A.O., Meyer-Hermann, M., Dustin, M.L., and Nussenzweig, M.C. (2010). Germinal center dynamics revealed by multiphoton microscopy with a photoactivatable fluorescent reporter. Cell *143*, 592–605.

Vilardaga, J.-P., Romero, G., Friedman, P.A., and Gardella, T.J. (2010). Molecular basis of parathyroid hormone receptor signaling and trafficking: a family B GPCR paradigm. Cell. Mol. Life Sci. *68*, 1–13.

Wang, F., Flanagan, J., Su, N., Wang, L.-C., Bui, S., Nielson, A., Wu, X., Vo, H.-T., Ma, X.-J., and Luo, Y. (2012). RNAscope. The Journal of Molecular Diagnostics *14*, 22–29.

Wang, X., Cho, B., Suzuki, K., Xu, Y., Green, J.A., An, J., and Cyster, J.G. (2011). Follicular dendritic cells help establish follicle identity and promote B cell retention in germinal centers. Journal of Experimental Medicine *208*, 2497–2510.

Wang, X., Rodda, L.B., Bannard, O., and Cyster, J.G. (2014). Integrin-mediated interactions between B cells and follicular dendritic cells influence germinal center B cell fitness. The Journal of Immunology *192*, 4601–4609.

Wilke, G., Steinhauser, G., Grün, J., and Berek, C. (2010). In silico subtraction approach reveals a close lineage relationship between follicular dendritic cells and BP3hi stromal cells isolated from SCID mice. Eur. J. Immunol. *40*, 2165–2173.

Yi, T., Wang, X., Kelly, L.M., An, J., Xu, Y., Sailer, A.W., Gustafsson, J.-A., Russell, D.W., and Cyster, J.G. (2012). Oxysterol Gradient Generation by Lymphoid Stromal Cells Guides Activated B Cell Movement during Humoral Responses. Immunity *37*, 535–548.

Yoneyama, H., Matsuno, K., Zhang, Y., Nishiwaki, T., Kitabatake, M., Ueha, S., Narumi, S., Morikawa, S., Ezaki, T., Lu, B., et al. (2004). Evidence for recruitment of plasmacytoid dendritic cell precursors to inflamed lymph nodes through high endothelial venules. Int. Immunol. *16*, 915–928.

Zhang, J.G., Hilton, D.J., Willson, T.A., McFarlane, C., Roberts, B.A., Moritz, R.L., Simpson, R.J., Alexander, W.S., Metcalf, D., and Nicola, N.A. (1997). Identification, purification, and characterization of a soluble interleukin (IL)-13-binding protein. Evidence that it is distinct from the cloned Il-13 receptor and Il-4 receptor alpha-chains. J. Biol. Chem. *272*, 9474–9480.

Zhang, Y., Roth, T.L., Gray, E.E., Chen, H., Rodda, L.B., Liang, Y., Ventura, P., Villeda, S., Crocker, P.R., and Cyster, J.G. (2016). Migratory and adhesive cues controlling innate-like lymphocyte surveillance of the pathogen-exposed surface of the lymph node. Elife *5*.

Zheng, G.X.Y., Terry, J.M., Belgrader, P., Ryvkin, P., Bent, Z.W., Wilson, R., Ziraldo, S.B., Wheeler, T.D., McDermott, G.P., Zhu, J., et al. (2017). Massively parallel digital

transcriptional profiling of single cells. Nat Commun *8*, 14049.

Zikherman, J., Parameswaran, R., and Weiss, A. (2012). Endogenous antigen tunes the responsiveness of naive B cells but not T cells. Nature *489*, 160–164.

Publishing Agreement

It is the policy of the University to encourage the distribution of all theses, dissertations, and manuscripts. Copies of all UCSF theses, dissertations, and manuscripts will be routed to the library via the Graduate Division. The library will make all theses, dissertations, and manuscripts accessible to the public and will preserve these to the best of their abilities, in perpetuity.

Please sign the following statement:

I hereby grant permission to the Graduate Division of the University of California, San Francisco to release copies of my thesis, dissertation, or manuscript to the Campus Library to provide access and preservation, in whole or in part, in perpetuity.

Author Signature

12/15/2017

Date